University College London

# A Computational Analysis of Thorium Dioxide and $Th_{(1-x)}U_xO_2$ Systems

Thesis submitted for the degree of Doctor of Philosophy (PhD) by

**Ashley Elizabeth Shields**

Supervisor:

Professor Nora H. de Leeuw

University College London

Department of Chemistry

December 2015

## Declaration

I, Ashley Elizabeth Shields, confirm that the work presented in this thesis is my own. Where information has been derived from other sources, I confirm that this has been properly indicated and fully acknowledged in the thesis.

Ashley Elizabeth Shields

December 2015

## Abstract

Nuclear power generation is an important way to satisfy rising global energy needs without increasing dependence on coal and petroleum. However, conventional nuclear fuels, such as uranium and plutonium dioxides, raise several safety concerns. Many countries have shown a renewed interest in thorium-based fuels as a potentially safer alternative. Thorium dioxide requires small amounts of a neutron source, such as uranium or plutonium, to generate a sustainable fission reaction. Due to the hazards of conducting experimental work on radioactive substances, a robust theoretical understanding of this doped-$ThO_2$ fuel is needed.

Using Density Functional Theory (DFT), we have studied the effects of uranium addition on the electronic structures of both the pure thoria bulk structure and three flat surfaces of $ThO_2$ and simulated Scanning Tunneling Microscopy (STM) images of each surface. We have also studied the effect of a uranium adatom on these surfaces. However, we wished to study larger systems than are practical to simulate with DFT, and so we developed a new Th-O Buckingham-type force field that has been optimized to work with a leading $UO_2$ interatomic potential. With this new potential, we have completed a configurational analysis of uranium substitution in thoria supercells of varying sizes and investigated the effects of uranium-doping on the thermophysical properties of the system. We have also modeled $ThO_2$ and U-doped thoria stepped surfaces and grain

boundaries, including the segregation energies of a uranium impurity and an oxygen defect in these systems.

# Acknowledgments

I would like to first and foremost thank my supervisor, Professor Nora de Leeuw for providing me with the opportunity to join her research group and for her support, guidance, and encouragement throughout the years of this project. I also wish to gratefully acknowledge the support provided to me and for this research by the Molecular Modeling and Materials Science Centre for Doctoral Training at UCL.

I'd also like to thank the members of the de Leeuw group, most particularly Dr Zhimei Du, for all of the practical advice, numerous useful discussions, encouragement, and friendship over the years. I especially want to thank Dr David Santos Carballal and James Pegg for reading this thesis. To Jane, Fruzsi, Milena, Kay, and Ben—thank you for being quick with a mid-afternoon cup of coffee or a drink after work when the situation called for one.

I am grateful to my family and friends near and far who have provided endless support throughout the years. Thank you for staying on top of every change of address and remembering all of my various phone numbers.

I dedicate this thesis to the memory of my grandmother Martha Banks, who sadly passed away during its writing but was very proud of its pending completion.

# List of Publications

The work discussed in this thesis has been published in the following papers:

*Theoretical analysis of uranium-doped thorium dioxide: introduction of a thoria force field with explicit polarization*: A. E. Shields, S. E. Ruiz-Hernandez, N. H. de Leeuw, AIP Advances **5** (2015) 087118.

*A density functional theory study of uranium-doped thoria and uranium adatoms on the major surfaces of thorium dioxide*: A. E. Shields, N. H. de Leeuw, submitted.

*Simulations of interfaces in thorium dioxide and the effects of uranium-doping on the segregation of defects at surfaces and grain boundaries*: A. E. Shields, N. H. de Leeuw, in preparation.

A. E. Shields, S. E. Ruiz-Hernandez, N. H. de Leeuw, *IOP Conf. Ser.:Mater. Sci. Eng*. **80** (2015) 012007.

A. E. Shields, S. E. Ruiz-Hernandez, N. H. de Leeuw, Thorium Energy Conference 2013, in press.

# Table of Contents

# Table of Figures

# Table of Tables

# Chapter 1

# Introduction

## 1.1 Nuclear Fuels

According to the International Atomic Energy Agency's (IAEA) Power Reactor Information System (PRIS), there are currently 441 operating nuclear power reactors, two in long-term shutdown, and sixty-five under construction (Anon 2015). Energy demands around the world are increasing, especially in rapidly developing nations, e.g. India and China. As supplies of conventional fossil fuels such as petroleum and coal become more difficult to access, clean and renewable energy sources are needed. Additional concerns over anthropogenic global warming (i.e. climate change) cast doubt on the sustainability of a carbon-based fuel economy. Even without considering climate effects or future global energy demands, there is a present concern that as older nuclear reactors come offline, a gap in current energy production is created that needs to be filled in order to meet power demands.

While nuclear power is based on compounds that must be mined and these elements do not represent a renewable resource, a survey of 103 studies calculating the greenhouse gas emissions of nuclear power plants showed these emissions are minimal compared to that of fossil fuels (Sovacool 2008). Indeed the entirety of the carbon footprint of nuclear electricity generation comes from the burning of traditional fuels in the course of mining, transport, and refining the fuel elements and waste products.

Although the majority of nuclear power reactors operating today use uranium and/or plutonium-based fuels such as low-enriched uranium (LEU) or mixed oxide fuels (MOX), alternative nuclear fuels are being considered as well (Crawford et al. 2007). The most promising alternatives are thorium-based fuels. Thorium is generally estimated to be between three and four times more abundant than uranium in the Earth's crust, with large stores in India, the United States, and other areas around the world, making elemental thorium an accessible starting material for nuclear fuels. Thorium compounds can be used to fuel nuclear reactors and they present an attractive alternative to the standard uranium and plutonium MOX fuels. The utilization of thorium in electricity generation will extend the useful life of clean nuclear power by taking full advantage of available fertile materials, while allowing more time for the investigation and optimization of truly renewable energy resources.

There are many different types of nuclear reactor in which thorium fuels could be used. In Generation IV reactors, a variety of fuel types are used. Some of these

fuels are based on fluoride fuels, using uranium or thorium fluorides. Others, such as Pebble Bed reactors, are designed to run with a nuclear oxide fuel.

While $ThO_2$ is used industrially for its ceramic properties, its applications as a potentially safe, abundant nuclear fuel make it the subject of computational research. Computational studies are an ideal way to both refine existing knowledge of thorium and investigate thorium-based fuels due to the difficulties associated with conducting experiments with hazardous materials such as thorium and uranium.

## 1.2 Physical and Mechanical Properties of Thorium Dioxide

Pure thorium dioxide (thoria) is a ceramic material with a melting point of 3651 K, the highest of any known oxide (Ronchi & Hiernaut 1996). $ThO_2$ also represents the highest oxidation state of the material, which makes it exceptionally stable in the presence of oxygen or water. This corrosion resistance has positive implications for the use of thoria in nuclear fuels. Thoria, like the dioxides of uranium, plutonium, and cerium, has the fluorite structure, space group $Fm\bar{3}m$ (225) (Figure 1-1). The lattice parameter of cubic thorium dioxide is 5.6001 Å (Idiri et al. 2004). With an experimental band gap of 5.75 eV (Land & Rodine 1971), thoria is classified as an insulator.

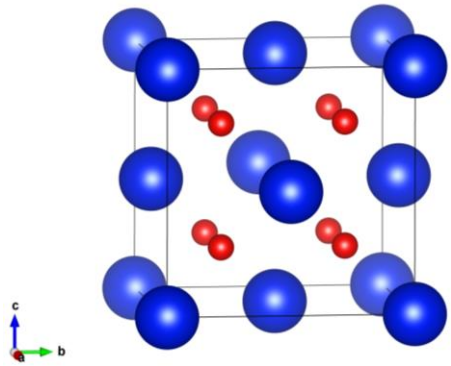


**Figure 1-1 The cubic fluorite *Fm$\bar{3}$m* structure of thorium dioxide, where Th atoms are represented in blue and oxygen in red.**

## 1.3 Uses and Applications of Thorium Dioxide

### 1.3.1 Industrial Uses

Although many early uses of thorium-containing industrial and commercial products has now stopped due to the radiation hazards involved, thorium dioxide has several industrial uses. Due to its high melting point, it is used in high temperature applications. While increasingly being replaced by non-radioactive compounds, thoria can serve to catalyze a range of chemical reactions, including Fischer-Tropsch reactions (Schulz 1999). $ThO_2$ is used as an additive in tungsten alloys to make electrodes for tungsten inert gas welding, although care must be taken to protect workers from exposure during use (Jankovic et al. 1999).

At present, elemental thorium is primarily of interest for its role in nuclear fuels. Thorium fuels can take several forms. Thorium fluoride is a fuel option for Molten

Salt Reactors (MSR), specifically in Liquid Fluoride Thorium Reactors (LFTRs). However, as many currently operating nuclear reactors use enriched $UO_2$ or MOX fuels, thorium dioxide is of immediate interest. Thorium can be combined with uranium or plutonium to create a new MOX fuel very similar to the uranium or plutonium fuels used now.

There are several advantages to using a MOX fuel that is primarily thorium-based. Since thorium is fertile but not fissile, a neutron is required for a fission reaction to occur. On the addition of a neutron, the stable $^{232}$Th isotope is converted into unstable $^{233}$Th, which is then transmuted via beta minus decay into Proactinium-233. $^{233}$Pa itself undergoes beta minus decay and is finally transmuted into the fissile $^{233}$U isotope per the following scheme (Dekoussar et al. 2005).

$$^{232}_{90}Th + neutron \rightarrow {}^{233}_{90}Th \xrightarrow{\beta- decay} {}^{233}_{91}Pa \xrightarrow{\beta- decay} {}^{233}_{92}U \rightarrow sustainable\ fission$$

**Figure 1-2 Transmutation scheme of Thorium-232**

The neutron source for the initial neutron can be uranium or plutonium, including U or Pu recycled from nuclear waste (Schram & Klaassen 2007; Lindley & Parks 2012). Only a small amount is strictly required although uranium or plutonium can be used in greater quantities depending on the desired fuel blend.

These thorium-containing fuels can be used in a variety of nuclear reactors. The so-called Generation II reactors, which comprise the bulk of operating reactor

types today, including pressurized water reactors (PWRs) and light water reactors (LWRs) typically use a uranium-based MOX fuel. These reactors can be adapted to use with thoria fuels due to the similarities between $UO_2$ and $ThO_2$. Generation IV nuclear reactors are being developed now and thorium fuels may also be deployed in these reactors (Lombardi et al. 2008).

### 1.3.2 Potential Benefits of Thorium Fuels

The many potential benefits of thorium fuels range from non-proliferation of nuclear weapons to increased safety. In a preliminary study published in 2011, calculations were performed on a fuel comprised of $^{235}U$ and $^{232}Th$ to be used in gas-cooled heavy water reactors (Ioffe & Kochurov 2012). This blend met the IAEA standards for non-proliferation and, via the production of $^{233}U$, created a highly radioactive product believed to be too difficult to move off-site for use in the production of nuclear weapons. Indeed, it is the production of the fissile and difficult to handle $^{233}U$ isotope that makes thorium reactor fuels an unlikely candidate for nuclear weapons. By comparison, plutonium is easier to handle in weapons manufacturing. Therefore any nuclear reactor that generates plutonium as a byproduct of nuclear decay must be closely observed by the international community (Greaves et al. 2012).

In a study of thorium fuel use in light water reactors by Herring et al a fuel blend of $ThO_2$ (70% by weight) and $UO_2$ (30% by weight) was shown to yield less plutonium overall than pure $UO_2$ fuel (Herring et al. 2001). Furthermore, at no

point in the studied fuel cycle was there an opportunity to isolate uranium as required for the production of nuclear weapons. Herring also concluded that $ThO_2$-$UO_2$ mix has several other important differences when compared to $UO_2$. These include changes in the decay heat, melting point, and thermal conductivity of the material, in addition to a decrease in the release rate of fission gases despite an actual increase in the production of fission gases. Further studies are needed to elucidate the effects of these changes on reactor performance and compliance with safety requirements.

Radioactive waste presents a challenge to countries that use nuclear power. However, reactors that use thorium can incorporate plutonium waste into the fuel blend, thereby burning up more plutonium than would be possible in a MOX reactor, for example (Schram & Klaassen 2007). Work by Lindley and Parks has demonstrated that transuranic waste (TRU) can be almost entirely used up when combined with thorium to form a MOX fuel in a pressurized water reactor (PWR) (Lindley & Parks 2012). This approach, pending full scale testing, would allow for a reduction in global nuclear waste stockpiles without requiring any new reactor technology.

## 1.4 Defects in Thorium Dioxide

Computational studies have been carried out to determine defect energies and migration in the thorium dioxide structure. While defects are of interest in any material, it is particularly important to understand the formation and migration of

vacancies and interstitials in a nuclear fuel such as $ThO_2$ due to the safety concerns presented should the fuel structure be compromised. To this end, several experimental and computational studies investigating the defect structure have been conducted and the basic Frenkel and Schottky defects are well understood.

Understanding defect migration and the migration of particles such as Xe that are released during radioactive decay of thoria is important. Several studies have been undertaken to determine the effects of fission products in thoria. Experimental studies conducted by Shiba et al in the early 1980s, irradiated samples of thoria-urania solid solutions heated to 1000 °C, then allowed those to cool for several days before the trapped gases were released and $^{133}Xe$ was measured (Shiba et al. 1981; Shiba et al. 1984). Shiba et al determined Xe was most likely released via vacancy clusters at this temperature. Yun et al investigated defect energy as well as Xe diffusion in $ThO_2$ using Density Functional Theory (DFT) with the Generalized Gradient Approximation (GGA) calculations in the Vienna *Ab Initio* Simulation Package (VASP) (Yun et al. 2009). Yun et al determined there is an energy barrier of 6.21 eV for Xe to migrate between adjacent octahedral sites, which indicates that vacancy migration is a more probable means of Xe diffusion in the thoria matrix. Since the point defects were calculated to have higher migration energies in thoria than in urania, this indicates that thoria fuels should have decreased release of fission produce gases.

Expanding on the work of Yun, Xiao et al investigated the incorporation and trapping of Br, Rb, Cs, and Xe fission products in thoria with DFT using Local Density Approximation (LDA) calculations implemented in VASP (Xiao et al. 2011). Xiao found that these fission products are not likely to be found in oxygen vacancy or octahedral sites, confirming the earlier Xe results of Yun. The thorium vacancy, $V_{Th}$, gives the most stable trapping for all products, with Rb the most stable, followed by Cs, Br, and finally Xe. This trend continues in all of the vacancy sites investigated, including oxygen vacancies, $V_O$, thorium-oxygen di-vacancies, $V_{ThO}$, and three types of tri-vacancies formed by O-Th-O vacancies. Table 1-1 summarizes the results of trapping these fission products in $ThO_2$, as calculated by Xiao et al, where the three tri-vacancies are denoted by the O-Th-O angle, $V_{79.5}$, $V_{109.5}$, and $V_{180}$.

**Table 1-1 Incorporation energy (eV) of trapping selected fission products in seven separate vacancy sites calculated by Xiao et al (Xiao et al. 2011).**

| Fission Product | Energy (eV) of incorporating fission product into the trapping site | | | | | | |
|---|---|---|---|---|---|---|---|
| | $V_{Th}$ | $V_O$ | $V_{ThO}$ | $V_{79.5}$ | $V_{109.5}$ | $V_{180}$ | Octahedral |
| Rb | -5.93 | 7.89 | -5.77 | -2.64 | -2.10 | -2.26 | 5.72 |
| Cs | -5.65 | 9.11 | -5.19 | -1.88 | -1.44 | -1.59 | 8.14 |
| Br | -4.69 | -0.38 | -3.11 | -2.45 | -1.70 | -0.50 | 3.56 |
| Xe | -1.37 | 9.45 | -0.08 | -0.20 | 0.88 | 1.68 | 9.53 |

Given the interest in using thoria in a fuel blend with other actinide oxides, in 2011, Xiao et al investigated oxygen vacancies in a ceria-thoria solid solution, $Ce_xTh_{1-x}O_2$ (Xiao & Weber 2011). Using DFT with the LDA in VASP, Xiao et al calculated that in pure thoria, an oxygen vacancy did not significantly displace the Th nearest neighbors. However, doping the thoria system with Ce, resulted in larger distances between the vacancy site and the Th or Ce nearest neighbor. Oxygen vacancy migration was calculated along the <100> and <$\bar{1}$00> directions for the $Ce_xTh_{1-x}O_{2-y}$ solid solution. As the amount of ceria-doping increased, the migration energy of the oxygen vacancy decreased. The lowest migration energy calculated for the solid solution was at a value of x= 0.75. Understanding the way dopants affect the properties of the pure thoria system

are critical to evaluating the performance of both thorium fuels and thorium waste in the future.

## 1.5 Thesis Chapter Summary

The work presented in this thesis is focused on the study of uranium-doped thorium dioxide. Th-U MOX blends are of great practical interest for developers and operators of nuclear power generators around the world. In Chapter 2, the general methodology employed in our study is discussed with a focus on the theories and approximations that underpin the computational codes used in this thesis. In Chapter 3, we present a new force field interatomic potential with explicit polarization to describe the Th-O interaction. The distribution of uranium atoms in bulk $ThO_2$ for the $ThO_2$-$UO_2$ solid solution is explored in Chapter 4 along with several important thermodynamic properties of the solid solution. A study of the electronic structure of $ThO_2$ and U-doped $ThO_2$ and the effects of uranium adsorption on the dominant surfaces of $ThO_2$ using DFT is presented in Chapter 5. Chapter 6 uses the potential model developed in Chapter 3 to model pure thoria and uranium-doped thoria stepped surfaces and grain boundaries. Finally, in Chapter 7, we discuss the results and conclusions of this study of Th-U oxides and the possibilities for future theoretical and experimental work on these materials.

# Chapter 2

# Theoretical Methodology for Modeling Materials

## 2.1 Introduction to Theoretical and Computational Methods

In this chapter the numerous computational methodologies that have been employed during the formulation of this thesis are discussed. To examine the electronic structure of thorium dioxide ($ThO_2$), we have used methods based on density functional theory (DFT). For our study of larger $ThO_2$ systems, including grain boundaries, we have used interatomic potentials via force field methods. The chapter begins with a description of DFT followed by a discussion of force field methods and, finally, an overview of configurational statistical mechanics.

## 2.2 Density Functional Theory

### 2.2.1 Background and Introduction

Density functional theory (DFT) serves as a way to approximate solutions to the Schrödinger equation (Schrödinger 1926) and the Born-Oppenheimer approximation (Born & Oppenheimer 1927) of Schrödinger's equation to describe chemical systems. The origins of DFT are based on refinements to earlier theories, beginning with the equation proposed by Schrödinger. Fundamental particles, such as electrons, are known to have wave-particle duality, wherein they express the characteristics and behavior of both waves and particles. It is at this point that the laws of classical mechanics fail to completely describe the behavior of these systems and we must turn to quantum mechanics. The quantum state of any system may be described completely by its wave function.

The time-independent Schrödinger's equation relates the wave function, Ψ, Hamiltonian $\hat{H}$, and energy *E* of a system via:

$$E\Psi = \hat{H}\Psi \qquad \textbf{(2-1)}$$

The Hamiltonian operator acts on the system of wave function Ψ such that it is proportional to the term *E*. The Hamiltonian is a quantum mechanical operator that contains information about the total energy of the system in question, where the total energy is considered to be the sum of the kinetic and potential

energies. Consequently, the Hamiltonian operator can be broken out into terms relating to the kinetic and potential energy operators, $\hat{T}$ and $\hat{V}$, respectively. These can be further separated into terms relating to the system in question. For an atomic system, the Hamiltonian becomes:

$$\hat{\mathrm{H}} = \hat{T} + \hat{V} = \hat{T}_e + \hat{T}_n + \hat{V}_{ee} + \hat{V}_{nn} + \hat{V}_{en} \quad \textbf{(2-2)}$$

Where $\hat{T}_e$ and $\hat{T}_n$ are the kinetic energy operators of the electrons and nuclei, respectively and $\hat{V}_{ee}$, $\hat{V}_{nn}$, and $\hat{V}_{en}$ are the potential energy operators for the electrons, nucleus, and the electrons and nucleus together, respectively. It is only possible to solve the Schrödinger equation explicitly for one-electron systems due to the lack of a numerical method to solve the electron-electron interaction energy in multi-electron systems.

In order to simplify the solution to the Schrödinger equation for many-electron atomic and molecular systems, approximations must be made. The Born-Oppenheimer approximation treats the kinetic energy of electrons and nuclei in the many-body wave function separately. This is achieved by considering that since the mass of the nuclei is so much greater than that of the electrons, the nuclei can effectively be held static in a system of moving electrons, thus negating the contribution of the nuclei to the kinetic energy. Furthermore, nucleus-nucleus repulsion is assumed to be constant, providing an additional approximation and thus simplification of the electronic Schrödinger equation. It is still difficult to solve this equation and further approximations are useful.

To provide an approximate solution to the Schrödinger equation, the Hartree-Fock (HF) method considers only the average repulsion between one electron in the system and the other electrons. One of the main disadvantages of HF theory is that the electron correlation is not described and therefore the calculated energy of the system is missing the electron correlation energy. While HF calculates the electron exchange energy and neglects the contribution of electron correlation, density functional theory offers an approximate solution to both the exchange and correlation energies, which lead to improved descriptions of the total energy. This improvement comes at a reasonable computational cost; therefore, DFT is now widely employed in computational chemistry.

## 2.2.2 Underlying Theorems

### 2.2.2.1 Hohenberg-Kohn Theorem

The theorems that underpin DFT were first proposed by Hohenberg and Kohn in 1964 (Hohenberg & Kohn 1964), expanding on the work of Thomas and Fermi (Thomas 1927; Fermi 1927). The Thomas-Fermi model used the electron density of a many-body system in calculations of the total atomic energy. While Schrödinger's equation requires 3*N* special coordinates for a system with *N* electrons, Hohenberg and Kohn simplified this by describing an inhomogeneous gas using its electron density, $\rho(\mathbf{r})$, which can be described by only 3 spatial coordinates. They determined that if the ground state is not degenerate, then the ground state electron density of a many electron system is related by a unique

functional to the static external potential $v(\mathbf{r})$ in which the electrons move. This external potential is key to determining the Hamiltonian and thus the physical properties of the system. The energy of the ground state, $E[\rho(\mathbf{r})]$ can be expressed in terms of the electron density, the external potential, and the functional $F[\rho(\mathbf{r})]$ as follows:

$$E[\rho(\boldsymbol{r})] = \int v(\boldsymbol{r})\rho(\boldsymbol{r})d\boldsymbol{r} + F[\rho(\boldsymbol{r})] \quad \textbf{(2-3)}$$

Hohenberg and Kohn also proposed that by applying a variational principle to minimize the value of the energy $E[\rho(\mathbf{r})]$ relative to the electron density, the exact value of ρ(r) can be found. The functional $F[\rho(\mathbf{r})]$ can be separated into terms representing the energy of the Coulomb interaction and a new functional $G[\rho(\mathbf{r})]$:

$$F[\rho(\boldsymbol{r})] = \frac{1}{2}\int \frac{\rho(\boldsymbol{r})\rho(\boldsymbol{r}')}{|\boldsymbol{r}-\boldsymbol{r}'|} d\boldsymbol{r}d\boldsymbol{r}' + G[\rho(\boldsymbol{r})] \quad \textbf{(2-4)}$$

#### 2.2.2.2 Kohn-Sham Theorem

Further improvements on the work of Hohenberg and Kohn were published the following year by Kohn and Sham (Kohn & Sham 1965). They considered a fictitious system of non-interacting electrons to have the same electron density as a real system with interacting electrons. By revising the expression for the total energy of the ground state of a real system as determined by the

Hohenberg Kohn theorem (Equation (2-3), the functional $G[\rho(\boldsymbol{r})]$ in a system of interacting electrons may be approximated by the kinetic energy ($T$[ρ(**r**)]) of a non-interacting system and the exchange correlation energy $E_{xc}$[ρ(**r**)]:

$$G[\rho(\boldsymbol{r})] = T[\rho(\boldsymbol{r})] + E_{xc}[\rho(\boldsymbol{r})] \quad \textbf{(2-5)}$$

In this fictitious system, Kohn and Sham rewrote the Schrödinger equation in terms of one electron orbitals ($\psi_i$) with one orbital energy ($\varepsilon_i$). The term representing the Hamiltonian operator can now be separated into three terms:

$$\left\{-\frac{1}{2}\nabla^2 + \left[\varphi(\boldsymbol{r}) + \mu_{xc}\big(\rho(\boldsymbol{r})\big)\right]\right\}\psi_i = \varepsilon_i\psi_i \quad \textbf{(2-6)}$$

where the first term of the Hamiltonian is equivalent to the kinetic energy and $\nabla^2$ is the Laplace operator, $\phi_i$ is a potential equal to the sum of the static external potential ($v$(**r**) from the Hohenberg-Kohn theorem) and the Coulomb interaction of a given electron density with the other electrons in the system, and the final term of the Hamiltonian operator is the potential $\mu_{xc}$[ρ(r)] due to the exchange and correlation of electrons. The electron density of this system of $N$ electrons can then be expressed as the sum of the orbitals:

$$\rho(r) = \sum_{n=1}^{N} |\psi_i|^2 \quad \textbf{(2-7)}$$

While the Hohenberg-Kohn theorem reduced the number of variables to three spatial coordinates, the use of orbitals in the Kohn-Shan formalism again

requires 3*N* spatial coordinates. From Equation (2-6 there are still refinements needed to DFT to improve the calculation of the exchange-correlation interactions in a many-body system. We will discuss two of the most common approximations in the sections below.

### 2.2.3 Approximations and Corrections to DFT

#### 2.2.3.1 Local Density Approximation

The local density approximation (LDA) or, for spin-polarized systems, the local spin density approximation (LSDA) was first proposed as a way to improve the description of the total exchange-correlation energy $E_{xc}$. In the LDA or LSDA, this energy in a real system can be estimated locally at a point **r** using the exchange-correlation energy of each particle in a uniform electron gas (jellium), $\varepsilon_{xc}$

$$E_{xc}^{LDA}[\rho(\boldsymbol{r})] = \int \rho(\boldsymbol{r})\varepsilon_{xc}\rho(\boldsymbol{r})d\boldsymbol{r} \quad \textbf{(2-8)}$$

The exchange-correlation energy can be further split into separate components. Here the exchange correlation term is a combination of exchange energy, $E_x$, and correlation energy, $E_c$.

$$E_{xc} = E_x + E_c \quad \textbf{(2-9)}$$

Accurate quantum Monte Carlo calculations on the jellium system (Ceperley & Alder 1980) have provided good values of $E_x$ to use in LDA/LSDA calculations and led to the development and popularity of several LDA DFT functionals (Vosko et al. 1980; Perdew & Wang 1992). It is difficult to obtain a good value of $E_c$ via this method. Known issues with the local density approximation include a poor description of Van der Waals interactions, hydrogen bonding, and the self-interaction problem between electrons (discussed in section 2.2.3.4).

### 2.2.3.2 General Gradient Approximation

The generalized gradient approximation (GGA) provides an alternate approximation of the exchange-correlation energy. In the GGA, the exchange-correlation energy for a given system is estimated from the gradient of the electron density at a point r. The equation for $E_{xc}$ in terms of the local gradient of the electron density, $\nabla\rho$, now becomes:

$$E_{xc}^{GGA}[\rho(r)] = \int \rho(r)\, \varepsilon_{xc}(\rho, \nabla\rho) dr \qquad \textbf{(2-10)}$$

There are several popular GGA functionals, such as those by Perdew and Wang (PW91) and by Perdue-Burke-Enzerhof (PBE) (Perdew & Wang 1992; Perdew et al. 1992; J. P. Perdew et al. 1996) which build upon the LDA from first principles.

### 2.2.3.3 Hybrid Functionals

Hybrid functionals combine the exchange-correlation energy of DFT functionals with part of the exact, non-localized Hartree-Fock exchange energy. Examples of hybrid functionals include LYP (Lee et al. 1988), BLYP (Becke 1988; Lee et al. 1988), B3LYP (Becke 1988; Lee et al. 1988; Becke 1993), and PBE0 (Lee et al. 1988; Adamo & Barone 1999). While these functionals offer an improvement on pure DFT functionals to more accurately describe important properties such as bonding, the self-interaction problem is not solved and therefore the band gap of semiconductors and insulators is still significantly underestimated.

### 2.2.3.4 Hubbard U Correction

The self-interaction of electrons is a problem in DFT that occurs because the correlation energy is not exact. An electron is then considered to have a Coulombic interaction with itself. In Hartree-Fock theory, the self-interaction is canceled because the exchange energy is treated exactly and the correlation energy is excluded. For systems with highly correlated *d* or *f* valence electrons, common among the transition metals and the actinide series, the self-interaction error is particularly prevalent and requires correction via the use of a Hubbard (DFT+U) Hamiltonian term. Without this correction, termed the Hubbard *U* correction, DFT functionals fail to describe these strongly correlated valence electrons. The newly corrected methods are termed DFT + U, e.g. LDA + U and GGA + U (Anisimov et al. 1991).

The Hubbard Hamiltonian (Hubbard 1963) uses the *U* parameter to apply an energy penalty to the double occupation of *d*- and *f*- bands by enhancing the on-site Coulomb repulsion between valence electrons. The U parameter can also be applied to *s* and *p* valence electrons, although this is less common than its application to *d* and *f* bands. In comparison to uncorrected LDA or GGA calculations, the introduction of Hubbard U parameters can improve the description of the band gap in semiconductors and insulators. There are two approaches to DFT+U, the first proposed by Liechtenstein (Liechtenstein et al. 1995) and the second, more simplified version by Dudarev (Dudarev et al. 1998). With the simplifications of Dudarev et al it is only necessary to consider the effective *U* parameter, $U_{eff}$:

$$U_{eff} = U - J \tag{2-11}$$

where U and J are Coulombic and exchange parameters, respectively, in the expression of the total DFT+U energy:

$$E_{DFT+U} = E_{DFT} + \frac{U_{eff}}{2} \sum_{\sigma} \left[ \left( \sum_{j} \rho_{jj}^{\sigma} \right) - \left( \sum_{j,l} \rho_{jl}^{\sigma} \rho_{lj}^{\sigma} \right) \right] \tag{2-12}$$

where σ is the spin and $\rho^{\sigma}$ is the density matrix of the electrons. An appropriate $U_{eff}$ value for a given system and a given set of functionals is selected by testing values of $U_{eff}$ to see which best reproduces experimentally available properties

such as the band gap and the lattice parameters. In this work we have used the Hubbard U correction in conjunction with PBE functionals.

## 2.2.4 Basis Sets

### 2.2.4.1 Localized Basis Sets

The selection and use of basis sets is important in ab initio methods such as DFT. A complete basis set is one that includes all of the functions necessary to describe the unknown function of a molecular orbital. This would require an infinite number of functions, which is of course impossible to calculate. Therefore a finite basis set must be chosen that is computationally practical while still providing an accurate representation of the system. There are two basic types of basis functions, Slater Type Orbitals (STOs) (Slater 1930) and Gaussian Type Orbitals (GTOs) (Boys 1950) which can be combined linearly to approximate all of the molecular orbitals in the simulation. STOs are similar to actual atomic orbitals and correctly model the exponential decay of the molecular orbitals with distance. Conversely, GTOs fail over long interatomic distances but can be combined to provide a good description of the orbitals. GTOs are generally easier to calculate and are therefore more popular than STOs. In this thesis, we have used plane wave basis sets, as discussed in the next section, in all DFT calculations.

### 2.2.4.2 Plane Wave Basis Sets

In solids with periodic boundary conditions, the unit cell is repeated infinitely in all directions. In reciprocal space, points corresponding to the primitive unit cell comprise the first Brillouin zone, sometimes referred to in the literature simply as the Brillouin zone. Reciprocal lattice space is the lattice that results from a Fourier transform of the wavefunction of the original, real space, lattice. Every vector **k** within the first Brillouin zone is unique. Plane wave basis sets are derived from Bloch's theorem (Bloch 1929), which states that electrons in a perfect crystal can be described by a basis set of functions comprised of Bloch wavefunctions $\psi_k(\mathbf{r})$ of the form:

$$\psi_k(\mathbf{r}) = e^{i\mathbf{k}\cdot\mathbf{r}}u(\mathbf{r}) \quad \textbf{(2-13)}$$

where **k** is a wave vector in reciprocal space, **r** is the position in real space, *u* is a periodic function that replicates the periodicity of the system, and $e^{i\mathbf{k}\cdot\mathbf{r}}$ the form of a plane wave. The introduction of the function *u*(**r**) ensures the periodicity of the Bloch wavefunction matches the finite crystal by relating positions in the unit cell to their equivalent positions throughout the crystal through the expression:

$$u(\mathbf{r}) = u(\mathbf{r} + \mathbf{T}) \quad \textbf{(2-14)}$$

We can now expand the function *u*(**r**) as a Fourier series in terms of the reciprocal lattice vectors **G:**

$$u(\mathbf{r}) = \sum_{\mathbf{G}} C_{i,\mathbf{k}+\mathbf{G}} e^{i\mathbf{G}\cdot\mathbf{r}} \quad \textbf{(2-15)}$$

where C represents the coefficients of the wave and reciprocal lattice vectors.

By applying Bloch's theorem in a periodic crystal, we no longer need to consider an infinite number of one electron wavefunctions. We are only concerned with the wavefunctions of the points **k** in the first Brillouin zone. However, to fully solve the Kohn-Sham equations in a periodic system, we would have to solve $\psi_k(\mathbf{r})$ at every possible **k** in the first Brillouin zone. As this is, of course, impossible, we must select a finite number of **k** points to calculate the energy of the crystal. The selection of k-points in this thesis is based on the Monkhorst-Pack grid (Monkhorst & Pack 1976), where the k-points are spaced evenly throughout the first Brillouin zone. A larger grid samples more k-points, improving accuracy but increasing the computational cost.

We can also write the wavefunction $\psi_k(\mathbf{r})$ with the expanded form of *u*(**r**):

$$\psi_{i,\mathbf{k}}(\mathbf{r}) = \sum_{\mathbf{G}} C_{\boldsymbol{i},\mathbf{k}+\mathbf{G}}\, e^{i(\mathbf{k}+\mathbf{G})\cdot\mathbf{r}} \quad \textbf{(2-16)}$$

Plane wave basis sets are delocalized, unlike STO and GTO basis sets, which are localized, typically on the atomic nucleus. An infinite number of plane waves would be needed to exactly solve for the wavefunction; however, we can

approximate the solution by only including those plane waves with a kinetic energy value that is lower than a pre-determined value (2-17), $E_{cutoff}$.

$$E_{cutoff} = \left(\frac{h}{2m_e}\right)|\mathbf{k} + \mathbf{G}|^2 \quad \textbf{(2-17)}$$

This cutoff energy is different for every system and must be carefully selected. Normally a suitable cutoff energy is close to the kinetic energy of the fastest electron in the crystal. Even by reducing the number of plane waves required through setting a cutoff energy, the system still requires a prohibitively large number of plane waves to describe all of the electrons in the system. One solution to this problem is to only consider the valence electrons through the use of pseudopotentials.

## 2.2.5 Pseudopotentials

When using plane wave basis sets, a large number of functions are required to describe the electrons in the core. For *f* block elements, there are a particularly large number of core electrons; however, the chemistry and properties of the system are primarily determined by the valence electrons. If the core of the atom is considered to be frozen, then it can be described by a pseudo-wavefunction which approximates the interaction of the valence electrons with the core. In DFT calculations, a pseudopotential is then considered to act on the valence electrons. The inclusion of pseudopotentials simplifies the calculation in a number of ways. Core electrons have the highest kinetic energy and therefore

using plane waves to describe the core requires a very high cutoff energy. Computationally, the calculation time increases for high values of $E_{cutoff}$, so avoiding a plane wave basis set describing all the core electrons provides a significant computational advantage.

There are several general types of pseudopotentials, including norm-conserving pseudopotentials (Hamann et al. 1979), ultrasoft pseudopotentials (Vanderbilt 1990), which are a variation on this approach, and projector augmented wave (PAW) pseudopotentials (Blöchl 1994). The PAW approach of Blöchl draws from the all-electron linear augmented plane wave methodology. All of the core electrons are included in this method, although they are frozen in position while the valence electrons are allowed to relax. By retaining the core electrons in the calculation, the all-electron wavefunction is used and therefore those properties which depend on inclusion of the core electron states, such as charge and spin density, are able to be calculated. PAW pseudopotentials are also typically faster to calculate than norm-conserving or ultrasoft pseudopotentials. We have used the PAW pseudopotential method in our calculations, as implemented in the Vienna *Ab Initio* Simulation Package (VASP) (Kresse & Joubert 1999).

## 2.3 Force Field Methods

### 2.3.1 Background and Introduction

As mentioned in previous sections, the energy of a system can only be calculated exactly for one-electron systems. Consequently approximations must

be made to treat systems with multiple electrons and nuclei. Force field methods address this issue by dealing with the interaction between atoms in the system, as opposed to treating the sub-atomic particles explicitly. The energy of the system, *U*, is considered to be an expansion series of the interactions between the atoms in the system:

$$U = \sum_{i=1}^{N} U_i + \frac{1}{2}\sum_{i=1}^{N}\sum_{j=1}^{N} U_{ij} + \frac{1}{6}\sum_{i=1}^{N}\sum_{j=1}^{N}\sum_{k=1}^{N} U_{ijk} + \cdots \quad \textbf{(2-18)}$$

where *N* is the total number of atoms and *i, j,* and *k* are individual atoms in the system.

For practical purposes, we must truncate the summation at some point to exclude higher order terms. Since the interaction between atoms is inversely proportional to the distance between them, it is logical to exclude atoms which are located far from each other in the system, by means of a cutoff distance.

In the Born model of crystal solids (Born & Huang 1954), the atoms in the system are considered to be charged spherical ions whose interatomic interactions are governed by short-range and long-range forces. Short-range forces include both repulsive and van der Waals forces while long-range forces are dominated by Coulombic (electrostatic) interactions. The lattice energy of the crystals is defined as:

$$U(r_{ij}) = \Phi_{l-r}(r_{ij}) + \Phi_{s-r}(r_{ij}) \quad \textbf{(2-19)}$$

$$U_{Coulomb} = \frac{q_j q_j}{4\pi\varepsilon_0 r_{ij}} \quad \textbf{(2-20)}$$

where $\Phi_{l\text{-}r}$ and $\Phi_{s\text{-}r}$ are potentials which correspond to the long-range and short-range forces, respectively. The electrostatic interactions account for most of the lattice energy and the equation for these is given in Equation (2-20, where *q* is the charge on the atom, $r_{ij}$ is the interatomic distance between the atoms *i* and *j*, and $\varepsilon_0$ is the vacuum permittivity. These short-range forces converge quickly whereas the long-range forces do not. This is because long-range forces include a large number of weak interactions. For a given ion *i* in an infinite 3D periodic crystal, while the strength of the interaction between ion *i* and other ions in the system decreases as the distance *r* increases, the number of ions interacting with *i* increases as *r* increases. This presents a significant complication in the calculation of the lattice energy, which can be mitigated with the Ewald summation (Ewald 1921).

The Ewald summation is a method for calculating the Coulombic forces in three dimensional periodic systems. The forces are considered to be the sum of three potential energy terms as seen in Equation **(2-21)**one which is calculated in real space, $U_{real}$, one in reciprocal space, $U_{recip}$, and one self-energy term, $U_{self}$, which is constant.

$$U_{Coulomb(Ewald)} = U_{real} + U_{recip} + U_{self} \quad \textbf{(2-21)}$$

## 2.3.2 Interatomic Potentials

The energy of the short-term interactions in systems can be described using different types of interatomic potentials. Different forms of the potential energy expressions are suitable for different types of ionic or molecular systems. Interatomic potentials are categorized by the number of particles interacting, e.g. two-body, three-body, or multi-body potentials.

Two body potentials include only the forces arising from the interactions between two ions or molecules and can take many forms. Two-body potentials are sufficiently accurate for many systems since two-body interactions comprise most of the short-range energy. The Morse potential (Morse 1929) and the Lennard-Jones potential (Jones 1924) are simple interatomic potentials with few parameters that require fitting to experimental data. The Morse potential for a diatomic molecule has the form:

$$U_{Morse}(r_{ij}) = D_e\left(1 - e^{-a(r-r_e)}\right)^2 \quad \textbf{(2-22)}$$

where $D_e$ is the dissociation energy of the atoms *i* and *j*, *a* is a constant related to $D_e$ and the force constant $k_e$ by the expression $a = \sqrt{k_e/2D_e}$, *r* is the distance between the atoms and $r_e$ is the equilibrium bond distance of *i* and *j*. The

Lennard-Jones potential, $U_{L\text{-}J}$, is comprised of a repulsive term, $r^{-12}$, which arises due to Pauli repulsion and an attractive term, $r^{-6}$, which is due to dispersion forces. It is useful for gases with neutral atoms and so is particularly accurate for the noble gases. The Lennard-Jones potential has the form:

$$U_{L-J}(r_{ij}) = 4\varepsilon\left[\left(\frac{\sigma}{r_{ij}}\right)^{12} - \left(\frac{\sigma}{r_{ij}}\right)^{6}\right] \quad \textbf{(2-23)}$$

where ε is the depth of the potential well, i.e. the energy difference between a reference energy value and a minimum of the potential energy, and σ is the distance where the intermolecular potential between *i* and *j* is zero.

Commonly used two-body potentials in ionic solids include Buckingham-type (Buckingham 1938) and Born-Mayer potentials. Buckingham proposed Equation (2-24) to be an alternative form of the Lennard-Jones potential. The attractive ($r^{-6}$) term is very similar to that of Lennard-Jones while the repulsive term (the $r^{-12}$ term in the Lennard-Jones potential) now becomes an exponential term of the form $A_{ij}e^{\frac{-r_{ij}}{\rho_{ij}}}$.

$$U_{Buck}(r_{ij}) = A_{ij}e^{\frac{-r_{ij}}{\rho_{ij}}} - \frac{C_{ij}}{r_{ij}^{6}} \quad \textbf{(2-24)}$$

$$U_{Born-Mayer}(r_{ij}) = Ae^{-r_{ij}/\rho} \quad \textbf{(2-25)}$$

where A, ρ, and C are parameters that are derived from experimental data or *ab initio* calculations, if experimental data is not available for the system. There are variations on the form of the Buckingham potential, which are discussed in the next chapter. In general, Buckingham potentials will fail if the interatomic distances are very small, although this is not typically an issue in ionic solids, where they are most commonly employed. In a Born-Mayer potential, the value of parameter A is adjusted to account for the attractive interactions.

Many-body interatomic potentials increase the complexity of the calculations but are particularly suitable for molecular and covalently bonded systems as angular contributions are taken into consideration. For example, a general form of a three-body function where the angle $\theta_{ijk}$ between the interacting ions *i*, *j*, and *k* can be accounted for with a simple harmonic expression, based on the Sanders potential for $SiO_2$ (Sanders et al. 1984).

$$U_{3B} = \frac{1}{2}k\left(\theta_{ijk} - \theta_0\right)^2 \quad \textbf{(2-26)}$$

where *k* is the force constant of the bending between the ions and $\theta_{ijk}$ is the equilibrium value of the angle. Other forms of three-body potentials are available depending on the system in question. Four-body potentials are useful in

molecular mechanics to describe the torsion (dihedral) angle $\phi$ between ions *i*, *j*, *k*, and *l* as follows:

$$U_{ijkl} = k[1 + \cos(n\phi - \phi_0)] \quad \textbf{(2-27)}$$

where *k* is the force constant of the bending between the four ions, *n* is the periodicity, and $\phi_0$ is the equilibrium dihedral angle.

### 2.3.3 Electronic Polarizability via the Shell Model

The above methods neglect polarizability in the system by approximating the atoms and ions in the system as point charges. The shell model proposed by Dick and Overhauser (Dick & Overhauser 1958) treats any polarizable atoms and ions as having two parts: a core and a massless shell, connected by a harmonic spring. The core contains the nucleus and inner electrons. Since the shell only contains the valence electrons, it can safely be considered to have no mass for the purposes of the calculation. In the shell model, only the shell experiences short-range forces but the long-range electrostatic interactions are applied to both the core and the shell of the ion in question.

### 2.3.4 Energy Minimization

We have used interatomic potentials as implemented in the General Utility Lattice Program (GULP) (Gale 1997; Gale & Rohl 2003) and in the Minimum Energy Techniques Applied to Dislocation, Interface, and Surface Energies (METADISE) code (Watson et al. 1996). Both of these codes use energy

minimization techniques to find local or global minima on the potential energy surface. The net forces acting on the system are minimized, the atomic positions adjusted step-wise and the forces recalculated until an arrangement of atoms is found that minimizes the energy. Popular methods to minimize the energy include the conjugate gradients algorithm (Shanno 1970) or the Newton-Raphson method, the latter of which has been used in the work presented in Chapter 6.

## 2.4 Configurational Statistical Mechanics

In this work we have used statistical mechanics and symmetry properties to study different possible configurations of substituted atoms in supercells by using the Site Occupancy Disorder (SOD) code (Grau-Crespo et al. 2007). For a given substitution of one atom for one of another element, SOD calculates the full configurational space (n = 1, …, M), i.e. all possible ways of carrying out the atomic substitutions in the crystal lattice. Then through the application of symmetry operators, the configurational space is reduced to a number of inequivalent configurations. These independent configurations represent all of the symmetrically equivalent configurations found in the full configurational space.

If we consider the system and all possible configurations to be in thermodynamic equilibrium, then the probability ($P_n$) of finding any one configuration can be given by a Boltzmann-like distribution:

$$P_n = \frac{1}{Z} exp\left(\frac{-E_n}{k_B T}\right) \quad \textbf{(2-28)}$$

where Z is the partition function, $E_n$ is the energy of configuration n, $k_B$ is Boltzmann's constant, and T is the temperature of the system. The partition function is given by:

$$Z = \sum_{n=1}^{N} exp\left(\frac{-E_n}{k_B T}\right) \quad \textbf{(2-29)}$$

Then after the complete number of configurations is reduced to only the inequivalent configurations, we can consider, at thermodynamic equilibrium at temperature *T,* the probability $P_m$ of any inequivalent configuration *m* in this reduced space to be:

$$P_m = \frac{\Omega_m}{Z} exp\left(\frac{-E_m}{RT}\right) \quad \textbf{(2-30)}$$

where $\Omega_m$ is the degeneracy, or number of symmetrically equivalent occurrences, of configuration *m* and the partition function Z is now expressed by:

$$Z = \sum_{m=1}^{M} exp\left(\frac{-E_m}{RT}\right) \quad \textbf{( 2-31)}$$

where $m$ = 1, …,M, where M is the total number of inequivalent configurations

The next chapters include discussion of the derivation of a new interatomic potential for thorium dioxide, the results of simulations using this new potential and computational codes which use the methodology outlined above.

# Chapter 3

# Development of a Novel Interatomic Potential for Th-O Interactions

## 3.1 Introduction

With a limited amount of experimental data available for thorium dioxide ($ThO_2$) and the prohibitive cost of DFT studies on large systems, there is a need for a reliable set of $ThO_2$ interatomic potentials to model systems of this mineral. In this chapter we evaluate the published experimental and theoretical studies of the mechanical properties of $ThO_2$. The results of these studies have been fiercely debated and having reliable values for these properties is essential in the development and verification of interatomic potentials. There is also a selection of interatomic potentials already published that have been used in the

modeling of $ThO_2$. However, as we will discuss in the following sections, upon evaluation for suitability in our proposed study, we determined that we needed to develop a novel Buckingham-type potential using the shell model of ions that is compatible with a leading uranium oxide ($UO_2$) potential of the same form. In this way we can simulate more complex, real world cases of uranium doping and defects in $ThO_2$ containing many hundreds or thousands of atoms. Density Functional Theory (DFT) is a very useful theory and one which is applied in Chapter 5 to investigate the electronic structure properties of thoria bulks and flat surfaces in systems with fewer than 100 atoms. However, to model interfaces such as grain boundaries, we must use a significantly larger number of atoms, which necessitates using force fields in the simulations. It is particularly important to understand the formation of complex interfaces and the segregation of defects at these interfaces in materials that are used as nuclear fuels, where many impurities and interstitials are continually being created through radioactive decay.

As research interest in thoria continues to increase and more molecular dynamics studies are conducted, there is a clearly defined need for reliable interatomic potentials. Much research already exists into potentials for $UO_2$ and as nuclear fuels research move towards a blend of uranium and thorium dioxides, it is expected that more studies will be published investigating $ThO_2$ potentials. Several atomistic studies already exist that attempt to determine an accurate interatomic potential for thoria. These studies span several decades

and there is still no widely used form of Buckingham potential for $ThO_2$. A study published in May 2012 developed eight interatomic potentials to test against previously published potentials and compared the results to experimental data where available (Behera & Deo 2012). Over time, these newly developed potentials may prove popular. However, we have developed a new Th-O potential, detailed at the end of this section, for use in modeling uranium-doped $ThO_2$ grain boundaries.

In 1963, Benson et al used a Born-Mayer interatomic potential model Equation **(3-1)** to investigate the cohesive and surface energies of thoria (Benson et al. 1963). However, as discussed in previous sections, experimental data regarding the bulk properties of $ThO_2$ was unpublished at the time Benson et al. were carrying out their work, which forced their use of approximations based on available experimental data for other ionic oxides. Ultimately this did not result in an interatomic potential that suitably reproduced the now-known properties of thoria. In a wide-ranging study of defects in ionic solids in 1979, Mackrodt et al used interatomic potentials to calculate the lattice energy, compressibility, and lattice parameter of $ThO_2$, however, details of the potential parameters were not published (Mackrodt & Stewart 1979). Similarly, Colbourn and Mackrodt investigated the defect structure of $ThO_2$ in 1983, again without publishing the details of the interatomic potential used in their calculations (Colbourn & Mackrodt 1983). In 1985, Lewis et al investigated potentials for ionic oxides (Lewis & Catlow 1985). Retaining the $O^{2-}$-$O^{2-}$ interaction published by Catlow in

1977 for $UO_2$, potentials of the Born-Mayer type describing the cation-anion interaction were derived for oxides, including thoria (Catlow 1977).

$$V_{B-M} = Ae^{-r/\rho} \quad \textbf{(3-1)}$$

More recently, Nadeem et al have derived a series of interatomic potentials for binary oxides using a core-shell model, including thorium dioxide (Nadeem et al. 2001). These Buckingham potentials of the form:

$$V_{Buck}(r_{ij}) = A_{ij}e^{\frac{-r_{ij}}{\rho_{ij}}} - \frac{C_{ij}}{r_{ij}^6} \quad \textbf{(3-2)}$$

were fitted using an empirical least squares fitting method, which involved fitting the calculated and experimental properties via least squares.

Experimental data used include lattice parameters and the elastic and dielectric constants. However, the calculated values for $ThO_2$ were not in good agreement with the experimental results. A molecular dynamics study of gadolinia-doped $ThO_2$ was undertaken by Osaka et al in 2007 (Osaka et al. 2007). The potentials used were fit to experimental data regarding the thermal expansion of the $ThO_2$ lattice.

Further testing of the interatomic potentials of Nadeem et al and Osaka et al were undertaken by Behera and Dao in 2012 (Behera & Deo 2012). For the sake of consistency, from here on in this chapter, the potentials derived by

Nadeem and Osaka will be referred to using the notation of Behera et al. The potentials of Nadeem and Osaka shall be referred to as the NASHK and OAKUY potentials. Behera and Dao also developed eight new interatomic potential models to describe thoria using the General Utility Lattice Program (GULP) (Gale 1997; Gale & Rohl 2003). In GULP, least squares fitting was used to fit experimental values of the lattice parameter and the elastic and dielectric constants to the calculated values, a similar methodology to the one we employed. These new potentials were tested against the results of NASHK and OAKUY, which were all tested against available experimental data. The eight new Behera and Dao potentials, referred to as BD01-BD08, took several forms, including Buckingham (Equation (3-3), the so-called Buckingham-4 (Equation **(3-4)** through (3-7), and Buckingham + Morse (Equation (3-8), outlined below.

$$V_{Buck}(r_{ij}) = A_{ij}e^{\frac{-r_{ij}}{\rho_{ij}}} - \frac{C_{ij}}{r_{ij}^6} - \frac{D_{ij}}{r_{ij}^8} \quad \textbf{(3-3)}$$

$$V_{Buck-4}(r_{ij}) = A_{ij}e^{\frac{-r_{ij}}{\rho_{ij}}} \text{ if } r_{ij} \leq r_1 \quad \textbf{(3-4)}$$

$$V_{Buck-4}(r_{ij}) = 5th\ order\ polynomial \text{ if } r_1 < r_{ij} \leq r_{min} \quad \textbf{(3-5)}$$

$$V_{Buck-4}(r_{ij}) = 3rd\ order\ polynomial \text{ if } r_{min} < r_{ij} \leq r_2 \quad \textbf{(3-6)}$$

$$V_{Buck-4}(r_{ij}) = -\frac{C_{ij}}{r_{ij}^6} \text{ if } r_{ij} > r_2 \quad \textbf{(3-7)}$$

$$V_{Buck+Morse}(r_{ij}) = D_{ij}\left\{\left[1 - \exp\left(-\beta_{ij}(r_{ij} - r_{ij}^{*})\right)\right]^{2} - 1\right\} \quad \textbf{(3-8)}$$

where $r_{ij}$ is the distance between ions i and j, and A, ρ , C, $r_1$, $r_{min}$, $r_2$, D, β, and $r_{ij}$* are free parameters representing the pair-wise repulsion. The charges used in each potential are the formal ionic charges, q(Th) = +4.0 and q(O) = -2.0 $e^-$, except for OAKUY, BD06, and BD08. These three potentials were calculated using partial charges. OAKUY and BD06 used values of q(Th) = +2.4 and q(O) = -1.2 $e^-$, while BD08 used q(Th) = +2.7 and q(O) = -1.35 $e^-$.

Behera et al evaluated ten potentials, NASHK and OAKUY, along with BD01-BD08 for suitability in the investigation of the elastic properties, phase stability, point defects, defect complexes, and surface stability of $ThO_2$. OAKUY, BD03-05, and BD07-08 all performed acceptably, according to Behera, in all tests.

In April 2015, Ma et al published a new Born-Mayer-Huggins (BMH) potential to be used in combination with the Partially Ionic Model (PIM) for $ThO_2$ (Ma et al. 2015). BMH potentials have been adapted from the original equations proposed by Born, Mayer, and Huggins in the 1930s for modeling alkyl halides (Born & Mayer 1932; Mayer 2004; Huggins & Mayer 1933). These modified BMH potentials are widely used to successfully model oxide glasses, particularly silicates and borates, and Arima et al have used potentials of this form in simulations of $UO_2$ and plutonium dioxide ($PuO_2$) (Delaye et al. 1997; Arima et al. 2005; Arima et al. 2010). Ma et al have used a modified Born-Mayer-Huggins potential with the Partially Ionic Model of the form:

$$V_{PIM} = \frac{z_i z_j e^2}{r_{ij}} + f_0(b_i + b_j)\exp\frac{a_i + a_j - r_{ij}}{a_i + a_j} - \frac{c_i c_j}{r_{ij}^2} \quad \textbf{(3-9)}$$

where z is the effective partial electronic charge of each ion *i* and *j*, e is the electronic charge, r is the interatomic distance, $f_0$ is an adjustable parameter, and a, b, and c are parameters fit to experimental data.

Early potentials, such as those used by Benson et al to study surface energies of thoria, were developed prior to the publication of experimental data on the bulk properties of $ThO_2$ and therefore relied on estimating those properties from other ionic oxides (Benson et al. 1963). Later studies either failed to publish the potential parameters or did not reproduce the available experimental data closely (Mackrodt & Stewart 1979; Colbourn & Mackrodt 1983; Nadeem et al. 2001). While several good $ThO_2$ potentials were published by Behera, et al in 2012, we have specifically developed a thoria potential for use in simulating uranium-doped systems, where the uranium-oxygen interactions are described by the well-established $UO_2$ potential of Catlow (Osaka et al. 2007; Behera & Deo 2012; Catlow 1977).

## 3.2 Methodology

There has been extensive debate in the literature as to the correct values of the elastic constants and bulk modulus of thorium dioxide, which will be discussed in later sections in this chapter. In order to ensure our force fields would accurately describe Th-O interactions, we thoroughly evaluated the available published

experimental and theoretical data for its suitability in fitting a new potential and for comparison with the results of any new potentials. This is in contrast to other recent potentials that have been published without making available all of the experimental data which has been used in the calculations and have used other theoretical values in evaluating the accuracy of the new potential model.

In particular many values of the bulk modulus have been proposed but after evaluating the available literature, in this work we have used the experimental value of 198 ± 2 GPa determined by Idiri et al using energy dispersive x-ray diffraction (EDXRD) for fitting the potential (Idiri et al. 2004). This value is in good agreement with another experimental value published at the same time by Staun Olsen et al. This group studied the bulk modulus of thoria with high-pressure x-ray diffraction (XRD) and synchrotron radiation, finding a value of 195 ± 2 GPa (Staun Olsen et al. 2004). We also used the experimentally determined elastic constants of Macedo et al in the potential fitting, as these elastic constants are the most widely accepted single crystal experimental values of the elastic constants in the available literature (Macedo et al. 1964).

We have developed a new thorium-oxygen Buckingham-type potential. The least-squares fitting was done in GULP using experimental data from Idiri and Macedo (Idiri et al. 2004; Macedo et al. 1964). The oxygen-oxygen interaction is described by the potential published by Catlow, whereas initial values of A and ρ were taken from the Catlow U-O Buckingham potential (Catlow 1977). Due to the similarities between urania and thoria, these values provided a good starting

point for potential parameters used in the derivation of a Th-O potential. We tested many possible fitting parameters, including fitting the A and ρ parameters separately, and found our best fit to experimental data when allowing A and rho to fit simultaneously.

## 3.3 Results

The parameters for this new Th-O interatomic potential are introduced below in Table 3-1. The O-O interaction is taken from the potential of Catlow (Catlow 1977).

**Table 3-1 Charge on each species and parameters for the Buckingham potential employed in this study (Th-O, this work; U-O, O-O, from Catlow 1977)**

| **Species** | **Charge (e)** | | **Spring constant (eV Å$^{-2}$)** |
|---|---|---|---|
| | core | shell | |
| Th | +4.000 | - | - |
| U | +4.000 | - | - |
| O | +2.400 | -4.400 | 292.98 |
| **Buckingham Potential** | ***A* (eV)** | **ρ (Å)** | ***C* (eV Å$^6$)** |
| Th—$O_{shell}$ | 1281.775 | 0.3910 | 0.0 |
| U—$O_{shell}$ | 1217.800 | 0.3871 | 0.0 |
| $O_{shell}$—$O_{shell}$ | 22764.300 | 0.1490 | 112.2 |

## 3.3.1 Reproduction of the Lattice Constants

Using the new force field, the calculated lattice parameter of 5.600 Å, is in excellent agreement with the experimental value of 5.6001 Å (Idiri et al. 2004). One test of the potential involved varying the lattice parameter of $ThO_2$ and then calculating the energies with DFT using VASP and using the new interatomic potential in GULP. The thoria structure was optimized using the generalized gradient approximation with Hubbard U correction (GGA + U) and the exchange-correlation functionals of Perdew, Burke, and Ernzerhof (PBE) in VASP, with a cutoff energy of 600 eV and Monkhorst-Pack grid of 6x6x6 k-points (J. P.

Perdew et al. 1996). Further details of the VASP calculations performed on $ThO_2$ are discussed in more depth in Chapter 5. The lowest energy structure should be the one with the experimental lattice parameter of 5.6001 Å. Additionally, the plot of the results calculated with the potential in GULP should be in agreement with DFT results calculated in VASP. This is indeed the case as seen Figure 3-1 and Figure 3-2, though the energy values are different, the slopes of the curves are the same and both methods find a minimum at the experimental lattice parameter of 5.6 Å.

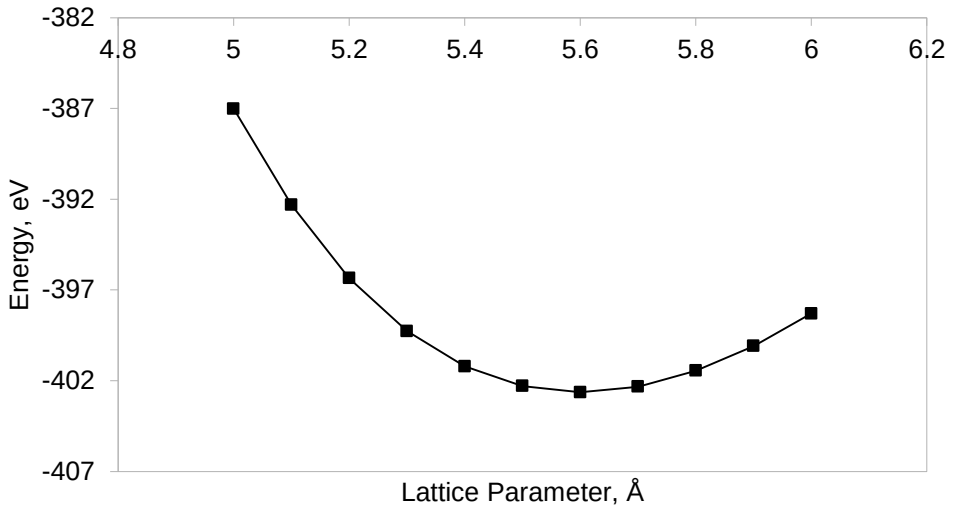


**Figure 3-1 Total energy vs. the lattice parameter, calculated in GULP.**

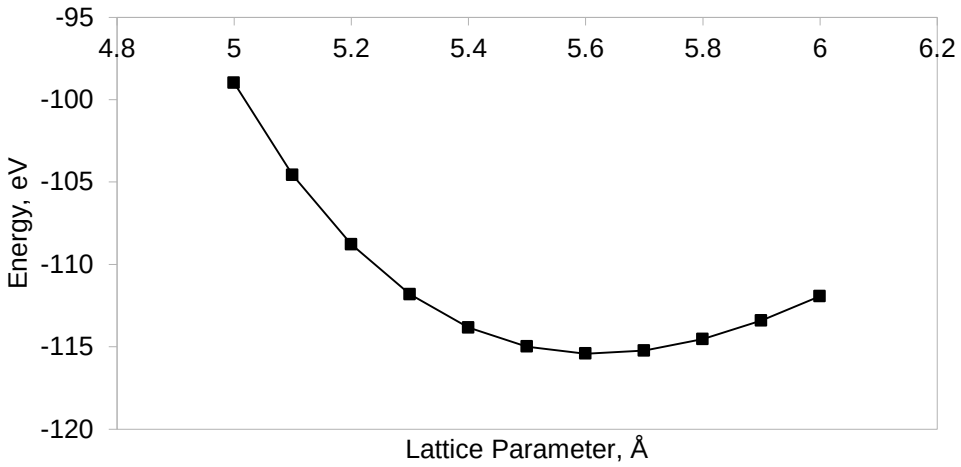


**Figure 3-2 Total energy vs. the lattice parameter, calculated in VASP.**

### 3.3.2 Agreement of the Elastic Constants with Literature Values

Table 3-2 below compares the elastic constants of $ThO_2$ calculated using the newly developed potential presented here with available experimental data. There is good agreement with the elastic properties. By using the shell model proposed by Dick and Overhauser (Dick & Overhauser 1958), we are able to correctly model the Cauchy violation of the elastic constants, where $C_{12} \neq C_{44}$, which is observed in fluorite structures. The third elastic constant, $C_{44}$, proved very difficult to match to the experimental value of Macedo et al while still retaining the good agreement observed in the other properties evaluated. Therefore, we have accepted this small deviation in the interest of improved accuracy in other parameters of system.

**Table 3-2 The elastic constants of thoria calculated with the new potential compared with the available experimental data (Macedo et al. 1964) and the error between the two values.**

| $ThO_2$ | Experimental Value (Macedo et al. 1964) | Calculated Value | % Error in Calculated Value |
|---|---|---|---|
| Elastic Constant $C_{11}$ (GPa) | 367 | 389.5 | 6.14 |
| Elastic Constant $C_{12}$ (GPa) | 106 | 114.9 | 8.36 |
| Elastic Constant $C_{44}$ (GPa) | 79.7 | 65.8 | -16.72 |

The three independent elastic constants of cubic $ThO_2$, $C_{11}$, $C_{12}$, and $C_{44}$, have been measured twice throughout the years. Macedo et al used a pulse echo technique to measure the velocity of 45 MHz sound waves through a single thoria crystal to determine the three constants (Macedo et al. 1964). The elastic constants $C_{11}$, $C_{12}$, and $C_{44}$ were found to be 367, 106, and 79.7 GPa, respectively. Clausen also conducted single crystal studies of $ThO_2$ in 1987 by inelastic neutron scattering (Clausen et al. 1987). This method yielded values of 377, 146, and 89 GPa. The results of these and other studies are summarized in Table 3-3. Theoretical investigations into the elastic constants of cubic $ThO_2$ increased dramatically in number during a five-year period between 2005 and 2010. These studies were mostly in agreement with the experimental values determined by Macedo in 1964, although there were some discrepancies in the calculated value of $C_{12}$.

In 2005, Terki et al undertook a theoretical study of the structural and electronic properties of $ThO_2$ using the WIEN2k code to implement the full potential linearized augmented plane wave (FP-LAPW) method with the generalized gradient approximation (GGA) of Perdew and Wang (GGA-92) (Terki et al. 2005; Schwarz & Blaha 2003; Perdew & Wang 1992). Terki determined the independent elastic constants, $C_{11}$, $C_{12}$, and $C_{44}$, to be 355, 105, and 54 GPa, respectively. Just a year later, Kanchana et al compared the elastic constants as calculated with the all electron full-potential linear muffin-tin orbital (FP-LMTO) with exchange-correlation potential approximated by the local density approximation (LDA) and GGA (Vosko et al. 1980; Kanchana et al. 2006). Values of $C_{11}$, $C_{12}$, and $C_{44}$ using the FP-LMTO-LDA were reported to be 405, 134, and 84, respectively. When compared to Macedo's experimental data, the FP-LMTO-GGA methodology was found to give the best agreement, with reported values of $C_{11}$, $C_{12}$, and $C_{44}$ as 376, 110, and 61 GPa, respectively. Kanchana's FP-LMTO-GGA calculations compare more favorably to the experimental data than the FP-LAPW methodology employed by Terki.

Continuing interest in computational investigations into the elastic properties of $ThO_2$ resulted in another two publications in the span of a few years. Shein et al used the WIEN2k code to implement the same FP-LAPW methodology used earlier by Terki, only this time applying the GGA as published by Perdew, Burke, and Ernzerhof (Shein et al. 2007; J. P. Perdew et al. 1996). However, the values calculated by Shein et al differed significantly from those of Terki, with $C_{11}$, $C_{12}$,

and $C_{44}$ equaling 315, 73.1, and 75.7 GPa, respectively. Finally, in 2010, Wang et al reported the elastic constants of cubic thorium dioxide as calculated with DFT using the GGA as implemented in VASP (Kresse & Hafner 1993; Kresse & Hafner 1994; Kresse & Furthmüller 1996b; Kresse & Furthmüller 1996a; J. Perdew et al. 1996; Wang, Shi, et al. 2010). The values of $C_{11}$, $C_{12}$, and $C_{44}$ were found to be 350, 111, and 70.6 GPa, respectively. When compared to the original experimental values determined by Macedo in 1964, the computational methodology of Wang better reproduced this data than the other theoretical studies previously undertaken. Using our potential, we have calculated values for the elastic constants of 389.5, 114.9, 65.8 (Table 3-2), which are in excellent agreement with the experimentally determined values of Macedo.

**Table 3-3 Experimental and theoretical vales of the elastic constants of cubic thoria in GPa, presented chronologically.**

| Group | Year | Method | $C_{11}$ | $C_{12}$ | $C_{44}$ |
|---|---|---|---|---|---|
| Macedo | 1964 | Experimental | 367 | 106 | 80 |
| Clausen | 1987 | Experimental | 377 | 146 | 89 |
| Terki | 2005 | Theoretical | 355 | 105 | 54 |
| Kanchana | 2006 | Theoretical | 405 | 134 | 84 |
| Kanchana | 2006 | Theoretical | 376 | 110 | 68 |
| Shein | 2007 | Theoretical | 315 | 73 | 76 |
| Wang | 2010 | Theoretical | 350 | 111 | 71 |
| *This work* | 2015 | Theoretical | 390 | 115 | 66 |

In 1983, Colbourn and Mackrodt calculated the elastic constants of thoria as a part of a larger study into the defect properties of the material. Additionally, Nadeem et al developed a number of interatomic potentials for binary oxides, including $ThO_2$. The fitting of these potentials involved the computation of the

elastic constants, among other parameters. Similarly, Behera et al recently computed elastic constants as a means to test the accuracy of a variety of interatomic potentials. The results of these studies have been discussed previously in section 3.1. These studies have used the elastic constants and other bulk properties to validate the results of calculations carried out using interatomic potentials, rather than focusing on the elucidation of these properties.

### 3.3.3 Prediction of the Bulk Modulus Compared to Literature Values

The bulk properties of thoria have been the subject of debate for several decades, most particularly the zero pressure bulk modulus. Our potential calculates the bulk modulus to be 206 GPa and the shear modulus to be 94 GPa (Table 3-4). This is in good agreement with widely accepted experimental values. There have been few experimental values published for $ThO_2$ and a significant number of theoretical calculations.

**Table 3-4 Calculated properties using the new interatomic potential as compared to experimental values.**

| $ThO_2$ | Experimental Value (Idiri et al. 2004) | Calculated Value (this work) | % Error in Calculated Value |
|---|---|---|---|
| Bulk Modulus (GPa) | 198 | 206 | 4 |
| Shear Modulus (GPa) | 98 | 94 | -4 |

Results from previous experimental measurements and theoretical calculations in the literature are summarized in Table 3-5. There is a very large range of values and therefore a careful analysis of previous studies must be made to select an accurate value of the bulk modulus to use in the derivation of a new potential. Starting from the elastic constants of thoria, the bulk modulus, *B*, can be calculated from the Voigt-Reuss-Hill approximation (Voigt 1928; Reuss 1929; Hill 1952). To calculate the Voigt bulk modulus, $B_{Voigt}$, and the shear modulus, $G_{Voigt}$:

$$B_{Voigt} = \frac{(C_{11} + 2C_{12})}{3} \quad \textbf{(3-10)}$$

$$G_{Voigt} = \frac{(C_{11} - C_{12} + 3C_{44})}{5} \quad \textbf{(3-11)}$$

The Reuss bulk, $B_{Reuss}$, and shear moduli, $G_{Reuss}$ for cubic crystals are given by the equations:

$$B_{Reuss} = B_{Voigt} \quad \textbf{(3-12)}$$

$$G_{Reuss} = \frac{5(C_{11} - C_{12})C_{44}}{[4C_{44} + 3(C_{11} - C_{12})]} \quad \textbf{(3-13)}$$

The Hill approximations for both the bulk and shear moduli are simply the arithmetic mean of the Voigt and Reuss values. The bulk modulus of thoria should be determined precisely by these equations, as the Voigt and Reuss calculations yield the same result. In 1964, Macedo experimentally calculated a value of the bulk modulus of a single crystal of thoria to be 193 GPa. Kelly and Brooks used thoria lattice parameters and total energy to perform DFT calculations using the linear muffin tin method to arrive at a bulk modulus value of 290 GPa (Kelly & Brooks 1987). Further experimental work in 1990, conducted by Dancausse et al, found the bulk modulus of thoria, when measured by energy dispersive x-ray diffraction (EDXRD), to be 262 GPa (Dancausse et al. 1990). While this value is in line with the earlier theoretical work of Kelly and Brooks, it is a significant departure from the value determined by Macedo in the 1960s.

In 1994, theoretical calculations carried out using the Hartree-Fock method by Harding et al arrived at a value of 175 GPa (Harding et al. 1994). At this point in time, there were two experimental values of the bulk modulus and two

theoretical values. A different type of theoretical calculation supported each experimental value. Li et al. undertook further theoretical calculations in 2002, and the results fell in between values previously calculated by Kelly and Harding (Li et al. 2002). Li et al used the all electron full-potential linear muffin-tin orbital (FP-LMTO) approach with GGA to arrive at a zero pressure bulk modulus of $ThO_2$ of 221 GPa (Savrasov 1996; J. P. Perdew et al. 1996). This result did not resolve the questions as to the true value and research interest in the topic remained high.

In 2004, two studies were published that attempted to settle this multi-decade debate. Staun Olsen et al conducted both experimental computational analysis of the behavior of $ThO_2$ under pressure. By using high-pressure x-ray diffraction (XRD) and synchrotron radiation, the pressure-volume relationship was established, allowing the bulk modulus to be calculated using the Birch-Murnaghan equation of state, which governs the finite elastic strain of cubic crystals, where P is the pressure, V is the volume, $B_0$ is the bulk modulus, and $B'_0$ is the first derivative of $B_0$ (Birch 1947).

$$P(V) = {}^{3}/_{2}\, B_0[\left(\frac{V_0}{V}\right)^{7/3} - \left(\frac{V_0}{V}\right)^{5/3}\left\{1 + {}^{3}/_{4}\,(B_0' - 4)\left[\left(\frac{V_0}{V}\right)^{2/3} - 1\right]\right\} \quad \textbf{(3-14)}$$

The result of the XRD experiment was a bulk modulus value of 195 ± 2 GPa. Staun Olsen et al conducted computational studies using the full-potential linear muffin-tin orbital (FP-LMTO) approach, where the exchange-correlation

functional is approximated using both the local density approximation (LDA) and the generalized gradient approximation (Savrasov 1996; Vosko et al. 1980; J. Perdew et al. 1996). The FP-LMTO-LDA approach predicted a bulk modulus of 225 GPa, while the FP-LMTO-GGA calculation predicted 198 GPa. The LDA approach underestimated the lattice parameter of the cubic fluorite thoria cell and therefore overestimated the bulk modulus. The accuracy of the FP-LMTO-GGA calculation in finding the experimentally determined lattice parameter accounts for the more accurate bulk modulus result. These calculations agreed strongly with both the XRD experimental results obtained at the same time and with the earliest experimental work by Macedo. The second study to be published on the matter in 2004 was by Idiri et al who determined the bulk modulus of thoria to be 198 ± 2 GPa using EDXRD (Idiri et al. 2004). In this high-pressure study of $ThO_2$, the compressibility of the fluorite cubic phase was studied up to a pressure of 20 GPa and the zero pressure bulk modulus was then calculated using the Birch-Murnaghan equation of state, in the same manner as Staun Olsen et al We have taken the experimental bulk modulus value of Idiri for our experimental reference in Table 3-4.

Another theoretical study was conducted in 2006 by Kanchana et al using the all electron FP-LMTO approach as described in the previous section (Kanchana et al. 2006). Kanchana co-authored the study undertaken by Staun Olsen et al in 2004 and repeated much of the same methodology, with the same results, in this study. These calculations were carried out using both LDA and GGA

methodologies at a theoretical equilibrium volume of the crystal as done previously by Staun Olsen et al and were able to reproduce the FP-LMTO-LDA result of 225 GPa and the FP-LMTO-GGA of 198 GPa. As Staun Olsen previously found and Kanchana confirmed, the LDA calculation underestimated the lattice parameter and therefore the equilibrium volume, $V_0$, while the GGA approach calculated the $V_0$ to be slightly higher than the known experimental value.

Given the relationship between the bulk modulus, B, and the equilibrium volume, V, given by the Murnaghan Equation (3-15), using $V_0$ from the experimental lattice parameter of 5.969 determined by Staun Olsen et al, the difference between FP-LMTO-LDA and FP-LMTO-GGA is reduced (Murnaghan 1944; Staun Olsen et al. 2004)

$$B(V) = B(V_0)\left(\frac{V_0}{V}\right)^{B'} \quad \textbf{(3-15)}$$

When using the experimental equilibrium volume, the FP-LMTO-LDA was found to be 189 GPa and the FP-LMTO-GGA to be 204 GPa. Overall, the FP-LMTO-GGA approach, using a theoretical equilibrium volume, most closely agreed with the published experimental values of Macedo, Staun Olsen, and Idiri. Using our potentials, we have found a value of the bulk modulus very close to that of Kanchana, which is good agreement with experiment.

Further DFT calculations were conducted by Wang et al to determine the bulk and shear moduli of thoria using the GGA of Perdew, Burke, and Wang, as implemented in the Vienna *ab initio* simulation package (VASP) (J. Perdew et al. 1996; Kresse & Furthmüller 1996b). The theoretical calculations gave a value for the bulk modulus of 191 GPa, which is in line with previous experimental and theoretical results.

When the bulk modulus of many of the actinides was first measured experimentally via the EDXRD experimental technique, the methodology did not give accurate bulk moduli values. The presence of silicone oil caused the results of these early EDXRD studies to significantly overestimate the value of the bulk modulus. Later, Idiri et al would go back and revisit and improve upon the EDXRD experimental data obtained previously by Dancausse and Benedict for thoria in order to correct for the use of silicone oil in the experiment (Idiri et al. 2004). Ultimately they arrived at an experimental value that is in agreement both with current theoretical calculations and the sound wave experimental data of Macedo from the 1960s. Reported calculations of the bulk modulus of $ThO_2$ in the 1960s-1990s ranged from 193 – 290 GPa. Given the wide range of values calculated through the years, further experimental results would be helpful in supporting the currently accepted value of 195-198 GPa.

**Table 3-5 Summary of thorium dioxide bulk modulus values.**

| Group (Year) | Method | Bulk Modulus (GPa) |
|---|---|---|
| Macedo (1964) | Experimental | 193 |
| Kelly & Brooks (1987) | Theoretical | 290 |
| Dancausse & Benedict (1990) | Experimental | 262 |
| Harding (1994) | Theoretical | 175 |
| Li (2002) | Theoretical | 221 |
| Staun Olsen (2004) | Theoretical | 225 |
| Staun Olsen (2004) | Theoretical | 198 |
| Staun Olsen (2004) | Experimental | 195 |
| Idiri (2004) | Experimental | 198 |
| Terki (2005) | Theoretical | 189 |
| Kanchana (2006) | Theoretical* | 225 |
| Kanchana (2006) | Theoretical* | 198 |
| Kanchana (2006) | Theoretical** | 189 |
| Kanchana (2006) | Theoretical** | 204 |
| Shein (2007) | Theoretical | 193 |
| Wang (2010) | Theoretical | 191 |
| *This work* | Theoretical | 206 |

*Values from Kanchana were calculated from the theoretical equilibrium volume of $ThO_2$.

** Values from Kanchana were calculated from an experimental equilibrium volume of $ThO_2$.

To thoroughly understand the mechanical stability and behavior under pressure of any material, bulk properties such as the lattice parameter, elastic constants, and bulk modulus are important factors that must be known with a high degree of confidence. Mechanical stability of a crystalline material is achieved by satisfying equations relating stability to the elastic constants (and thus the bulk and shear moduli) as given in Equations (3-16) through (3-19) below (Wang et al. 1993). A cubic crystal may generally be considered stable where all of the independent elastic constants are positive numbers.

$$(C_{11} - C_{12}) > 0 \quad \textbf{(3-16)}$$

$$(C_{11} + 2C_{12}) > 0 \quad \textbf{(3-17)}$$

$$C_{11} > 0 \quad \textbf{(3-18)}$$

$$C_{44} > 0 \quad \textbf{(3-19)}$$

Aside from the obvious practical advantages of knowing the bulk properties of a material, these values are useful in assessing the accuracy and validity of computational models in materials science. When using DFT, the generalized gradient approximation consistently proved more effective at reproducing experimental data than the local density approximation. However, we are able to use the new Th-O interatomic potential here to calculate the bulk properties of thoria. The ability to reproduce bulk properties is a key component of most models and interatomic potentials.

## 3.4 Conclusions

We have developed a novel interatomic potential to describe the interaction between Th-O in $ThO_2$ by using least squares fitting in GULP and fitting to available experimental data, where the O-O interaction is described by the potential developed by Catlow. This $ThO_2$ potential correctly models the Cauchy violation ($C_{12} \neq C_{44}$) observed experimentally in thoria and is in excellent agreement with experimental data. While other good Th-O potentials have been published previously, we have specifically fit and optimized this potential for use with a leading $UO_2$ potential, making it particularly useful in the study of thorium-based MOX fuel materials. We have used this potential to successfully model $ThO_2$ and $Th_{1-x}U_xO_2$ bulk materials, surfaces, and grain boundaries, and in a detailed study of the configurational and thermophysical properties of these systems, the results of which are presented in the following chapters of this thesis. While this potential is optimized for use with $UO_2$, it is excellent for modeling pure thoria and we believe it will be useful when modeling other doped thoria systems.

# Chapter 4

# Configurational Analysis of Uranium-doped Thorium Dioxide

## 4.1 Introduction

We have completed a configurational analysis of the thermophysical uranium-doped thorium dioxide using the Th-O potential we developed (Chapter 3). While thorium is a fertile material, it is not fissile and therefore a sustained conversion to the fissile $^{233}U$ isotope can only occur in the presence of a neutron source. Although plutonium and uranium may serve as the source, there are several advantages to blending thoria with urania that have been confirmed experimentally, including changes in the decay heat, melting point, and thermal conductivity of the material, in addition to a decrease in the release rate of

fission gases despite an actual increase in the production of fission gases (Herring et al. 2001).

As previously mentioned in Chapter 1, thoria has the fluorite structure, which is shared with the dioxides of, for example, cerium, plutonium, and uranium. Since a neutron source is required for application as a nuclear fuel, and as $ThO_2$ and $UO_2$ are isostructural, there is significant interest in thoria-urania solid solutions, both experimentally and theoretically (Banerjee et al. 2012; Dash et al. 2009; Martin et al. 2012; Kandan et al. 2009). As it is useful to study thoria in the context of uranium doping, it is important to have reliable computational methods for these materials due to the safety hazards and high costs of conducting experiments on radioactive materials.

In experimental test reactors using thorium fuels, typically only small concentrations of uranium or plutonium are used, in the region of 5-15%. The role of U or Pu in these fuel blends is not as a fuel itself but rather as a neutron source for the production of $^{233}U$ by $^{232}Th$. To model such small concentrations of uranium dopant in thoria, we need a sufficiently large system, which requires the use of affordable computational methods based on interatomic potentials. We now apply here the new interatomic potential presented in the previous chapter. We have applied this model to the study of uranium distribution in $ThO_2$ supercells.

However, we are not aware of any robust theoretical investigations into the different possible configurations of uranium substitution in thoria, which might elucidate the distribution of the uranium atoms serving as a neutron source in a thorium dioxide nuclear fuel and the thermodynamic properties of these configurations. It is important to understand how uranium behaves when inserted into thoria as part of an effort to understand how large-scale MOX fuel rods may behave. Since thorium has no further oxidation states beyond $Th^{4+}$, $UO_2$ is more susceptible to oxidation than $ThO_2$, and so any uranium clustering at surfaces or grain boundaries could lead to oxidation and thereby compromise the corrosion-resistance of the material. In this chapter, we present the results of our investigation into the numerous independent configurations obtainable at a variety of uranium concentrations in $ThO_2$ using the interatomic potential from Chapter 3 to describe the interaction between thorium and oxygen in this system.

## 4.2 Methodology

### 4.2.1 Energies and Geometries

The energies of different configurations of the mixed solid were evaluated using the General Lattice Utility Program (GULP) (Gale 1997; Gale & Rohl 2003). GULP implements the Born model of solids, which assumes that the ions in the crystal interact via short-range repulsive interactions, longer-range attractive interactions, and long-range Coulombic interactions (Born & Huang 1954). The short-range energy contribution due to interactions between each particle and all

others is summed within a predetermined cut-off. The contribution of the long range electrostatic forces is summed using the Ewald sum (Ewald 1921). The electronic polarizability of ions is included via the shell model of Dick and Overhauser in which each of the polarizable ions, in this case the oxygen atoms, are represented by a core and a massless shell, connected by a spring (Dick & Overhauser 1958). The polarizability of the model ion is then determined by the spring constant and the charges of the core and shell. The advantage of using the shell model is that it better reproduces the elastic and dielectric properties of ionic solids than rigid ion models, though it increases the computational cost of the simulations (Upadhyay 2008).

The parameters of the interatomic potentials describing the interactions between Th-O, U-O, and O-O used in this study are given in Table 3-1. In order to make geometry predictions in GULP, the lattice energies are minimized with respect to the structural parameters, until the forces acting on the ions are all less than 0.001 eV $Å^{-1}$. All structures reported are the result of constant pressure energy minimizations, where not only the ionic positions but also the cell parameters are allowed to vary to find the energy minimum. The external pressure was set to zero in all calculations.

### 4.2.2 Representation of the solid solutions

The $Th_{1-x}U_xO_2$ solid solutions were represented by a symmetry-adapted ensemble of configurations in a supercell, using the methodology implemented

in the Site Occupancy Disorder (SOD) program (Grau-Crespo et al. 2004; Grau-Crespo et al. 2007), which has been employed previously in the simulation of a range of mineral solid solutions, including carbonates, oxides and sulfides. Successful applications of SOD include a study of the thermophysical properties of carbonates, investigations into the mixing thermodynamics of oxides and a simulation of cation distribution and thermodynamics in sulfides (Grau-Crespo et al. 2007; Ruiz-Hernandez et al. 2010; Wang et al. 2011; Benny et al. 2009; Grau-Crespo et al. 2010; González-López et al. 2014; Haider et al. 2012; Seminovski et al. 2012). This program generates the complete configurational space for each composition in a supercell of the structure, before extracting the subspace of symmetrically inequivalent configurations, for which energies and other properties are evaluated. In this case a 2x2x2 thoria supercell (Figure 4-1b and c) was used as the base simulation cell, and we have worked with uranium concentrations up to x = 0.16. The computational cost of investigating higher U concentrations in a system of this size was considerable and of limited practical concern, as the amount of uranium-doping required in thoria fuels is small. However, to investigate the full range of the solid solution and derive thermodynamic properties that can be compared with experimental values, a full configurational analysis was carried out on a 1x1x2 supercell (Figure 4-1a).

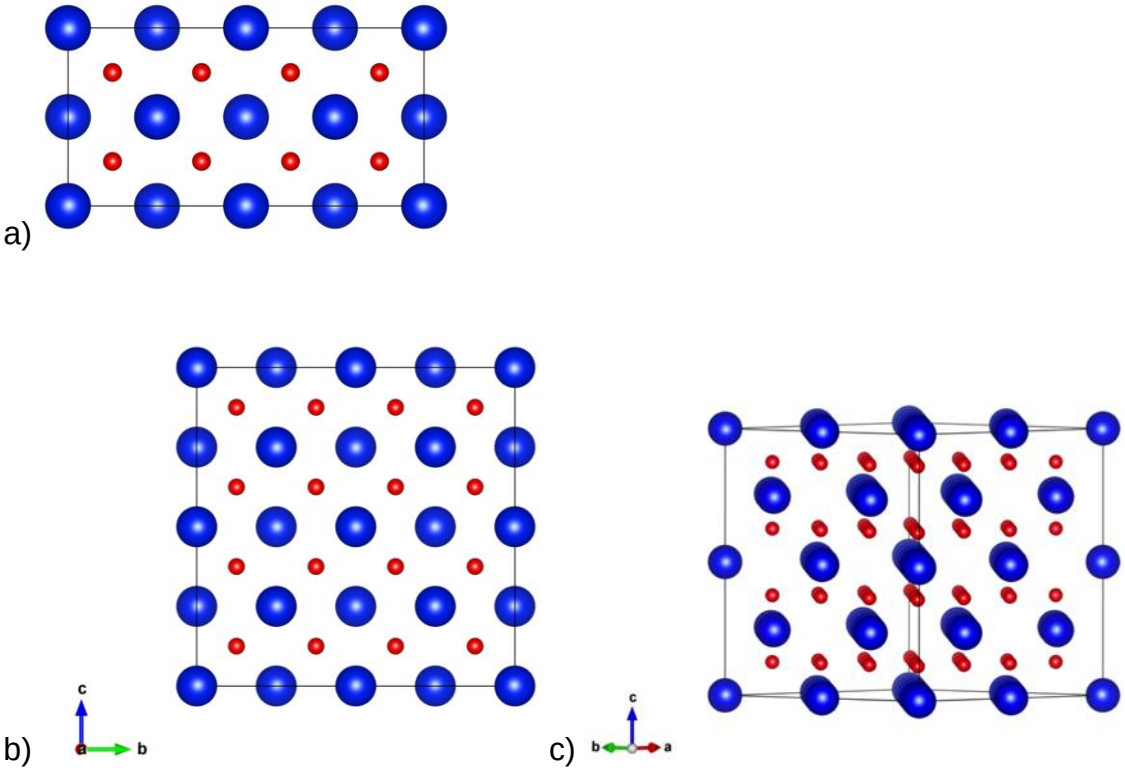


**Figure 4-1 a) 1x1x2 supercell and b) and c) 2x2x2 supercell face and side views of $ThO_2$, where the Th atoms are represented by the blue spheres and the O atoms are represented by the red spheres.**

Once the configurational spectrum is obtained, it is possible to derive thermodynamic properties through further application of statistical mechanics. In the simplest formulation, the extent of occurrence of one particular configuration, *n*, in the disordered solid in configurational equilibrium at a temperature *T* can be described by a Boltzmann-like probability, $P_n$:

$$P_n = \frac{1}{Z} exp\left(-E_n/k_B T\right) \quad \textbf{(4-1)}$$

where $E_n$ is the energy of configuration *n* and Z is the partition function given by the following equation:

$$Z = \sum_{n=1}^{N} exp\left(-E_n/k_B T\right) \quad \textbf{(4-2)}$$

The energy of the system is now calculated as a sum as follows:

$$E = \sum_{n=1}^{N} P_n E_n \quad \textbf{(4-3)}$$

Then in the reduced configurational space, a new probability can be determined for an inequivalent configuration, *m*. This is calculated from the energy of that configuration, $E_m$, and its degeneracy $\Omega_m$ (the number of times that the configuration is repeated in the complete configurational space):

$$P_m = \frac{\Omega_m}{Z} exp\left(-E_m/RT\right) = \frac{1}{Z} exp\left(-E_{m(red)}/k_b T\right) \quad \textbf{(4-4)}$$

where m=1,…, M (M is the number of inequivalent configurations), R is the gas constant, and Z is the partition function (Equation **(4-5)**, which guarantees that

the sum of all the probabilities equals 1 and also gives access to the calculation of configurational free energies and entropies.

$$Z = \sum_{m-1}^{M} exp\left(-E_m/_{RT}\right) \quad \textbf{(4-5)}$$

$E_{m(red)}$ is the reduced energy and relates to the energy $E_m$ and the reduced, or degeneracy, entropy, $S_m$, via:

$$E_{m(red)} = E_m - TS_m \quad \textbf{(4-6)}$$

$$S_m = k_B T ln\Omega_m \quad \textbf{(4-7)}$$

From this relationship, it is possible to compare the inequivalent configurations as the degeneracy and the energies are considered. For two inequivalent configurations of the same energy, the one with the highest degeneracy will then have the higher degeneracy entropy and therefore a lower reduced energy and thus higher probability (Equation **(4-4)**. It is possible in this way to obtain temperature-dependent configurational thermodynamic functions and equilibrium degrees of disorder (Grau-Crespo et al. 2009; Ruiz-Salvador et al. 2013; Smith et al. 2010). In this work we have focused on the distribution of uranium in a range of concentrations in the thoria lattice and the derivation of thermodynamic properties of the solid solution.

The configurational free energy *G* of the disordered solid can be obtained directly from the partition function:

$$G = -kT \ln Z \tag{4-8}$$

and any average observable, including the enthalpy *H* of the solution, can be estimated using configurational averaging:

$$H = \sum_{m=1}^{M} P_m H_m \tag{4-9}$$

Having obtained the enthalpy and free energy of the solid solution, it is useful to evaluate the enthalpy of mixing:

$$\Delta H_{mix} = H[Th_{1-x}U_xO_2] - (1-x)H(bulk\ ThO_2) - xH(bulk\ UO_2) \tag{4-10}$$

which can be compared with experimental calorimetric determinations, and the free energy of mixing:

$$\Delta G_{mix} = G[Th_{1-x}U_xO_2] - (1-x)G(bulk\ ThO_2) - xG(bulk\ UO_2) \tag{4-11}$$

which can also be found experimentally from equilibrium composition measurements.

Technically important properties like the thermal linear expansion coefficient, α, can be calculated:

$$\alpha = \frac{1}{a_{293}} \frac{\partial a}{\partial T} \quad \textbf{(4-12)}$$

where a is the lattice parameter of the cell at a given temperature, T, and $a_{293}$ is the lattice parameter at 293 K. The values of *a* at seven temperatures were calculated directly in GULP followed by fitting the values to a 3rd order polynomial to enable the extrapolation to higher values. As noted, due to the computational cost of calculating the configurational thermodynamics for the full $ThO_2$-$UO_2$ solid solution using the large 2x2x2 supercell, a 1x1x2 cell was used instead for these calculations.

**Table 4-1 Polynomial fit for $ThO_2$ and $UO_2$** $\boldsymbol{a_T(\text{Å}) = c_0 + c_1 T + c_2 T^2 + c_3 T^3}$

| **Material** | $c_0$ | $c_1 \times 10^5$ | $c_2 \times 10^8$ | $c_3 \times 10^{12}$ | $\alpha_{293}$ |
|---|---|---|---|---|---|
| **$ThO_2$** | 5.60793 | 2.79036 | 1.46253 | -3.43684 | 5.608 |
| **$UO_2$** | 5.45337 | 2.54896 | 1.45446 | -3.76733 | 5.462 |
| **$Th_{0.87}U_{0.13}O_2$** | 5.58811 | 2.93563 | 1.23247 | -2.01114 | 5.598 |
| **$Th_{0.75}U_{0.25}O_2$** | 5.56882 | 2.71268 | 1.70802 | -4.78603 | 5.578 |

GULP will also calculate certain thermodynamic properties of a system when a phonon calculation is performed. We have taken advantage of this fact to extract the specific heat capacities at constant volume of our system while computing phonons, where the constant volume heat capacity, $C_v$, is calculated from the vibrational partition function, $Z_{vib}$:

$$C_v = RT\left(2\left(\frac{\partial lnZ_{vib}}{\partial T}\right) + T\left(\frac{\partial^2 lnZ_{vib}}{\partial T^2}\right)\right) \quad \textbf{(4-13)}$$

$$Z_{vib} = \sum_{k-points} w_k \sum_{all\ modes} (1 - \exp(-\frac{hv}{kT})^{-1} \quad \textbf{(4-14)}$$

## 4.3 Results

### 4.3.1 Thermal Expansion of Thorium Dioxide

It is important to have a thorough understanding of the temperature-dependent properties of any nuclear fuel in order to understand and predict its behavior. For example, the thermal expansion must be understood before the fuel rods and cladding are designed (Olander 1976). If the fuel-cladding gap is either too small or too large, failure of the fuel cladding can occur. If the gap is too small, as the fuel expands, pressure is exerted on the cladding and deformation of the fuel can occur. If the gap is too large, the fuel material may vibrate excessively and so damage the cladding (Olander 2009).

We have calculated the value of the thermal linear expansion coefficient, α, for thoria at 6.4 $\times 10^{-6}$ $K^{-1}$ at 300 K. This value is in line with the experimental values reported by Marples (7.3 $\times 10^{-6}$ $K^{-1}$), Kempter and Elliot (8.2 $\times 10^{-6}$ $K^{-1}$), and, at 293K, Yamashita et al (8.43 $\times 10^{-6}$ $K^{-1}$) (Marples 1976; Kempter & Elliott 1959; Yamashita et al. 1997). While our thermal expansion coefficient does underestimate the values found experimentally, this could be explained by the small difference in the initial lattice parameters used in the experimental systems and in our system. We have used a value for the lattice parameter, a, of $ThO_2$ of 5.6 Å in our simulations, whereas Kempter found an initial a value of 5.597 Å and Yamashita one of 5.58 Å. As $ThO_2$ does not undergo much expansion with temperature, it is possible that by using a larger initial lattice parameter, our calculations failed to account for a small amount of expansion and so underestimate the coefficient of thermal expansion. It should also be noted that Kempter reported impurities in his original samples of $ThO_2$ and these could have had a non-negligible effect on the experimental values reported.

A computational study based on Density Functional Theory (DFT) by Lu et al reports values at higher temperatures, i.e. α of 33–37 $\times 10^{-6}$ $K^{-1}$, an order of magnitude above the values determined experimentally and that are estimated by our simulation (Lu et al. 2012). Martin et al have used a rigid ion potential in molecular dynamics simulations to calculate an α of 9.2 $\times 10^{-6}$ $K^{-1}$ at 1500 K, which is in the same range as our value and the experimental values but this method does not account for the polarizability of the ions or the contribution of

phonons in their simulation (Martin et al. 2012). Similarly, using a Born-Mayer-Huggins potential with a partially ionic model, Ma et al have calculated an α at 1500 K of 11.9 $\times 10^{-6}$ $K^{-1}$ (Ma et al. 2015). These calculated values at 1500 K are lower than the experimental values reported at 1200 K of Yamashita et al and that at 1273 K of Kempter and Elliot. These findings indicate that interatomic potentials used to determine the coefficient of linear expansion tend to underestimate the values but are of the same order of magnitude as experiment and a distinct improvement on the values obtained from DFT for this material.

### 4.3.2 Configurational Variations in U-Substituted Thorium Dioxide

Thoria has a cubic fluorite unit cell with 4 cation sites in the unit cell. $U^{4+}$ (1.00 Å) has a smaller ionic radius than $Th^{4+}$ (1.05 Å) (Shannon 1976). The equilibrium geometries and energies of the U-substituted configurations were calculated both with and without considering vibrational effects. The SOD code identified a number of independent configurations for the uranium-doped thoria systems under investigation (Table 4-2). The number of inequivalent configurations increases significantly with each additional substitution until a U mole fraction of x = 0.5 is reached in the 1x1x2 supercell.

The variation of the lattice parameter, a, with the mole fraction, x, in the $ThO_2$–$UO_2$ solid solutions modeled follow Vegard's law (Figure 4-2), in good agreement with the experimental measurements of Hubert et al and Banerjee et al (Hubert et al. 2006; Banerjee et al. 2012). We can further compare our

models with these data by examining the cation-anion and cation-cation distances of Th—O, U—O, Th—Th, and U—U (Figure 4-4 and Figure 4-5).

**Table 4-2 The total number of geometry configurations and the number of inequivalent configurations found with SOD using 1x1x2 and 2x2x2 supercells**

| Supercell | $Th_{(1-x)}U_xO_2$ | Mole fraction of Uranium, x | Total Number of Configurations | Total number of Inequivalent Configurations |
|---|---|---|---|---|
| 1x1x2 | $Th_7U_1O_{16}$ | 0.125 | 8 | 1 |
| | $Th_6U_2O_{16}$ | 0.25 | 28 | 4 |
| | $Th_5U_3O_{16}$ | 0.375 | 56 | 4 |
| | $Th_4U_4O_{16}$ | 0.5 | 70 | 8 |
| | $Th_3U_5O_{16}$ | 0.625 | 56 | 4 |
| | $Th_2U_6O_{16}$ | 0.75 | 28 | 4 |
| | $Th_1U_7O_{16}$ | 0.875 | 8 | 1 |
| 2x2x2 | $Th_{31}U_1O_{64}$ | 0.031 | 32 | 1 |
| | $Th_{30}U_2O_{64}$ | 0.063 | 496 | 5 |
| | $Th_{29}U_3O_{64}$ | 0.094 | 4960 | 14 |
| | $Th_{28}U_4O_{64}$ | 0.125 | 35960 | 71 |
| | $Th_{27}U_5O_{64}$ | 0.156 | 201376 | 223 |
| | $Th_{26}U_6O_{64}$ | 0.188 | 906192 | 874 |
| | $Th_{25}U_7O_{64}$ | 0.219 | 3365856 | 2706 |

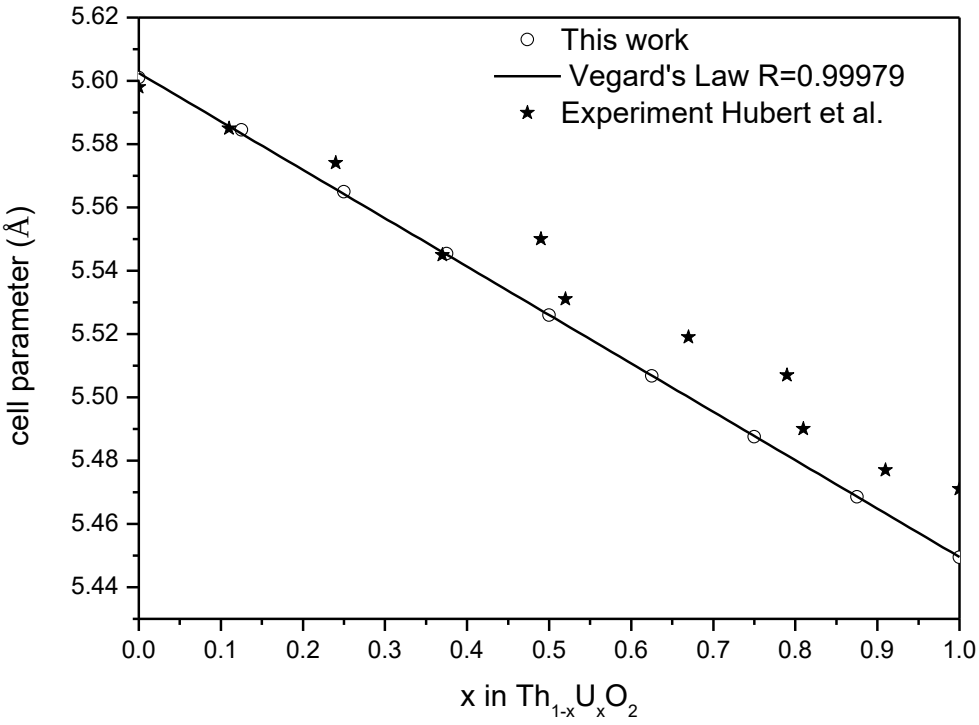


**Figure 4-2 Comparison of the cell parameter vs composition with Vegard's law**

Before we consider the distances in the full $ThO_2$–$UO_2$ solid solution, it is useful to examine the effect of a single uranium atom substitution in the thoria supercells. While the 1x1x2 supercells is of practical use in modeling the full solid solution, we observe that our values of the interatomic distances at x = 0.13 are higher than the experimental values at this mole fraction of uranium (Figure 4-4 and Figure 4-5). To investigate why this might be, we have investigated the effects of a single uranium substitution in both the 1x1x2 and 2x2x2 supercells (Figure 4-3). Of course a single substitution yields different mole fractions of uranium in the cells, where x= 0.13 in a 1x1x2 and 0.03 in a

2x2x2 supercell. However we can see from the interatomic distances in Table 4-3 that small changes are introduced to the lattice even at the lowest mole fraction of uranium we have studied, x = 0.03. While in this cell, the introduction of one U atom does not significantly affect the Th-Th or Th-O distances, the Th-U and U-O distances are smaller than the Th-Th and Th-O distances being replaced. Moving to the 1x1x2 cell, with one U substitution, all four of the possible cation-cation and anion-anion distances are affected by the presence of a uranium atom. Due to the shape of the 1x1x2 cell, a larger percentage of the oxygen atoms in the lattice are affected by the presence of uranium than in the 2x2x2 cell. These oxygen atoms are moved closer to uranium than they would be in the pure $ThO_2$ lattice, thus affecting the other interatomic distances in the small supercell, resulting in an exaggerated effect when a single substitution is introduced into a small supercell. In a larger supercell with an equivalent mole fraction of uranium, there are many available configurations. We have calculated the interatomic distances in a 2x2x2 supercell for x = 0.13 as an average of all 71 inequivalent configurations (Table 4-3). These distances more closely reproduce the experimental values of Hubert et al compared to the distances in the singly substituted 1x1x2 cell. Therefore, we consider that the overestimation of the interatomic distances at x = 0.13 in Figure 4-4 and Figure 4-5 is due to the effect of a single uranium substitution in a small simulation supercell. However, the 1x1x2 cell is able to provide a good representation of the solid solution at higher levels of uranium substitution, when the concentration is more balanced.

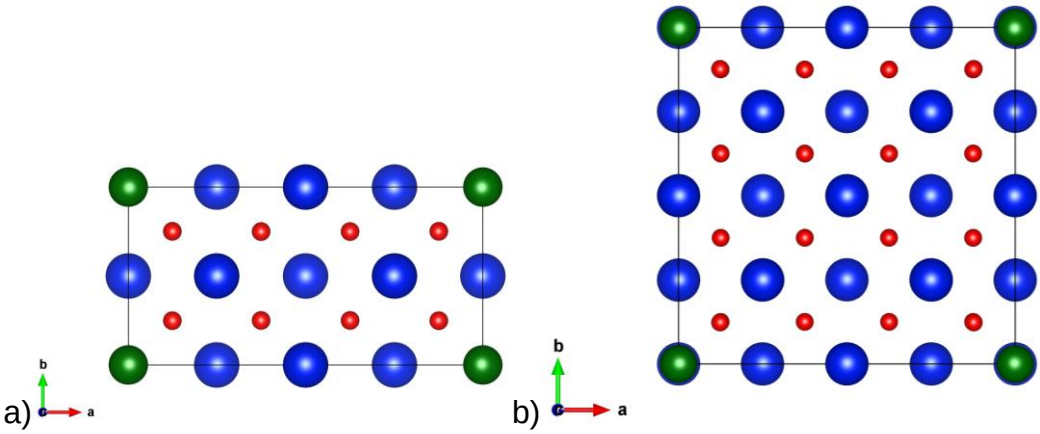


**Figure 4-3 a) $Th_7U_1O_{16}$ b) a $Th_{31}U_1O_{64}$ supercells**

**Table 4-3 Interatomic distances (Å) for pure $ThO_2$ and the 1x1x2 and 2x2x2 supercells with one uranium substitution (x = 0.13 and 0.03 respectively) and for the 2x2x2 supercell with 4 uranium substitutions (x = 0.13)**

| | Th-Th | Th-U | Th-O | U-O |
|---|---|---|---|---|
| $ThO_2$ | 3.961 | --- | 2.425 | --- |
| $Th_7U_1O_{16}$ | 3.978 | 3.970 | 2.437 | 2.422 |
| $Th_{31}U_1O_{64}$ | 3.960 | 3.948 | 2.426 | 2.389 |
| $Th_{28}U_4O_{64}$ | 3.952 | 3.940 | 2.423 | 2.386 |

As noted, to obtain the interatomic distances, we have taken the average values over all the inequivalent configurations. Overall, our Th-Th distances are slightly overestimated compared to those distances found by Hubert et al at low concentrations of U, and slightly underestimated at high U concentrations. The

U—U distances are more consistent but are underestimated across the full range of solid solutions. Hubert et al did not publish data on Th-U distances for us to use for comparison, but we have found in our calculations that the Th-U distances are greater than those of U-U but less than Th-Th for each value of x. In absolute terms all of the calculated cation-cation distances are extremely close to experiment and consistent with the fact that U is the smaller cation and that its incorporation into thoria creates stress in the lattice to maintain the four-fold coordination of the oxygen in the fluorite structure. The U—U separation is larger at low values of x. As typically only small amounts of uranium are added to a thorium-uranium MOX fuel, the larger U—U separation at these concentrations indicates that uranium does not cluster within the thoria lattice. The Th-O and U-O distances show similar behavior to the Th-Th distances, as expected from the smaller ionic radius of uranium compared to thorium.

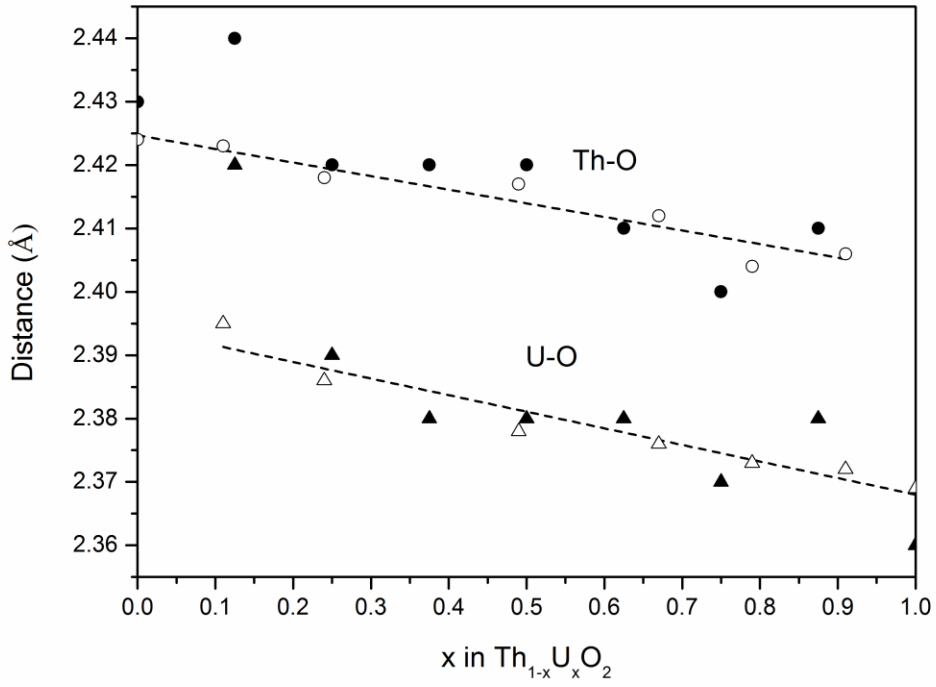


**Figure 4-4 Cation-anion distances decrease as the mole fraction, x, of the system increases. Black circles and triangles, this work; open triangles and circles, experimental data from Hubert et al (Hubert et al. 2006).**

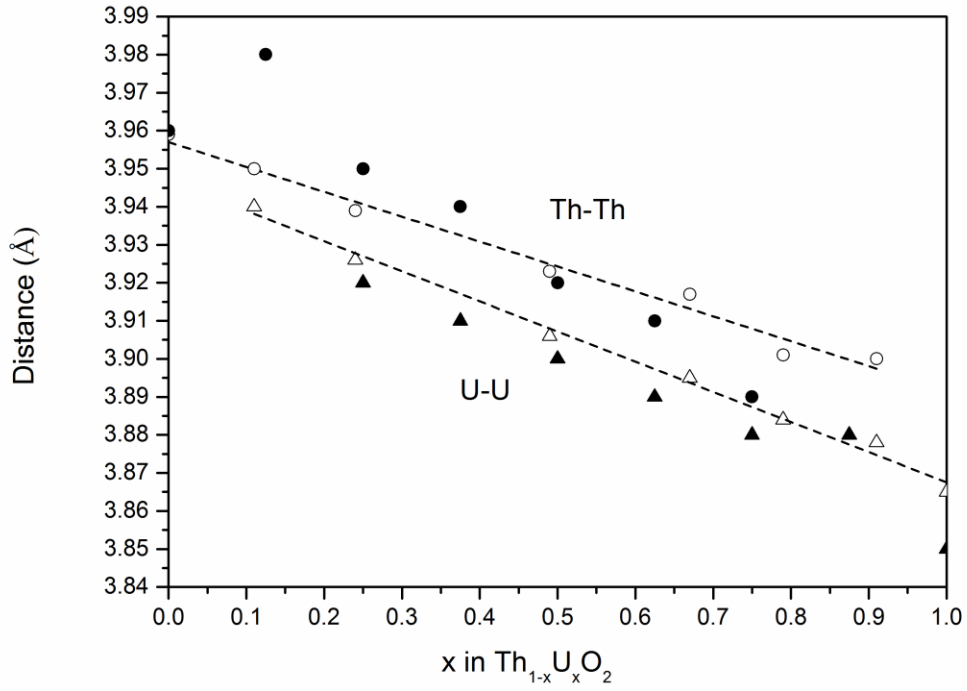


**Figure 4-5 Cation-cation distances as a function of the mole fraction of uranium, x. Black circles and triangles, this work; open triangles and circles, experimental data from Hubert et al (Hubert et al. 2006).**

To analyze the Boltzmann probability distributions, it is now useful to consider the larger 2x2x2 supercell. By using the larger cell, we can not only analyze the system at the low concentrations of uranium that are of particular interest in MOX fuels, but we can also more clearly observe any changes in the lattice that may occur on the addition of uranium. In Figure 4-6, with a mole fraction of uranium of x = 0.06, we show that configurations 4 and 5 together are clearly dominant, with probabilities of 38 and 41%, respectively. The corresponding structures may be seen in Figure 4-8. As the concentration of uranium and the

total number of inequivalent configurations increases for $Th_{29}U_3O_{64}$, there are no longer just one or two dominant configurations as illustrated in Figure 4-7.

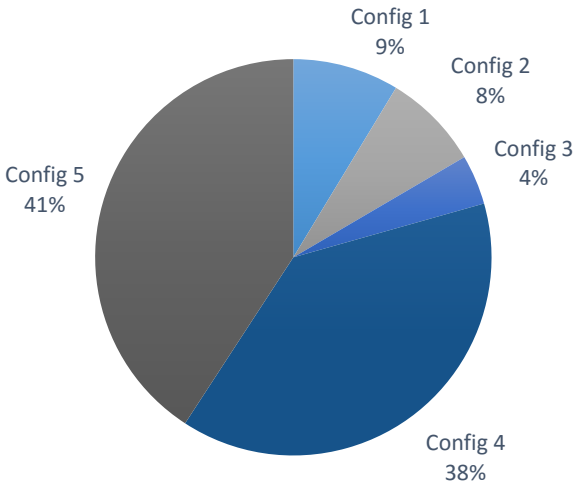


**Figure 4-6 Probability distribution of the independent configurations of $Th_{30}U_2O_{64}$ at 500 K, with values rounded to the nearest whole number**

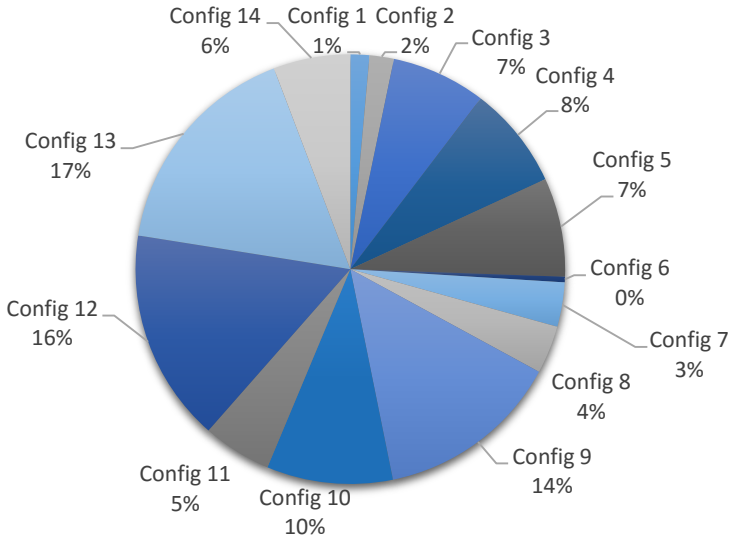


**Figure 4-7 Probability distribution of the independent configurations of $Th_{29}U_3O_{64}$ at 500 K, with values rounded to the nearest whole number**

To further analyze the relationship between the structures of the inequivalent configurations and the probabilities that a given configuration will occur at equilibrium, it is useful to examine the energies of each symmetrically inequivalent configuration. In Table 4-4, the energies of the independent configurations obtained from GULP are listed relative to the lowest energy configuration of the $Th_{30}U_2O_{64}$ (uranium mole fraction of x = 0.06) system. As shown in Table 4-4, the energies of the different configurations do not vary much, indicating that the U distribution can be expected to be fairly random. Following the simple arguments by McLean (McLean 1957) for metals and confirmed for ionic materials (de Leeuw & Parker 2000), that dopant incorporation is based on the reduction of elastic strain, the smaller U cation should be easily incorporated in the thoria lattice, which is confirmed by the lack of site preference shown by the U cations in the thoria lattice.

However it is important to consider the degeneracy, Ω, of the system, which here is the number of symmetrically equivalent configurations that can be represented by one inequivalent configuration. The energy of the degenerate system, $E_{m(red)}$, considers the degeneracy of the system and therefore differs from the energy of the corresponding structure in the full configurational space (Equations **(4-6)** and **(4-7)**. Therefore the probability of finding any one configuration must consider the energy of the degenerate system ($E_{m(red)}$) and not simply the energy of the configuration alone.

For $Th_{30}U_2O_{64}$, as noted in Table 4-2, there are 496 initial configurations that, in the reduced configurational space, yield five inequivalent configurations. The degeneracy and the relative energy of each configuration with and without considering the degeneracy ($E_{m(red)}$ and $E_m$, respectively) are presented Table 4-4. Configuration 3, which is the lowest probability configuration seen in Figure 4-6, is the structure with the lowest energy originally ($E_m$ = 0). As this configuration only occurs 16 times in total, compared to the Ω values of 48 for configurations 1 and 2 and 192 for configurations 4 and 5, configuration 3 has the highest $E_{m(red)}$ and therefore the lowest probability.

**Table 4-4 The number of times each inequivalent configuration occurs and the relative energies ($E_m$) of each of these configurations, and the relative energies when the degeneracy of the system is considered ($E_{m(red)}$) for the $Th_{30}U_2O_{64}$ supercell**

| Configuration | Degeneracy (Ω) | $E_m$ eV | $E_{m(red)}$ eV |
|---|---|---|---|
| 1 | 48 | 0.0147 | 0.0667 |
| 2 | 48 | 0.0187 | 0.0707 |
| 3 | 16 | 0 | 0.0993 |
| 4 | 192 | 0.0101 | 0.0024 |
| 5 | 192 | 0.0077 | 0 |

In the two dominant configurations at x= 0.063 and the lowest energy structure of x=0.094 (Figure 4-9), there is a distortion of the lattice. This same distortion was observed in the 2x2x2 supercells at the other concentrations considered, and can be explained by the changed cation-cation and cation-anion distances in the lower energy configurations as compared to the original lattice positions and the highest energy (lowest probability) structures. Due to the U-U and U-O distances being shorter than the corresponding Th-Th and Th-O distances, as uranium substitutions are made in the cell, oxygen atoms move closer to the U atom. This moves some of the nearby Th atoms away, as the distance between Th and O atoms is preferably longer. These movements create local distortions in those regions of the cell, particularly where two uranium atoms are close together, as observed in Figure 4-8 a) and b) and Figure 4-9. When the energies of the $Th_{29}U_3O_{64}$ (U mole fraction of x = 0.094) are considered along with the degeneracy of each independent configuration (Table 4-5), configuration 6 has the highest relative energy, both including the degeneracy of the configuration and without. The lowest energy configuration is Configuration 10, but the configurations with the lowest degenerate energy, $E_{m(red)}$, are configurations numbered 13, 12, and 9. These three structures each occur 768 times in the full configurational space, the highest degeneracy of any of the 14 independent configurations. These configurations are therefore also the three highest probability configurations, with probabilities of 17%, 16%, and 14% respectively. However, as Figure 4-7 illustrates, no single configuration is dominant at a uranium mole fraction of x = 0.094.

**Table 4-5 The degeneracy of each inequivalent configuration (the number symmetrically equivalent configurations) and the relative energies ($E_m$) of each of these configurations, and the relative energies when the degeneracy of the system is considered ($E_{m(red)}$) the $Th_{29}U_3O_{64}$ supercell**

| Configuration | Degeneracy (Ω) | $E_m$ eV | $E_{m(red)}$ eV |
|---|---|---|---|
| 1 | 96 | 0.0304 | 0.1122 |
| 2 | 96 | 0.0158 | 0.0977 |
| 3 | 384 | 0.0173 | 0.0394 |
| 4 | 384 | 0.0123 | 0.0344 |
| 5 | 384 | 0.0147 | 0.0368 |
| 6 | 32 | 0.0388 | 0.168 |
| 7 | 192 | 0.0212 | 0.0732 |
| 8 | 192 | 0.0165 | 0.0685 |
| 9 | 768 | 0.0188 | 0.0111 |
| 10 | 384 | 0 | 0.0221 |
| 11 | 256 | 0.0122 | 0.0517 |
| 12 | 768 | 0.0102 | 0.0024 |
| 13 | 768 | 0.0078 | 0 |
| 14 | 256 | 0.0054 | 0.0449 |

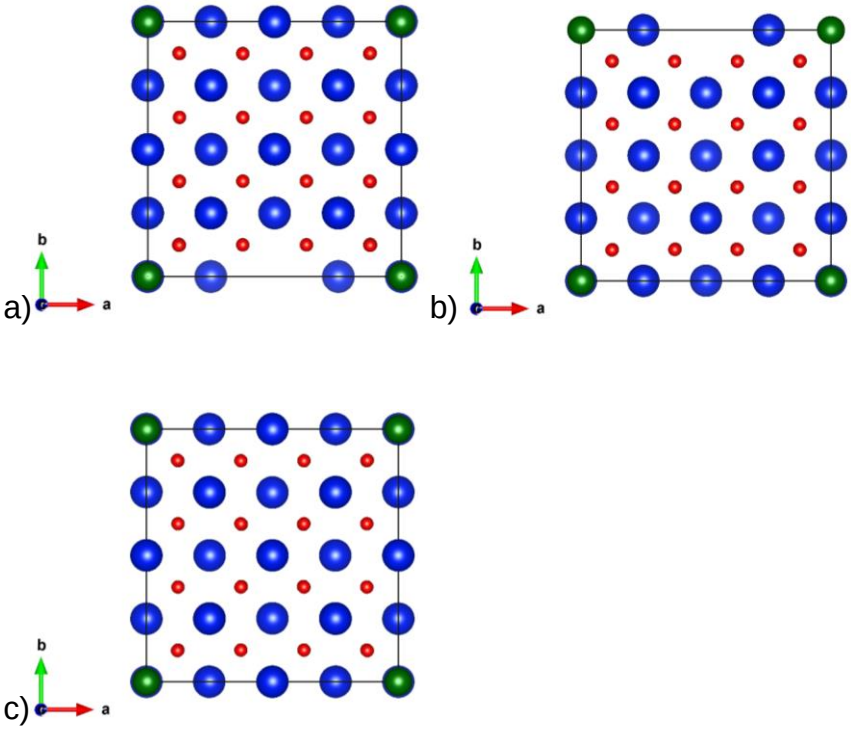


**Figure 4-8 $Th_{30}U_2O_{64}$ where Th is represented in blue, U in green, and O in red. a) Configuration 4 (38% probability); b) Configuration 5 (41% probability); c) Lowest probability structure**

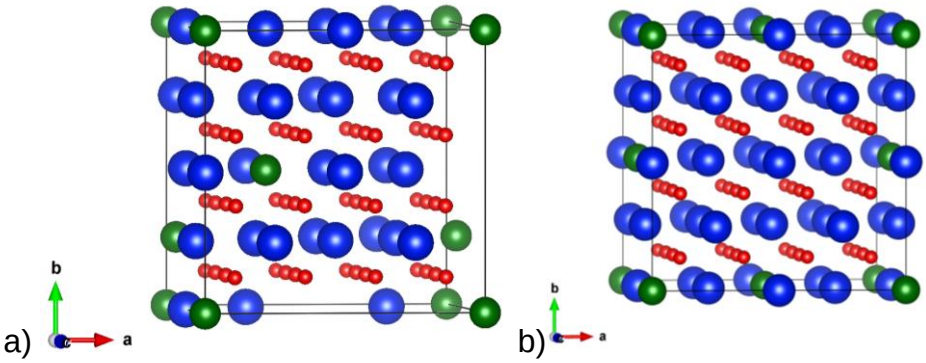


**Figure 4-9 $Th_{29}U_3O_{64}$ a) Maximum probability; b) Lowest probability**

For all concentrations of uranium investigated within the 2x2x2 supercell, there is no single dominant configuration. Above x = 0.063, there are no longer even

two dominant structures and instead several configurations share nearly equal probabilities and none of these probabilities exceed 17%. We do find that in the highest probability (lowest relative energy) configurations at all values of x, the U—U distances are smaller than these distances in the lowest probability (highest energy) configurations, but since there is a large number of possible independent configurations available in the system and no single one is dominant, including the lowest energy configuration, we predict that uranium atoms will be distributed throughout the cell without forming clusters.

### 4.3.3 Thermodynamic Properties of $Th_{(1-x)}U_xO_2$ Solid Solutions

From the average configurational enthalpies computed with the SOD code, using Equation **(4-9)**, we have calculated the enthalpies of mixing ($\Delta H_{mix}$) at several temperatures for a range of solid solutions of the 1x1x2 supercell system of $Th_{(1-x)}U_xO_2$. By using a smaller supercell than that evaluated for the configurational energies and probability, the number of inequivalent configurations and hence computational cost was reduced and the full solid solution could be calculated. All values of $\Delta H_{mix}$ are positive as shown in Figure 4-10, indicating that mixing of the two solids is endothermic. For an ideal solid solution, by definition $\Delta H_{mix} = 0$, whereas $Th_{(1-x)}U_xO_2$ deviates from an ideal solid solution, with a maximum $\Delta H_{mix}$ of approximately 2.5 $kJmol^{-1}$ near the midpoint of the solid solution range. From the values of $\Delta H_{mix}$ , we have calculated the values of $\Delta G_{mix}$ (Figure 4-11), to see if mixing is spontaneous at temperatures above 298 K. To determine the vibrational contributions to the free energy of the

system, the k-points were checked in GULP until the energy converged. We have used a k-points mesh of 2x4x4 to calculate the phonon frequencies of $Th_{(1-x)}U_xO_2$. When vibrational effects are included at 600 K (Figure 4-12), $\Delta G_{mix}$ is lowered, showing the importance of including vibrational contributions to $\Delta G_{mix}$ to obtain more accurate values. On close examination of the mixing curves in Figure 4-12, a miscibility gap is observed. However, the gap is only 0.1 $kJmol^{-1}$ without consideration of vibrational effects, decreasing to just 0.05 $kJmol^{-1}$ when vibrational contributions are included. As this miscibility gap is so small in energetic terms, we do not expect to observe the formation of two separate domains at 600 K. Additionally, a slight shift towards the lowest values of x is observed in the $\Delta G_{mix}$ curves in both Figure 4-11 and Figure 4-12 with the more thorium-rich $Th_{(1-x)}U_xO_2$ systems having a lower $\Delta G_{mix}$ than uranium-rich $Th_{(1-x)}U_xO_2$.

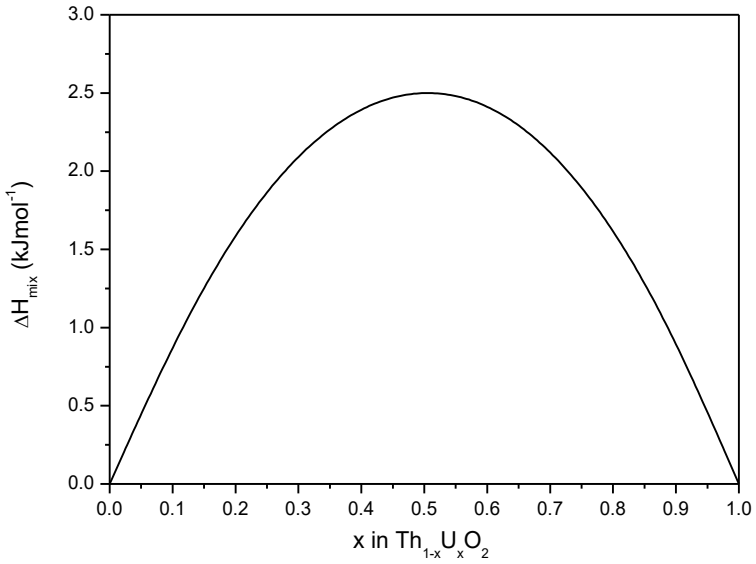


**Figure 4-10 $\Delta H_{mix}$ calculated using a 1x1x2 supercell**

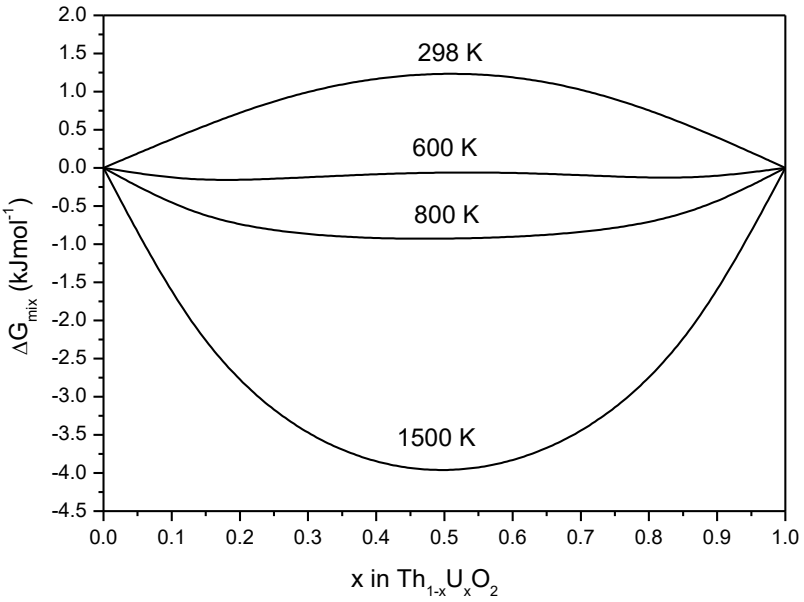


**Figure 4-11 $\Delta G_{mix}$ at different temperatures calculated for a 1x1x2 supercell, not considering vibrational effects**

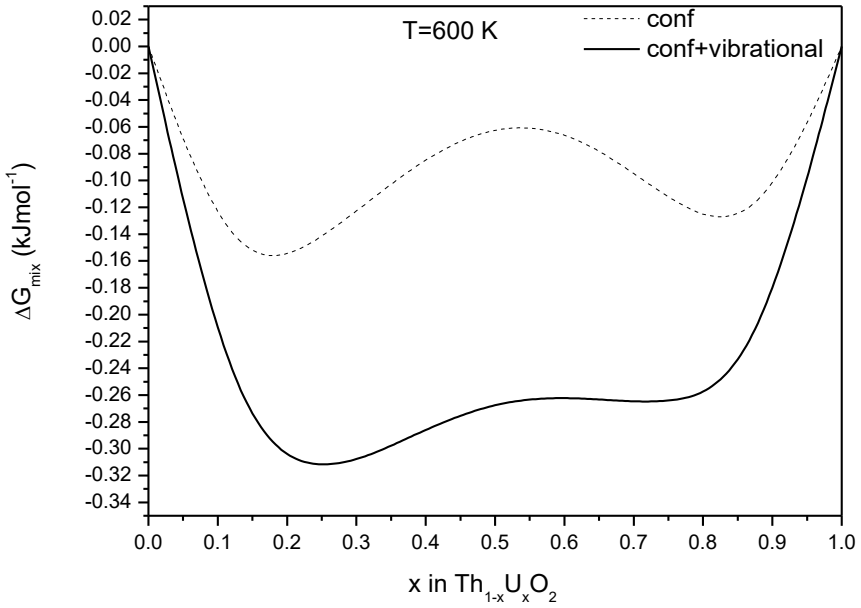


**Figure 4-12 $\Delta G_{mix}$ at 600 K showing the configurational and the configurational and vibrational effects**

Understanding the heat capacity and thermal expansion is important in any nuclear fuel material in order to predict the temperature of the fuel in the reactor. We have calculated these properties for the full range of the $ThO_2$-$UO_2$ solid solution in the 1x1x2 supercell and compared our values to those found experimentally or using other computational methodologies where available. The results of the constant-volume heat capacity calculations for the pure materials and the solid solutions are presented in Figure 4-13. As the $C_v$ values of $ThO_2$ we calculated are in line with the DFT values and have used a less compute-intensive methodology than the value found by Lu et al (Lu et al. 2012) at all temperatures studied here, we expect that this methodology will be useful in

determining $C_v$ of even lower concentrations of uranium in the $ThO_2$-$UO_2$ solid solution, or other nuclear materials.

The coefficient of thermal expansion, α, of pure thoria has been discussed in section 4.3.1, and was calculated in good agreement with experimental values, but in MOX fuels it is important to understand the effect of both cations on the thermal expansion. Generation IV reactors are typically designed to withstand temperatures up to 1873 K, so we have calculated α from room temperature (298 K) to 1900 K to represent typical operating temperatures of this fuel type. In Figure 4-14, we present the results of $Th_{(1-x)}U_xO_2$ where x= 0.125, 0.25, and 0.38 compared to $ThO_2$. The values of α are in good agreement with the pure material at all temperatures calculated. There is particularly close agreement at low temperatures, with deviation from the pure material increasing above approximately 1000 K.

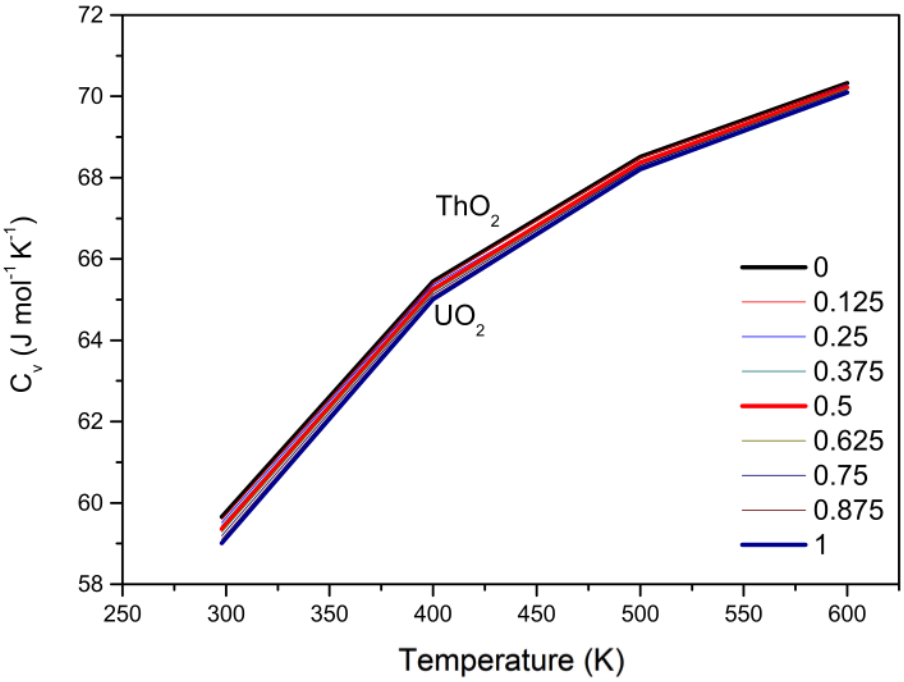


**Figure 4-13 Constant volume heat capacity of $Th_{(1-x)}U_xO_2$ solid solutions**

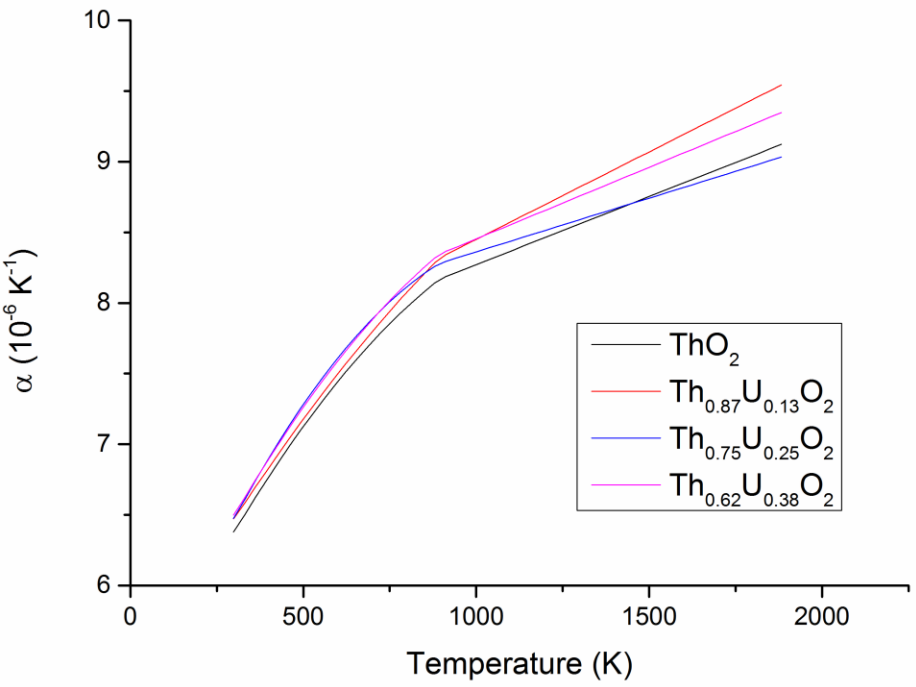


**Figure 4-14 Coefficient of thermal expansion of $Th_{(1-x)}U_xO_2$ solid solutions**

## 4.3.4 Conclusions

In this chapter we have employed the potentials developed in the previous chapter in a study of the distribution of uranium atoms in thoria supercells. Using this methodology, we have closely reproduced available experimental data for the lattice parameters and coefficient of thermal expansion.

We have shown that uranium atoms do not cluster in the bulk material but are instead distributed throughout the cell. In a $Th_{(1-x)}U_xO_2$ solid solution the enthalpy of mixing is endothermic across the full range of the solution, but while the Gibbs free energy of mixing is favorable above 600 K, when vibrational effects are

included in the calculations, the free energies of mixing show a very small miscibility gap. However, as the energy penalty is so small, we do not predict the formation of separate domains at high or low concentrations of uranium in the thoria lattice.

# Chapter 5

# DFT Study of Uranium-Substituted Thorium Dioxide

## 5.1 Introduction

We have looked at many useful thermophysical properties of thorium dioxide and thoria-urania solid solutions in Chapter 4, such as thermal expansion and the enthalpy of mixing. Now we wish to investigate the specific local effects of uranium substitution in the thoria bulk and when adding uranium to surfaces. The presence of uranium in $ThO_2$ can arise two ways, either by the deliberate addition of uranium to thoria in a mixed oxide fuel (MOX) fuel or as an impurity. As discussed in Chapter 1, the $^{232}Th$ isotope is transmuted via the addition of a neutron and a series of beta decay to the fissile $^{233}U$ isotope, which undergoes the fission required for nuclear power generation (Figure 5-1).

$$^{232}_{90}Th + neutron \rightarrow {}^{233}_{90}Th \xrightarrow{\beta- decay} {}^{233}_{91}Pa \xrightarrow{\beta- decay} {}^{233}_{92}U \rightarrow sustainable\ fission$$

**Figure 5-1 The transmutation of the most common thorium isotope into the fissile $^{233}$U isotope.**

By using Density Functional Theory (DFT), we can explore the effects of uranium dopants and impurities on the nature of the atomic bonding interactions and the charge distribution in thorium dioxide. These effects are important to understand in any material and are particularly critical in predicting the fuel behavior and integrity in nuclear reactors. In an interest to save computational resources, we have explored the density of states (DOS) of 2x2x2 supercells of the pure thoria compound along with a select number of other systems. To investigate the effects of uranium in the electron cloud of the material we have obtained the DOS plots for very low concentrations (x = 0.03, x = 0.06 and x = 0.09) of U in the $Th_{1-x}U_xO_2$ solid solution.

Several computational studies have investigated the surface chemistry of $ThO_2$, many of which focus on adsorption of water and molecular oxygen on the (111) surface (Benson et al. 1963; Skomurski et al. 2008; Behera & Deo 2012). In this chapter we have used DFT to calculate the surface energies of the three low Miller index surfaces, the (111), (110), and (100), of thoria and to simulate the scanning tunneling microscopy (STM) images of these surfaces. Furthermore, we have explored the effects of a uranium adatom on the thoria surfaces. At this time, we are unaware of any existing experimental or theoretical studies reporting STM topographies for pure $ThO_2$. While we are aware of several

studies exploring the effects of adsorbates such as $H_2O$ or $O_2$, we are not familiar with any studies into the effects of uranium adatoms on thoria surfaces at present.

## 5.2 Methodology

### 5.2.1 Simulation of Bulk Thoria Supercells

The $ThO_2$ unit cell (Figure 5-2) has the fluorite structure with a lattice parameter of 5.6 Å (Idiri et al. 2004). In this work, we have generated the 1x1x2 and 2x2x2 supercell structures of thoria, containing 24 and 96 atoms respectively (Figure 5-4). We have placed between 1 and 3 uranium atoms in each 2x2x2 supercell to simulate low-level uranium doping. The uranium atoms were positioned at the center of the simulation cell and the relaxed cells may be seen in section 5.3.1. These supercells were then optimized using spin-polarized DFT calculations implemented within VASP (Kresse & Hafner 1993; Kresse & Hafner 1994; Kresse & Furthmüller 1996b; Kresse & Furthmüller 1996a). The exchange-correlation functional of Perdew, Burke, and Ernzerhof (PBE) (J. P. Perdew et al. 1996) was used with the projector augmented wave (PAW) method to describe the core electrons and the interaction between the atomic cores and the electrons in the valence shells. For oxygen, the 1*s* electrons were kept frozen during the simulations and for thorium and uranium, electrons were frozen up to the 4*f* and 5*d* orbitals, inclusive. A kinetic energy cut-off of 600 eV was used for the plane wave basis set expansion. A gamma-centered

Monkhorst-Pack mesh of 6x6x6 k-points was used after carefully checking for self-consistency of the electronic energy at 1 x $10^{-6}$ eV.

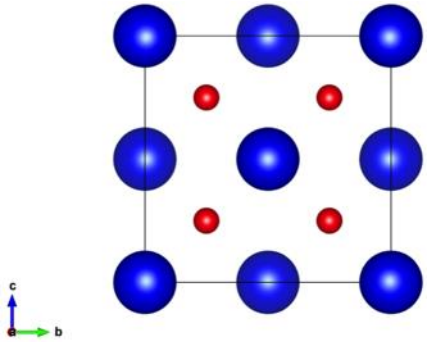


- Th atoms in blue
- O atoms in red

**Figure 5-2 $ThO_2$ unit cell**

To correct for the strong on-site Coulomb repulsion arising from the presence of *f* electrons in the actinides and to reduce hybridization with the oxygen atoms, a Hubbard Hamiltonian following the approach of Dudarev et al (Dudarev et al. 1998) was used with the Generalized Gradient Approximation (GGA + U) where:

$$E_{\mathrm{DFT+U}} = E_{\mathrm{DFT}} + \frac{U-J}{2}\sum_{\sigma} Tr[\rho^{\sigma} - \rho^{\sigma}\rho^{\sigma}] \qquad \textbf{(5-1)}$$

With $\rho^{\sigma}$ representing the density matrix, the Coulomb parameter (U) and exchange parameter (J) here are the elements of the spherically averaged matrix of the screened Coulomb interaction (Dudarev et al. 1998; J. Perdew et al. 1996; J. P. Perdew et al. 1996). For purposes of this study, U and J are not treated separately and instead the effective U parameter is considered, where:

$$U_{\text{eff}} = \text{U} - \text{J} \quad \textbf{(5-2)}$$

The value of the Hubbard parameter, $U_{eff}$, used for uranium was 4 eV, a commonly used value in other previous DFT studies, including those by Shi et al and Devey et al, which modeled the optical and elastic properties of $UO_2$ with good experimental agreement (Shi et al. 2010; Devey 2011). For Th, we investigated many different values of $U_{eff}$ using both the local-density approximation + Hubbard U correction (LDA+U) and two exchange-correlation GGA+U functionals. We found that any value of $U_{eff}$ used decreased the accuracy of the structural prediction as a whole while offering no improvement in the calculation of the density of states as compared to previous reports, when employing the GGA approximation in VASP. Figure 5-3 shows that a U value of 0 eV is preferable for modeling $ThO_2$ structural parameters and that of the three exchange-correlation functionals tested, LDA significantly underestimates the experimental lattice parameter of 5.6001 Å (Idiri et al. 2004) as compared to GGA functionals.

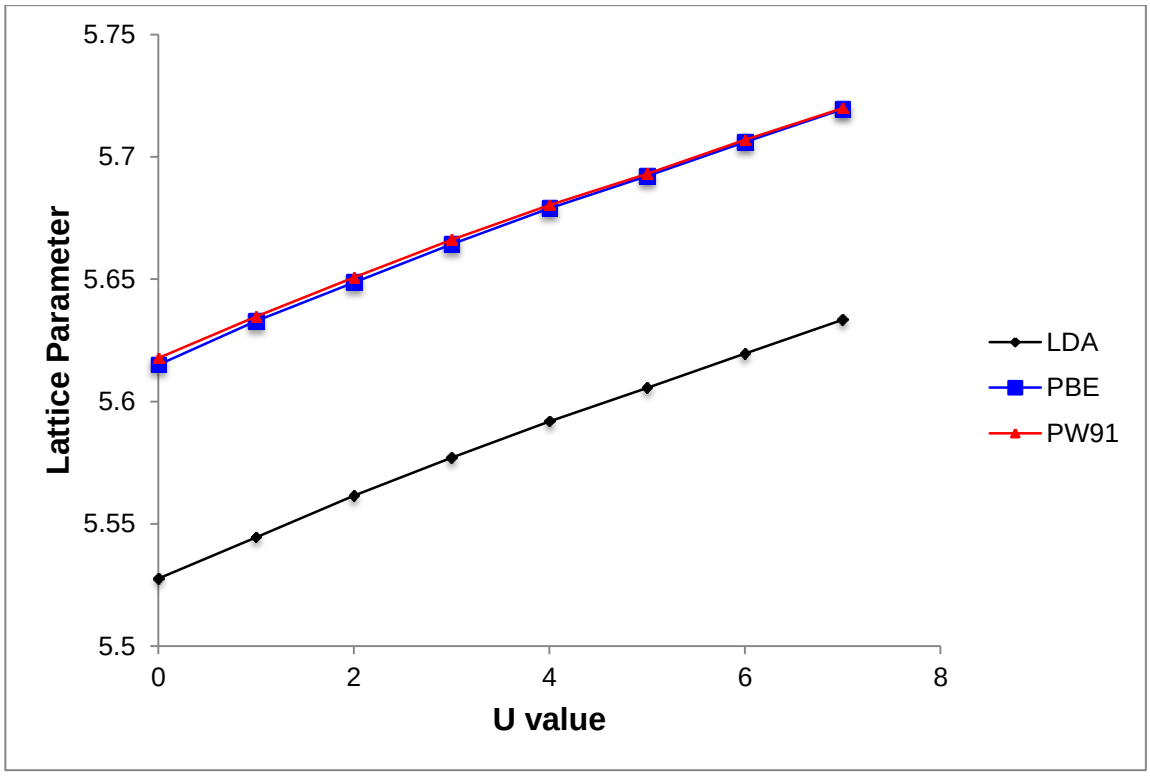


**Figure 5-3 Plot of calculated $ThO_2$ lattice parameters against the Hubbard U value using three different functionals. The experimental lattice parameter is 5.6001 Å.**

Wang et al successfully modeled $ThO_2$ using GGA and Lu et al similarly concluded that no U correction was needed for $ThO_2$ (Wang, Zhang, et al. 2010; Lu et al. 2012). This has also proven true in other DFT studies of thorium-containing compounds; for instance, ThN has been modeled using GGA+U by Lu et al (Lu et al. 2011). All of these results agree with our own conclusion that no additional structural accuracy resulted from the addition of the Hubbard U parameter. As there is no formal electron occupation of the *f* orbitals in $ThO_2$, the effect of the U parameter is negligible in DFT calculations.

Using the Site Occupancy Disorder Code (SOD), the theory and method of which are discussed in Chapter 2 and Chapter 4, we have generated a number of inequivalent configurations for each 1x1x2 supercell of $Th_{(8-x)}U_xO_{16}$ where x = 0-7 (Grau-Crespo et al. 2007). We have carried out our DFT calculations on the lowest energy configurations for each value of x, as determined in Chapter 4.

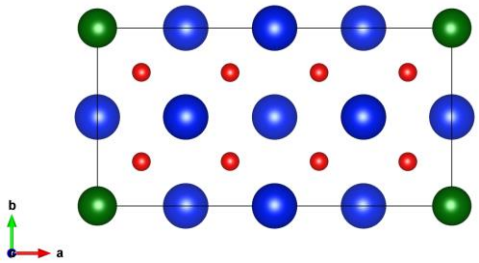


**Figure 5-4 1x1x2 supercell of $ThO_2$**

## 5.2.2 Simulation of $ThO_2$ Surfaces

Flat surfaces were generated from the geometry optimized bulk unit cell structure using METADISE (Watson et al. 1996). This approach is based off of the work of Tasker on ionic crystal surfaces, where the surface is considered to be a slab of stacked planes (Tasker 1979; Tasker 1980). Tasker described three types of surface plane stacking sequences. Each plane in a type 1 surface has anions and cations in their stoichiometric ratios and therefore there is no dipole. Type 2 surfaces consist planes A and B, stacked in repeating units of A/B/A, such that the net charge in each plane cancels any net dipole perpendicular to the surface. For example, if plane A has a charge of -1 and plane B has a

charge of +2, a surface slab stacking sequence of A/B/A/A/B/A will be non-dipolar. The final surface type, type 3, is an alternating pattern of oppositely charged planes, *e.g.* A/B/A/B, thus generating a dipole moment for this surface. By moving half of the ions of the same charge from the top to the bottom of the slab, a type 3 may be rearranged to have no net dipole perpendicular to the plane of the surface. It is important to avoid any of these dipoles, as in the presence of a dipole perpendicular to the surface planes the surface energies will diverge (Bertaut 1958). Should the surface planes be charged, these planes are arranged symmetrically to eliminate any dipole perpendicular to the surface plane. METADISE has been used to cut flat non-dipolar surfaces of many different oxides and sulfides (Watson et al. 1996; de Leeuw et al. 2000; Santos-Carballal et al. 2014; Devey et al. 2008).

The natural cleavage plane of fluorite and fluorite-type materials is the anion-terminated (111) surface (Figure 5-5), which is the most stable (Tasker 1979; Tasker 1980). In this work we model not only the O-terminated (111) surface orientation but also the O-terminated (100) and the (110) surfaces (Figure 5-6 and Figure 5-7). These three surfaces were then used for further calculations in VASP. Surface slabs comprised of nine atomic layers were used for the (111) and (100) surfaces and a slab of six layers was used to model the (110) surface. The (100) slab contained 48 atoms and the (110) and (111) slabs contained 72 atoms each. A 6x6x1 grid of k-points was used for all surface simulations. The convergence of the energy with respect to the vacuum size was carefully

checked in VASP. A vacuum layer of 15 Å was sufficient to isolate one slab and the adsorbate, where applicable, from its repeat image in the periodic calculations. Other settings were kept the same as for the bulk thoria simulations. For bulk calculations, all ions were allowed to fully relax. For the surfaces, only the ions in the top layers of the slab were relaxed while the rest were held fixed at their bulk relaxed positions. For the (111) and (100) surfaces, the top five layers were relaxed and for the (110) surface, the top three layers were relaxed. We have applied dipole corrections to our surface calculations (Makov & Payne 1995; Neugebauer & Scheffler 1992).

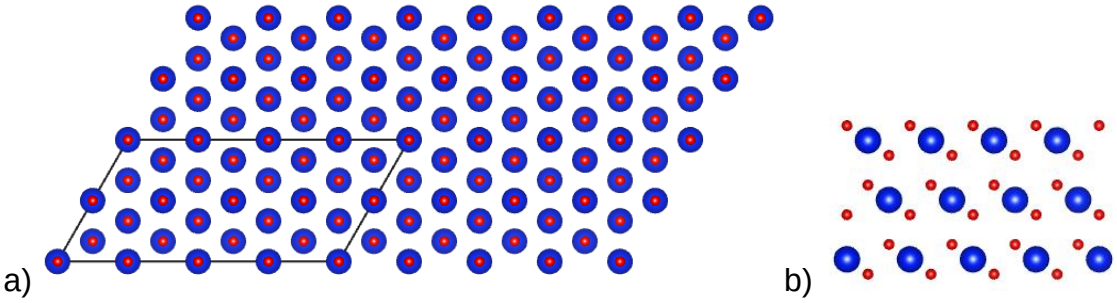


**Figure 5-5 a) top and b) side views of the oxygen-terminated (111) surface before relaxation**

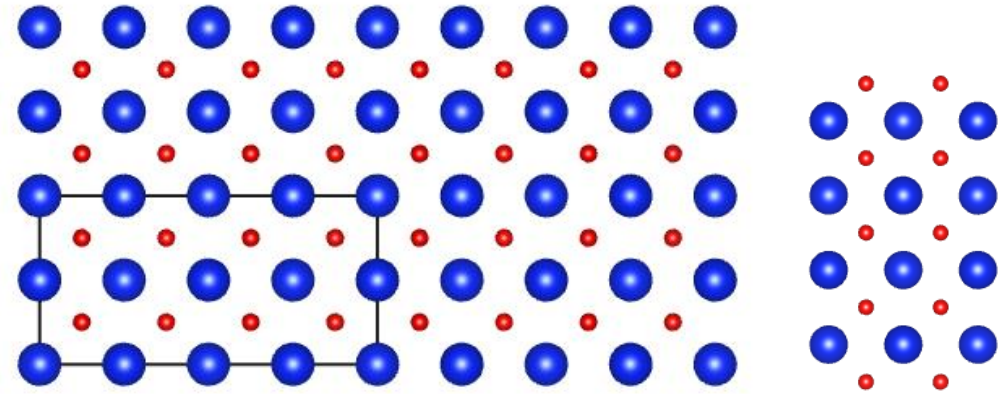

a) b)

**Figure 5-6 a) top and b) side views of the oxygen-terminated (100) surface before relaxation, with all atoms in their original positions. Thorium atoms are blue, oxygen atoms are red.**

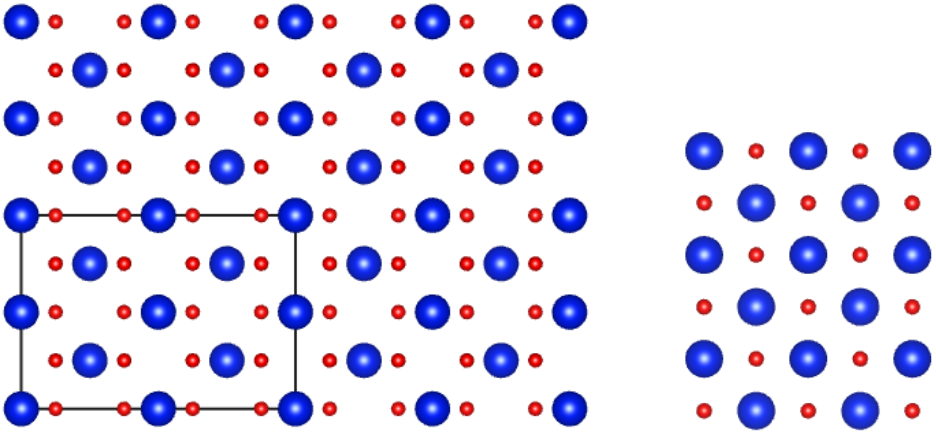

a) b)

**Figure 5-7 a) top and b) side views of the (110) surface before relaxation**

We have used the Bader (Bader 2002) charge analysis code of Henkelman et al (Henkelman et al. 2006; Sanville et al. 2007; Tang et al. 2009) to analyze the charge distribution in our systems.

### 5.2.3 Calculation of Surface Energies

We can calculate the surface energies of the (111), (110), and (100) surfaces from the surface slab energies. The surface energy represents the excess of energy of the surface as compared to the original bulk material and thus serves as a measure of the stability of the crystal surface relative to the bulk. The cleavage of the bulk to form the surface reduces the coordination of those atoms located in the surface slab. Using VASP to perform energy minimizations on each slab before allowing the atoms to relax, we can calculate the surface energy before relaxation, $\gamma_u$, for a stoichiometric and symmetric surface, with the equation:

$$\gamma_u = \frac{E_{slab,u} - E_{bulk}}{2A} \qquad \textbf{(5-3)}$$

where $E_{slab,u}$ is the energy of the unrelaxed surface slab, $E_{bulk}$ is the energy of a bulk system comprised of the same number of atoms as the surface slab, and A is the surface area of the top and bottom of the slab, which is why A is doubled in the equation. The top of the surface slabs were then allowed to relax while the bottom part of the slab remained fixed. This allows us to derive the relaxed surface energy, $\gamma_u$, given by the equation:

$$\gamma_u + \gamma_r = \frac{E_{slab,r} - E_{bulk}}{A} \qquad \textbf{(5-4)}$$

where $E_{slab,r}$ is the total energy of the relaxed surface slab. In these simulations, only the top layers of the simulation slab have been allowed to relax. It is to be expected that the relaxed surface energy will be lower than the unrelaxed surface, as all surface atoms will be in their optimized positions.

It is also useful to consider surface energies in the context of the energy required to cleave the bulk material to form two equivalent surfaces. The cleavage energy, $E_c$ is related to the relaxed surface energy by the equation:

$$E_c = 2\,\gamma_r \tag{5-5}$$

The difference in energies between the relaxed and unrelaxed surface energies represents the extent of relaxation that each surface undergoes. A higher degree of relaxation signifies how much the atomic positions have changed during the relaxation calculations. This can be expressed as a percentage via the equation:

$$\%\,relaxation = \frac{\gamma_u - \gamma_r}{\gamma_u} \times 100 \tag{5-6}$$

We have used these relaxed surface energies to calculate the relaxed equilibrium morphology using Wulff's Theorem (Wulff 1901). This states that the distance the surface and the center of the particle is proportional to the surface energy. For equilibrium morphologies, the Gibbs-Wulff theorem applies. Gibbs determined that crystal particle at thermodynamic equilibrium will form the shape

that minimizes the Gibbs free energy of the surface (Gibbs 1928). This has been successfully been used to predict crystal morphologies for a range of materials including sulfides (Devey et al. 2008) and oxides (Kawabuchi & Magari 1980; Abramowski et al. 1999; Fronzi et al. 2009).

### 5.2.4 Uranium Adatom Surfaces

To calculate the energy of adsorption of a uranium adatom, we placed a single uranium atom above the $ThO_2$ surface slab and performed a geometry optimization calculation. The original unrelaxed positions of U may be seen in Figure 5-8—Figure 5-10. The adsorption energy ($E_{ads}$) for one atom of the U adsorbate can be calculated using the equation:

$$E_{ads} = E_{slab+U} - (E_{slab} + E_U) \quad \textbf{(5-7)}$$

where $E_{slab+U}$ is the energy of the slab with the uranium adatom determined from a single point calculation, $E_{slab}$ is the energy of the surface slab without an adsorbate, and $E_U$ is the energy of a uranium atom in isolation.

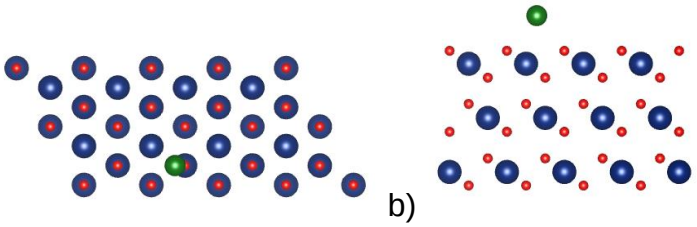

a) b)

**Figure 5-8 Unrelaxed (111) surface with a uranium adatom in green a) top view, b) side view**

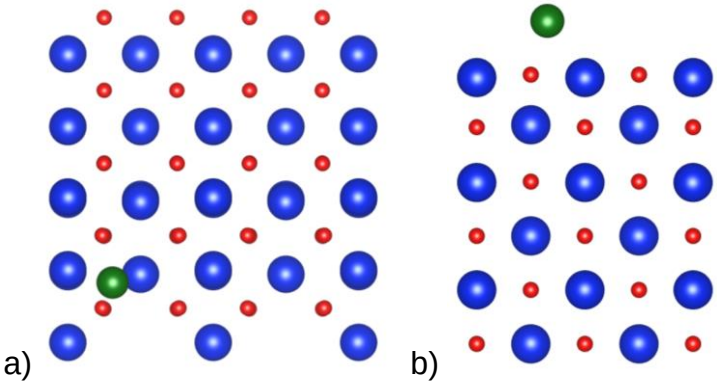


**Figure 5-9 Unrelaxed (110) surface with a uranium adatom in green a) top view, b) side view**

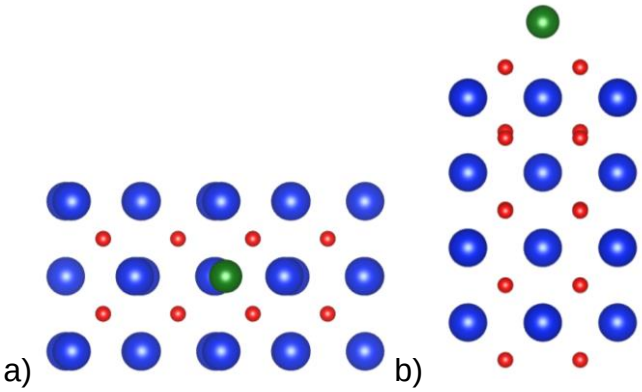


**Figure 5-10 Unrelaxed (100) surface with a uranium adatom in green a) top view, b) side view**

## 5.2.5 Calculation of STM Images

We have calculated the STM images of the three flat surfaces. At the time of writing, we are not aware of the existence of any experimental STM images of the surfaces of thorium dioxide. We therefore propose these images in the

absence of experimental data to use as a comparison with the hope that future experiments on thoria surfaces will find the calculated images useful.

We have used the STM simulation program HIVE to predict STM images from calculations of the partial charge density in VASP (Vanpoucke & Brocks 2008). By applying the Tersoff-Hamann model, which considers the local density of states (LDOS) to be proportional to the tunneling current at a given position of the STM tip (Tersoff & Hamann 1985). HIVE integrates the calculated partial charge density from the Fermi energy to a sample bias (-2.5 eV in the present study). The STM tip is assumed to be an infinitely small point, which varies in height above surface in such a way that the charge density remains constant. A constant charge density represents a constant LDOS, and so follows the Tersoff-Hamann formalism. The HIVE methodology has been successfully implemented previously on the pure atomic surfaces of germanium (Vanpoucke & Brocks 2010) and gold (Irrera et al. 2013), and on iron oxide (Santos-Carballal et al. 2014) surfaces to simulate STM topographies.

## 5.3 Results

### 5.3.1 Structural Effects of U-doping in the $ThO_2$ Bulk

We have plotted the density of states (DOS) for each 2x2x2 supercell system to examine the effects of uranium doping on the electronic structure of thorium dioxide. While small changes to the geometry of the cell are visible in the relaxed structures of the $Th_{(32-x)}U_xO_{64}$ systems under investigation (Figure 5-11),

changes to the electronic structure are clearer when the density of states (DOS) is examined. In Figure 5-11b, it is clear that on the addition of two uranium atoms to the cell, the cation-cation distance is affected and some of the thorium atoms have moved away from the defect region. We have used the SOD code to carry out a more systematic analysis of the inequivalent geometric configurations of uranium substitution in thorium dioxide and their energetics, which have been discussed in Chapter 4.

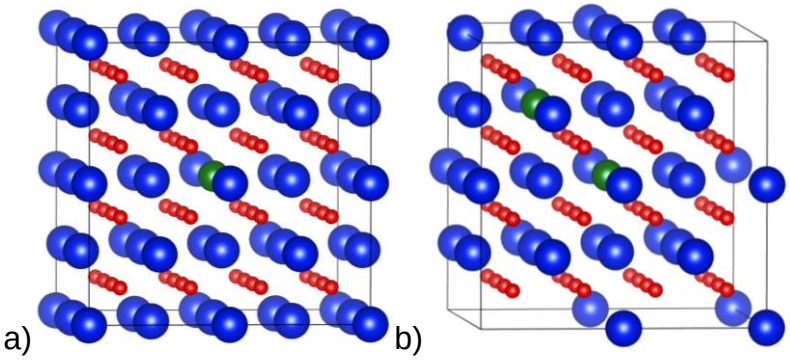


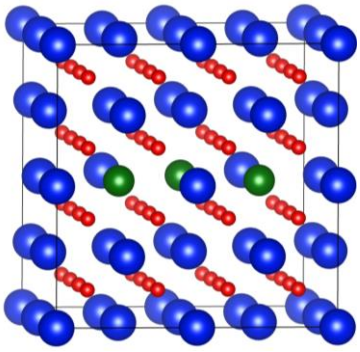


**Figure 5-11 Relaxed $Th_{(32-x)}U_xO_{64}$ supercells with a) one, b) two, and c) three uranium atoms. Thorium, uranium, and oxygen atoms are represented in blue, green, and red, respectively.**

The DOS plot for a 2x2x2 supercell of $ThO_2$, shown in Figure 5-12, was found to

underestimate the experimental band gap of 5.75 eV (Land & Rodine 1971), with a calculated value of 4.12 eV. Our value matches closely with the band gap reported by many other DFT studies of $ThO_2$ in the literature (Shein et al. 2007; Wang, Shi, et al. 2010; Terki et al. 2005). The conduction band is dominated by the Th *5f* electrons while the valence band is predominately comprised of O *2p* states. Uranium substitution affects the total DOS plot as seen in Figure 5-13, Figure 5-14, and Figure 5-15. While the band gap remains the same, there is a shift of the oxygen valence to a lower energy level from the pure $ThO_2$ DOS and a small peak appears at the Fermi level. This shift indicates an increase in the covalent character of the cation-anion interaction compared to the pure compound. This can be further investigated by calculating the charge density distribution for these systems.

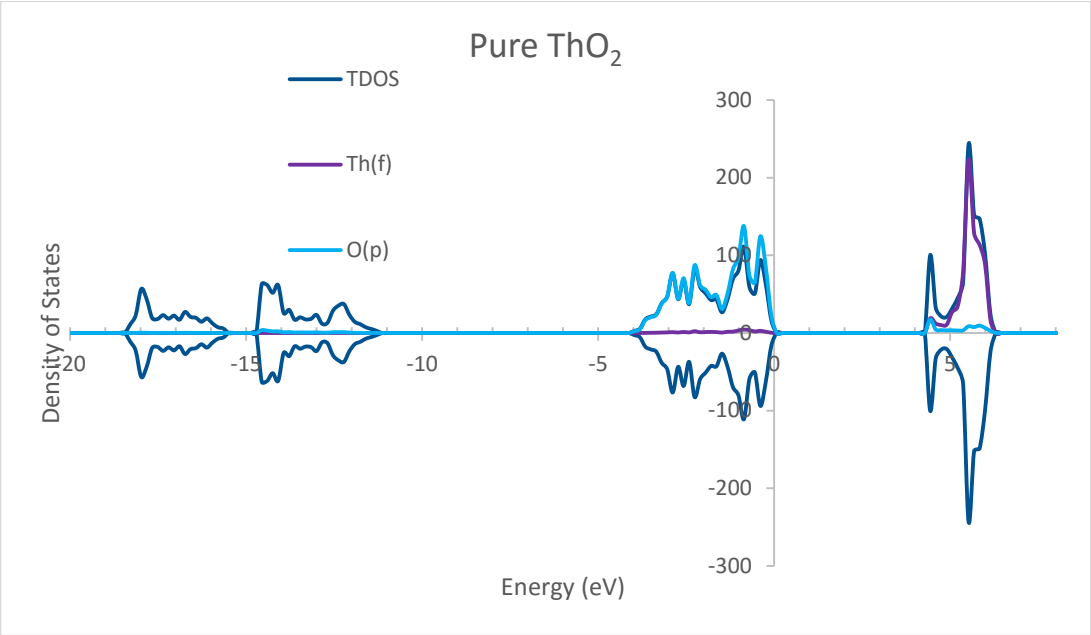


**Figure 5-12 $ThO_2$ DOS including contributions from individual orbitals**

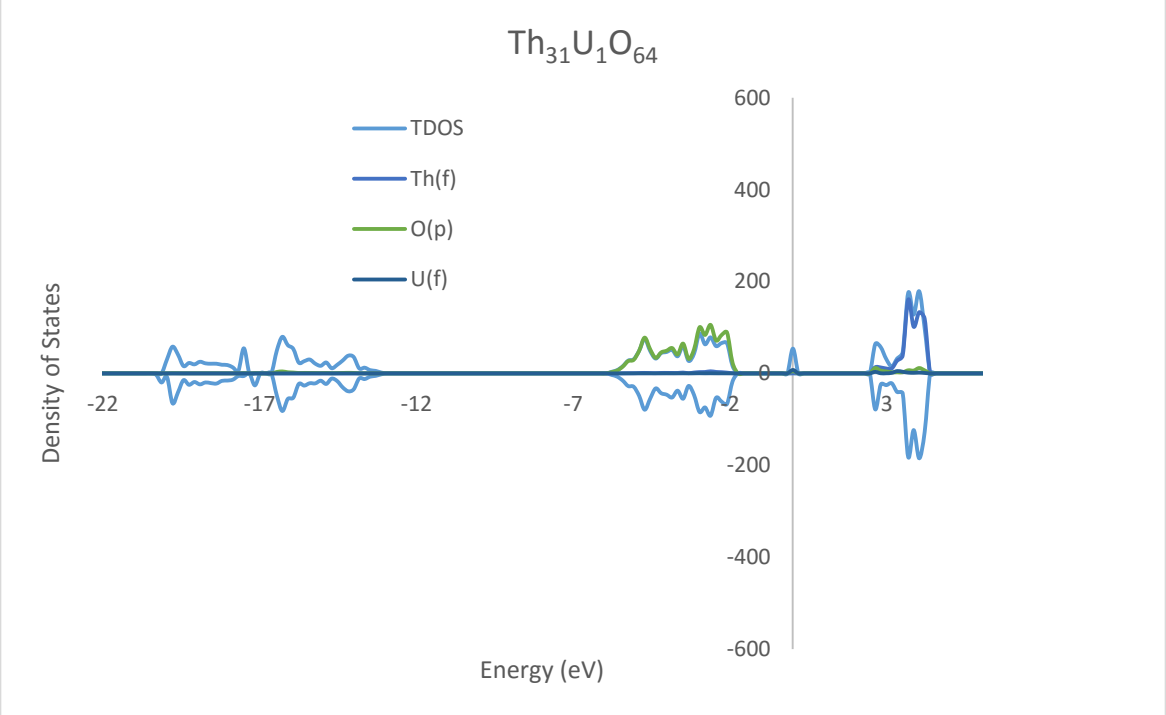


**Figure 5-13 $Th_{31}U_1O_{64}$ total DOS**

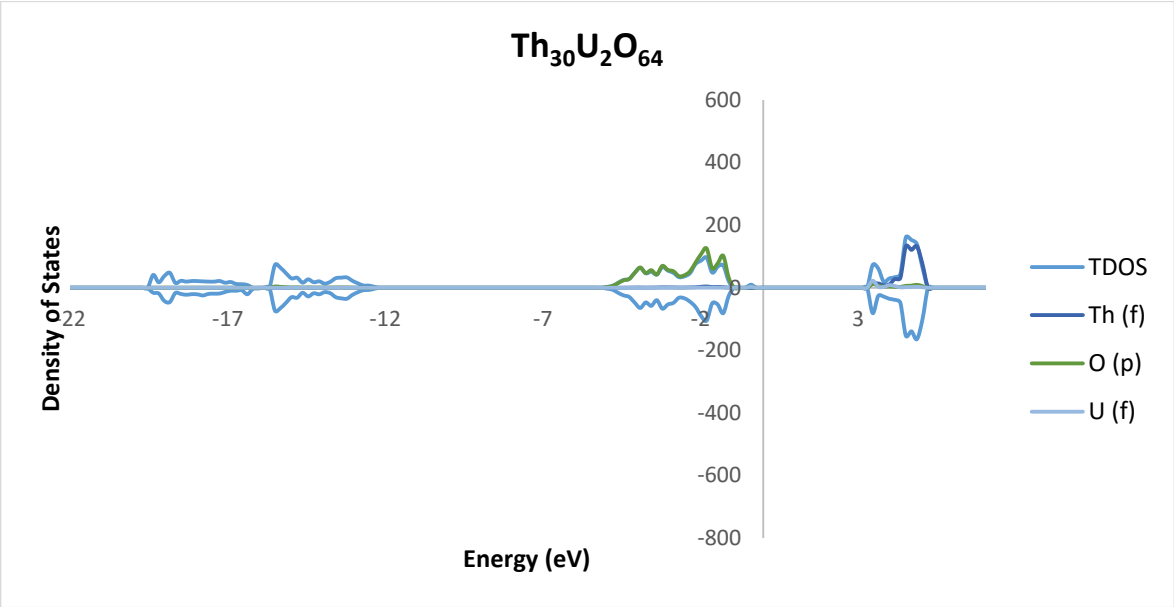


**Figure 5-14 $Th_{30}U_2O_{64}$ total DOS**

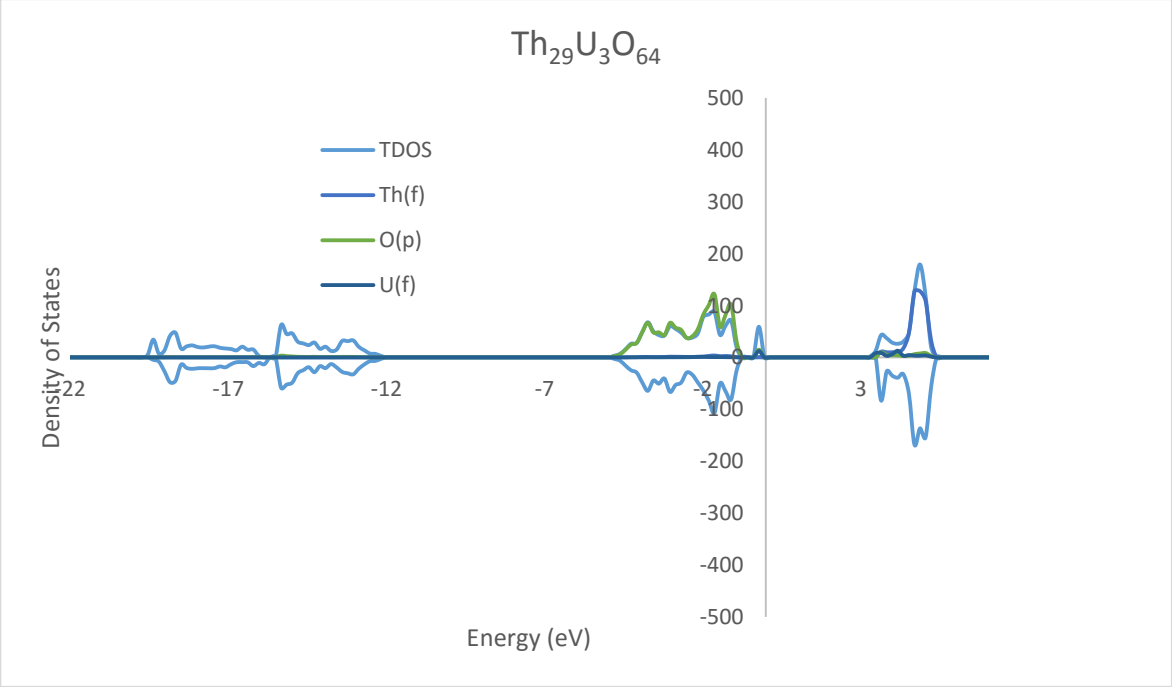


**Figure 5-15 $Th_{29}U_3O_{64}$ total DOS**

### 5.3.2 Charge Density

We have completed a Bader charge analysis of the 1x1x2 supercell for the range of the $ThO_2$-$UO_2$ solid solution. We find the charges for pure $ThO_2$ of Th +2.729 and O -1.365 to be slightly underestimated from the theoretical charges of Th +4 and O -2. This is common with DFT calculations. The valence charge is predominately located on the oxygen atoms in the pure material. This is in agreement with the analysis of $ThO_2$ conducted by other groups, including Wang et al in 2010 (Wang, Shi, et al. 2010). On the addition of uranium to the system, some of the charge density is now distributed to the uranium ions. As the number of U substitutions increases, there is overall a reduction of the positive charge on Th by 0.078 $e^-$ and a reduction of the negative charge on O by 0.074 $e^-$. This change in charge density distribution further supports the increase in covalent character of the Th-O interaction with increasing uranium substitution as more charge is shared, as seen in the DOS

**Table 5-1 The Bader charges on Th, U, and O ions in $Th_{(8-x)}U_xO_{16}$**

| | Bader Charge | | |
|---|---|---|---|
| #U | Th | U | O |
| 0 | 2.729 | -- | -1.365 |
| 1 | 2.654 | 2.541 | -1.320 |
| 2 | 2.659 | 2.569 | -1.318 |
| 3 | 2.665 | 2.562 | -1.313 |
| 4 | 2.660 | 2.571 | -1.308 |
| 5 | 2.651 | 2.567 | -1.299 |
| 6 | 2.652 | 2.575 | -1.297 |
| 7 | 2.657 | 2.571 | -1.291 |

### 5.3.3 Thoria Surface Energies

The three relaxed thorium dioxide surfaces are shown in Figure 5-16 to Figure 5-18. The calculated surface energies before and after relaxation of the (111), (110), and (100) surfaces are presented in Table 5-2. As expected, the oxygen terminated (111) surface orientation is the lowest energy surface. The (100) surface is the least energetically favorable and undergoes the greatest degree of relaxation at 33%. This leads to a distortion of the atomic positions, as seen in Figure 5-18. The Th-O distance between the first layer of O atoms and the

second layer of Th atoms decreases on relaxation by 0.3 Å. The Th-O distance between the second surface layer of Th atoms and the 3$^{rd}$ layer of the surface slab decreases by 0.1 Å. The O atoms also shift out of plane slightly within each relaxed layer. In the unrelaxed surface, the O atoms are in the same plane, with an angle of 180°. After relaxation, the O-O-O angle in the layer is 170°. The (111) surface undergoes the least relaxation, of only 2 %, and is overall the most favorable surface energetically. There are only very small changes in the interatomic distances or atomic positions of the atoms in the (111) surface after relaxation. The Th atoms of the second layer move 0.1 Å closer to the O atoms in the first layer of the slab, and 0.1 farther from the O atoms in the third layer. The (110) surface experiences a greater change in the interatomic distances on relaxation. The first and second layers shift closer together, with a reduction in the Th-Th distance of 0.1 Å. The O atoms shift horizontally in the relaxed layers, with the horizontal O-O distances reduced by 0.35 Å and the O-Th distance by 0.4 Å.

**Table 5-2 Surface Energies of the lowest Miller index surfaces before and after relaxation**

| Surface | Surface Energy (unrelaxed) ($J/m^{-2}$) | Surface Energy (relaxed) ($J/m^{-2}$) | Percent Relaxation |
|---|---|---|---|
| (100) | 1.93 | 1.30 | 32.56 |
| (110) | 0.92 | 0.75 | 18.28 |
| (111) | 0.51 | 0.50 | 2.15 |

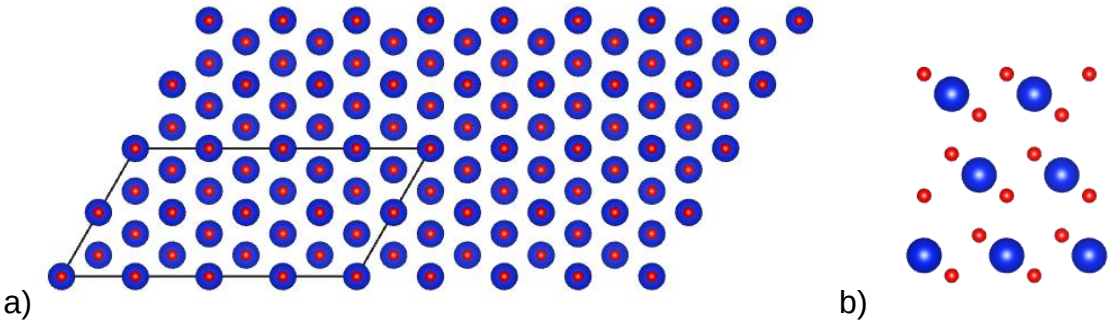


**Figure 5-16 $ThO_2$ (111) a) top and b) side views after relaxation, where Th atoms are represented in blue and O atoms in red**

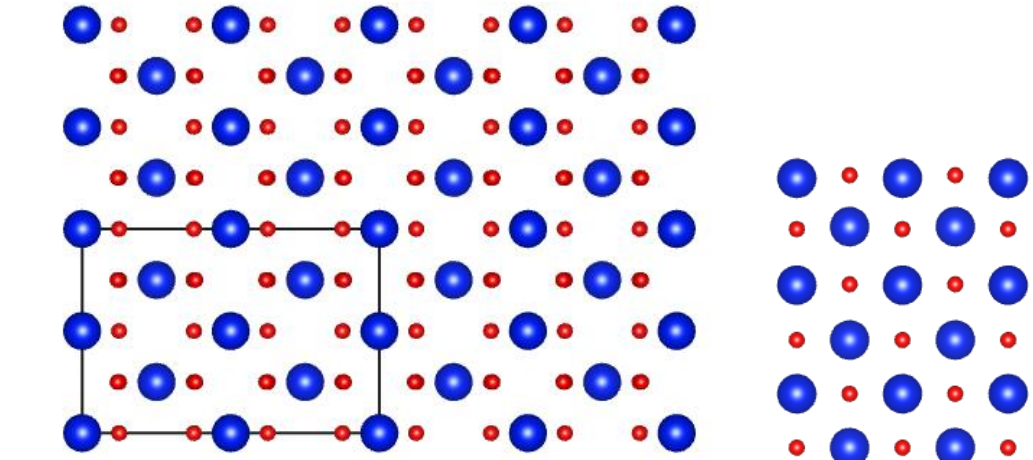


**Figure 5-17 $ThO_2$ (110) a) top and b) side views after relaxation, where Th atoms are represented in blue and O atoms in red**

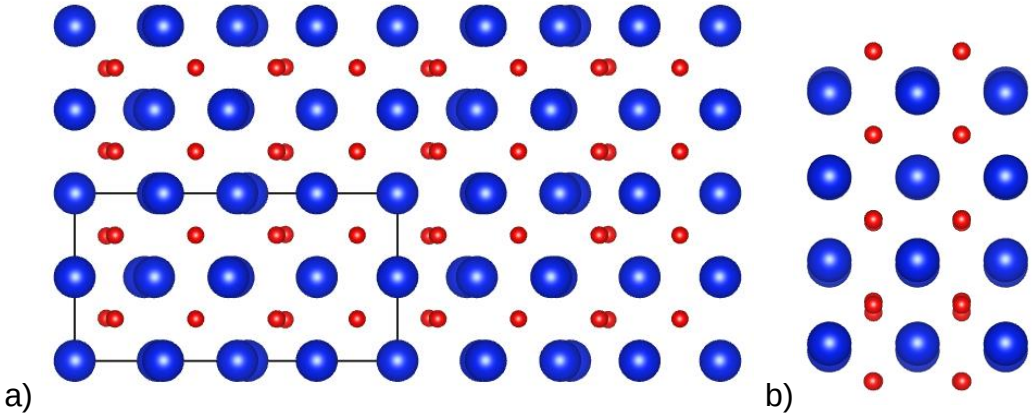


**Figure 5-18 $ThO_2$ (100) a) top and b) side views after relaxation, where Th atoms are represented in blue and O atoms in red**

### 5.3.4 Wulff Morphology

From the relaxed surface energies, we have predicted the Wulff morphology of a thorium dioxide particle at thermodynamic equilibrium. We have used the three low Miller index surfaces studied above at a temperature of 0 K and therefore

the predicted particle is limited to only these three surfaces. However, as the other possible surfaces of $ThO_2$ are expected to be higher in energy than the low Miller plane surfaces in this study, we do not expect them to influence the morphology significantly. We find that the lowest energy (111) surface facets completely dominate the morphology as seen in Figure 5-19. The (110) and (100) surface orientations do not appear in the particle morphology at all. Our predicted morphology is in good agreement with other equilibrium morphology studies of fluorite systems, including $UO_2$ (Abramowski et al. 1999) and $CeO_2$ (Fronzi et al. 2009). The only experimental $ThO_2$ morphology study of which we are aware is the 1980 study by Kawabuchi et al of the influence of plasma currents on the growth morphology of thoria crystals (Kawabuchi & Magari 1980). They found that under the influence of the current, thoria formed rounded crystals and not faceted crystals. However, the experimental stoichiometry of the plasma experiment was $ThO_{1.64}$ and this may have contributed to the final crystal morphology.

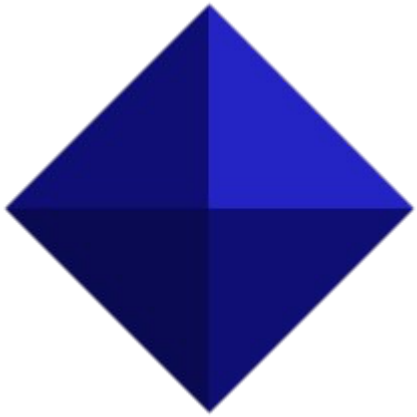

**Figure 5-19 The calculated equilibrium morphology of a thorium dioxide particle. The particle is an octahedron, bounded by facets of the (111) surface**

### 5.3.5 Uranium Adsorption on $ThO_2$ Surfaces

To calculate the adsorption energy ($E_{ads}$) of a uranium atom on the thoria surfaces, we have placed a single atom of uranium on the relaxed surface and allowed it to relax in all directions to find the optimal position. After relaxation, the uranium atom is positioned almost directly over a thorium atom in the surface on the (111) and (100) surfaces, which are both oxygen-terminated. On the (110) surface, which has alternating thorium and oxygen atoms at the surface termination, the uranium has moved to a bridging position and is not located directly over any of the atoms in the top layer of the surface. The energy of adsorption (Figure 5-3) is negative for every surface, meaning that surface the adsorption of a U adatom is favorable compared to the isolated uranium atom. The U adatom binds very strongly to the (100) and (110) surfaces. It is highest for the (111) surface. Even though the (111) surface has the smallest $E_{ads}$ at -

1.89 eV, this value is still highly negative and uranium adsorption on this surface is highly feasible.

**Table 5-3 Adsorption energies of an atom of uranium on the three low Miller index surfaces of $ThO_2$**

| Surface | $E_{ads}$ (eV) |
|---|---|
| (100) | -4.17 |
| (110) | -4.05 |
| (111) | -1.89 |

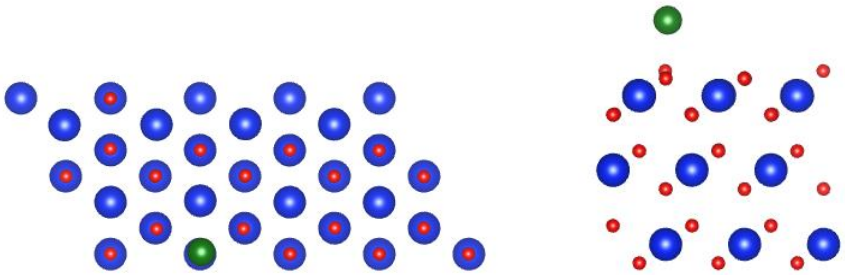

a) b)

**Figure 5-20 Relaxed (111) surface with uranium adatom (green)**

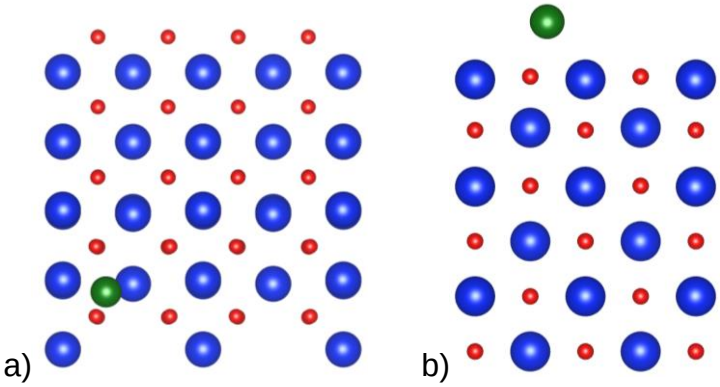


**Figure 5-21 Relaxed (110) surface with uranium adatom (green)**

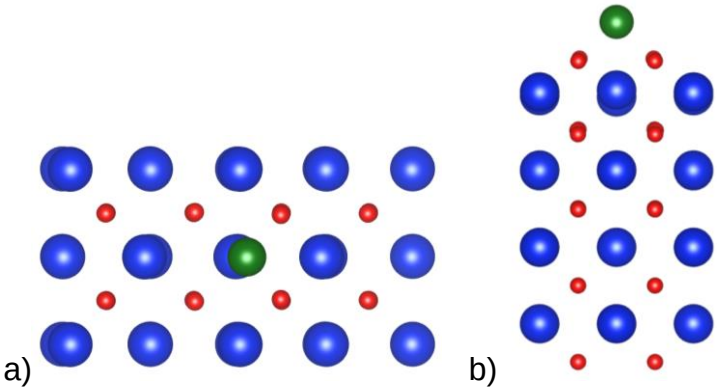


**Figure 5-22 Relaxed (100) surface with uranium adatom (green)**

We have analyzed the effect of the U adatom on the charges of the ions. The results of the Bader charge analysis are presented in Table 5-4. The charge on the uranium ion in general is underestimated and is lowest on the (111) surface, where the U ion is positioned directly over an oxygen ion. For all three surfaces, the addition of the U adatom causes the Th ions on the surface to be reduced by an average of 0.01 $e^-$. The charge on the O ions varies very little on addition of

U to the surface and thus Th is the main donor of charge to the U adatom in the surfaces.

**Table 5-4 Average charges on the Th, U, and O ions for the (100), (110), and (111) pure surfaces and with a U adatom**

| | Charge | | |
|---|---|---|---|
| Surface | Th | U | O |
| 100 | 2.585 | -- | -1.293 |
| 100+U | 2.562 | 0.938 | -1.302 |
| 110 | 2.627 | -- | -1.313 |
| 110+U | 2.615 | 0.580 | -1.320 |
| 111 | 2.665 | -- | -1.333 |
| 111+U | 2.655 | 0.313 | -1.334 |

## 5.3.6 Calculation of STM Images of $ThO_2$ Surfaces

We propose Scanning Tunneling Microscopy images for the (111), (110), and (100) surfaces of thoria. As we are not aware of any STM experiments on $ThO_2$ surfaces, our simulated images may be useful as a predictive guide if such experiments are conducted. During an experimental STM run, the positions of ions on the surface may be affected by perturbations of the electric field due to the STM scanning tip, which are neglected in our simulations. In Figure 5-23, we

observe the (100) surface, with the terminal oxygen ions in white in the image. In the atomic overlay on the simulated images, oxygen is represented by red circles and thorium by blue circles. The Th ions are slightly visible beside and below the oxygen ions. The terminal O ions are also present in the image of the (111) surface and the classic hexagonal structure of (111) surfaces may be seen in Figure 5-24. The alternating Th and O ions are visible on the (110) surface (Figure 5-25).

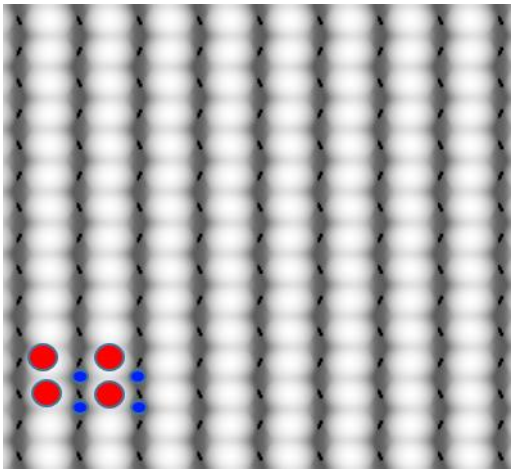

**Figure 5-23 Simulated STM image of the (100) surface of $ThO_2$, where oxygen anions are in represented in red and thorium cations in blue (atomic radii are not to scale).**

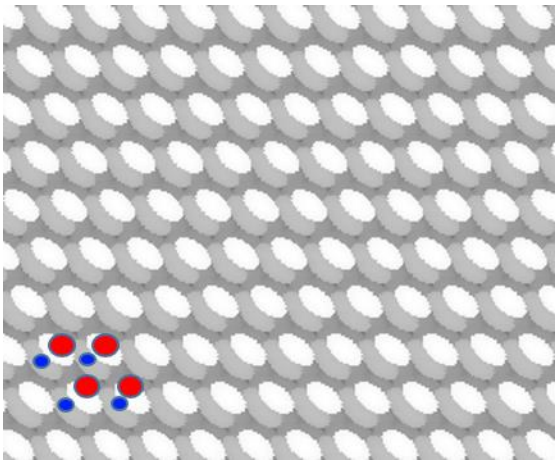

**Figure 5-24 STM Image of the (111) surface of $ThO_2$, where oxygen anions are in represented in red and thorium cations in blue (atomic radii are not to scale).**

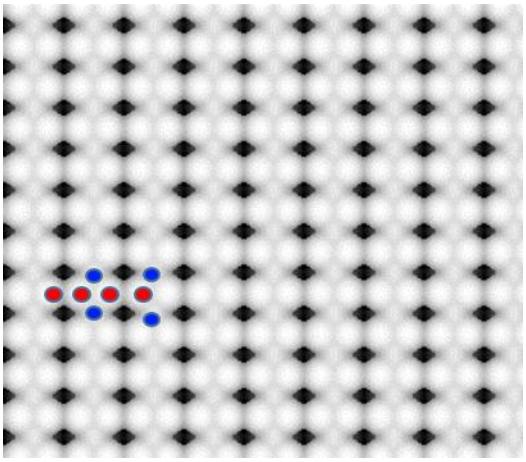

**Figure 5-25 Simulated STM image of the (110) surface of $ThO_2$, where oxygen anions are in represented in red and thorium cations in blue (atomic radii are not to scale).**

## 5.4 Conclusions

We have analyzed available DFT and DFT+U methodologies to determine which best reproduce the electronic structure and physical characters of pure $ThO_2$. We have used GGA with PBE functionals, without the Hubbard U correction, to calculate the density of states and charge density of thoria. On the addition of uranium to the thoria system, the Hubbard U correction to the exchange-correlation must be applied via the GGA+U framework. We have used a $U_{eff}$ of 4eV for uranium, the value common to many other DFT+U studies of uranium. The calculated DOS plots for uranium-substituted thorium dioxide show an increasing covalent character in the system, a finding supported by the calculated charge density plots. Pure $ThO_2$ is mainly ionic, with the electron density localized on the anions. As the uranium content in the system increases, the character of the bonding changes and some of the charge density is shifted on to the uranium cations. In order to look at larger stepped surface systems and grain boundaries, we must shift to force field based methods.

We have modeled three low Miller index surfaces for thorium dioxide, the (100), (110), and (111) flat surfaces and calculated the surface energies of each. The (111) surface is found to be the lowest in energy and is therefore the most stable surface and undergoes the least amount of relaxation from the bulk termination to the unrelaxed surface compared to the other two surfaces studied. We have proposed the Wulff's morphology for a $ThO_2$ particle at equilibrium calculated from the relaxed surface energies and find that the particle is completely

bounded by facets with the (111) surface orientation and takes the shape of an octahedron, in good agreement with the results of similar work on $UO_2$ and $CeO_2$. We have proposed simulated STM images for the three surfaces studied in the absence of other experimental or theoretical work with which to compare the images. After calculating the adsorption energy of a U adatom on the three relaxed surfaces, we expect U to adsorb on to all three surfaces, with particularly strong adsorption on the (110) and (100) surfaces.

# Chapter 6

# $ThO_2$ and $Th_{(1-x)}U_xO_2$ Stepped Surfaces and Grain Boundaries From the (111) Surface

## 6.1 Introduction

Thorium-based MOX fuels may be used in several different Generation IV reactors, such as pebble bed reactors. In pebble bed reactors, the fuel matrix is contained inside a “pebble” of graphite, where each pebble is generally six centimeters in diameter, approximately the size of a tennis ball (Kadak 2005). This type of fuel matrix must of course arise from new fuel processing methodologies and therefore it is important to understand the defect structures of $Th_{(1-x)}U_xO_2$ to improve understanding of new fuel structures. We have explored three surface terminations and uranium adatoms on these surfaces in

Chapter 5 and now wish to investigate other types of surfaces and interfaces. Despite the importance of stepped surfaces and grain boundaries in understanding the practical properties of materials, little work has been done in this field for thorium dioxide. We present six thoria stepped surfaces and six grain boundaries in this chapter, whose structures, relative stabilities, and energies were calculated using the Th-O interatomic potential we developed in Chapter 3. To each of these, we have added uranium in concentrations approximating the low levels of uranium doping required in real-world applications of Th-U MOX fuels.

Furthermore, it is important to understand the behavior of a uranium defect in thorium dioxide surfaces and grain boundaries. In pure $ThO_2$, thorium is transmuted to $^{233}U$ in the presence of a neutron source as discussed in Chapter 1, leading to a uranium defect. By calculating the segregation energy of a uranium impurity as it migrates from the bulk to the top of the surface, the understanding of the movement and distribution of these defects in the material can be better understood. We have also calculated the segregation energy of an oxygen vacancy in pure and uranium-doped $ThO_2$ to elucidate the effects of uranium doping on oxygen migration. Oxygen and uranium defects in the $ThO_2$ bulk material have previously been modeled using molecular dynamics (Cooper et al. 2014; Ma et al. 2015) and DFT simulations (Yun et al. 2009). Aidhy et al have modeled oxygen migration at $CeO_2$/$ThO_2$ bulk interfaces with Ga, La, Nd, and Y dopant ions but have not investigated uranium doping (Aidhy et al. 2014).

However, we are not aware any studies into the effects of uranium doping on oxygen vacancy segregation at stepped surfaces and grain boundary interfaces at this time. Molecular dynamics simulation of defects in $UO_2$ by Govers et al confirmed the influence of grain boundaries on defect migration as compared to the corresponding pure crystal (Govers & Verwerft 2013). The accumulation of defects on or under the surface or interface can greatly impact the physical behavior of a material. It is particularly important to understand this defect accumulation in nuclear fuel materials.

## 6.2 Methodology

### 6.2.1 Modeling Stepped Surfaces and Grain Boundaries

We have used the code METADISE to create planar surfaces, stepped surfaces, and tilt grain boundaries without dipoles from the bulk material (Watson et al. 1996). METADISE has been successfully used to model surfaces and grain boundaries of other oxide systems (Harding et al. 1999; de Leeuw et al. 2000). METADISE uses the two region approach to model interfaces, where region I contains the surface atoms and region II contains atoms that are representative of the bulk. During a geometry optimization, ions in region I are allowed to relax while those in region II are held fixed in their relaxed bulk positions. Region II needs to be included in the calculations to ensure the energy of the ions at the bottom of region I is accurate. For grain boundaries and other interfaces, the simulation contains two blocks, each containing region I and region II type ions (Figure 6-1). The interface occurs at the incidence of two region I surface blocks,

which can be arranged to model different types of interfaces. The total energy of the system is then the sum of the energies of region I and II.

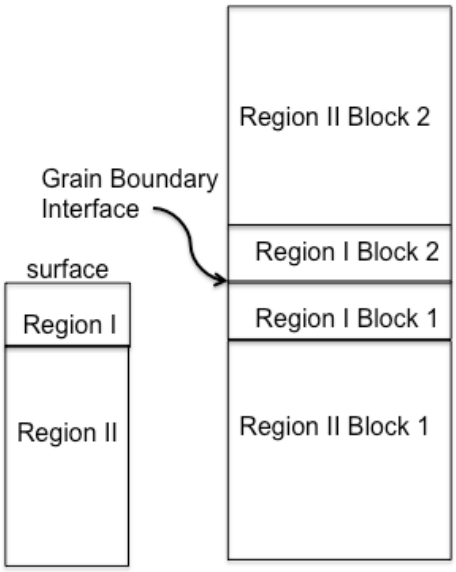


**Figure 6-1 Schematic of the two region approach to modeling surfaces and interfaces**

Based on the work of Tasker on the surfaces of fluorite structures and the results of our Density Functional Theory (DFT) investigations implemented within the Vienna *Ab Initio* Simulation Package (VASP) on three different thoria surfaces in Chapter 5, we have selected the flat (111) surface as our starting point to model stepped surfaces and grain boundaries (Tasker 1979; Tasker 1980; Kresse & Hafner 1993; Kresse & Hafner 1994; Kresse & Furthmüller 1996a; Kresse & Furthmüller 1996b). This is the surface with the lowest surface energy and therefore it is the most stable one. It is also the dominant surface orientation in the relaxed equilibrium morphology. In METADISE, the flat (111)

surface of $ThO_2$ was created from the relaxed bulk structure. This surface was then cut again in METADISE to create a stepped surface.

Next, reflecting this stepped surface across a plane within METADISE and applying a rotation to the reflected block relative to the original stationary block (which is equivalent to the stepped surface) produced grain boundaries with mirror tilt interfaces, where the steps in the surface now create corresponding pores in the grain boundary. In order to model six different grain boundaries, scaling the size of the original (111) flat surface created six different types of stepped surfaces. The depth of the steps was varied to create two different step heights for each of three terrace lengths. These scaled stepped surfaces represent two different pore sizes per terrace size, varying both the length of the terrace and the step height, as seen in Figure 6-2. For clarity, we have assigned the stepped surfaces (S) and grain boundaries (G) names based on the terrace length (T1-T3) and step height (S1 and S2). T1 denotes a terrace length of 22 Å, T2 corresponds to 30 Å, and T3 to a length of 38 Å. The shortest step height is denoted by S1 and the highest by S2.

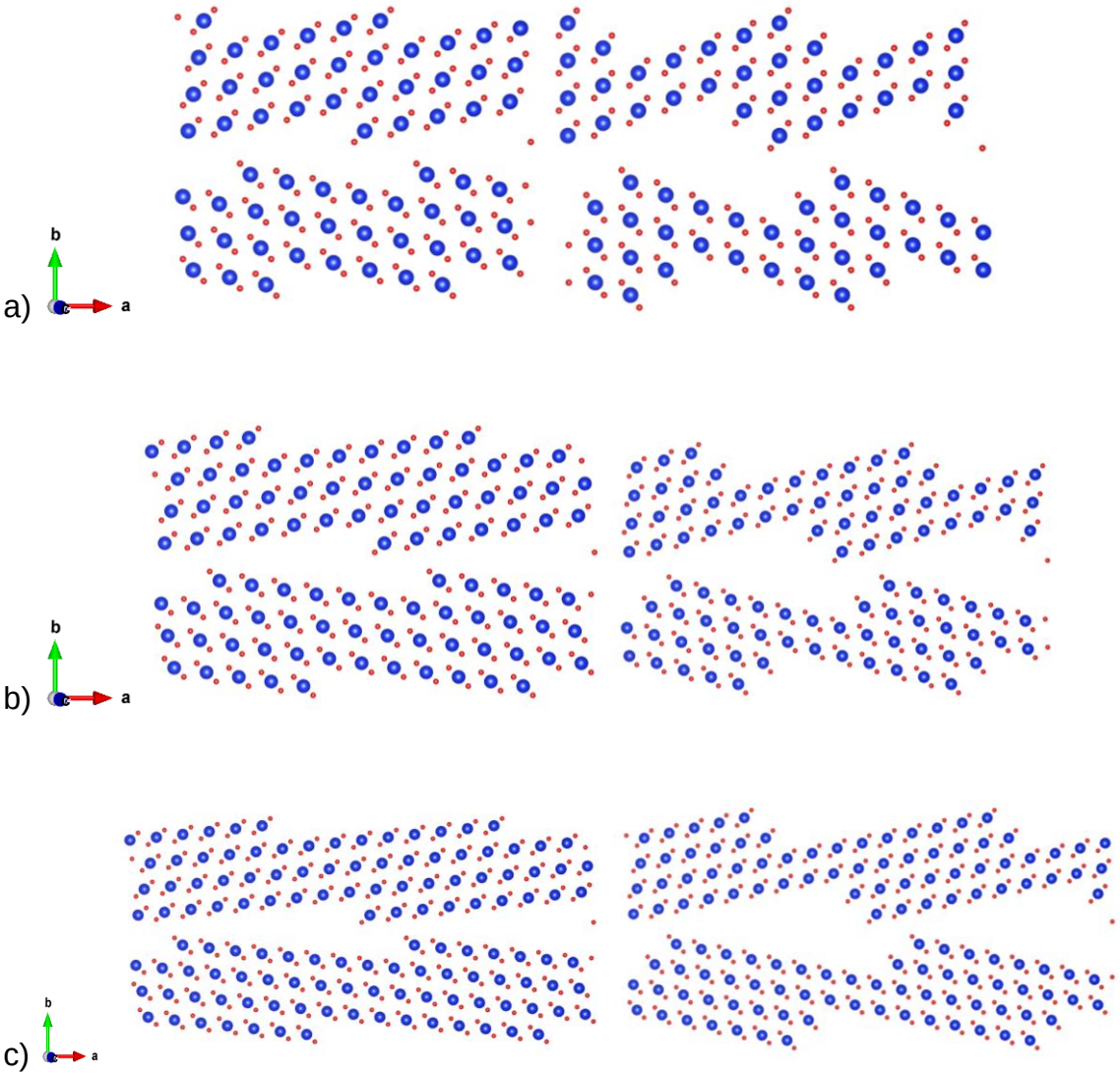


**Figure 6-2** The unrelaxed pure thoria grain boundaries a) GT1S1 (left) and GT1S2 (right), b) GT2S1 (left) and GT2T2 (right), and c) GT3S1 (left) and GT3S2 (right) where Th atoms are represented by blue spheres and O atoms by red.

## 6.2.2 Energies of the Surfaces and Grain Boundaries

We have used energy minimization techniques implemented in METADISE to calculate the surface and boundary energies for the surfaces and grain

boundaries modeled here. Due to the size of the systems being studied, DFT methods cannot be used efficiently at present for the energy calculations. Even for the smallest system in this study, there are 320 atoms in region I block 1 alone, therefore it is most practical to use force field methods to simulate these systems. We have employed the Th-O force field developed in Chapter 3 and the U-O and O-O interactions of Catlow for these calculations as we have elsewhere in this thesis.

The surface energy of the stepped surfaces represents the stability of the surface relative to the corresponding bulk crystal. Accordingly, the surface energy, $\gamma_s$, is calculated from the energy of the surface simulation cell, $E_s$, of surface area A, and the energy of an equivalent number of formula units in the bulk crystal, $E_b$, with the equation:

$$\gamma_s = \frac{E_s - E_b}{A} \qquad \textbf{(6-1)}$$

It is necessary to perform a systematic scan of the potential energy surface of the interface to determine the optimal orientation of block II relative to block I. The atoms in block I are held fixed while those in block II are moved to a new position and then the full system is relaxed. In this way we can determine the structure of the grain boundary that gives the lowest energy. We have scanned the surface in such a manner that sixteen positions of block II were tested and have used the lowest energy structure in further calculations.

To determine the stability of each grain boundary relative to the bulk material, the total energy of the six relaxed grain boundaries was compared to the energy of a corresponding number of atoms of bulk thoria. The boundary energy, $\gamma_g$, is calculated from the total energy, $E_g$, and the energy of an equal amount of the pure relaxed bulk material, $E_b$ using Equation (6-2) where A is the area of the grain boundary. $E_b$ must be doubled to account for the doubling of regions 1 and 2 in METADISE when modeling the grain boundaries; conversely, $E_g$ could be halved for the same result. Another measure of stability is to relate $E_g$ to the surface energy, $E_s$ of the corresponding pure thoria stepped surface to determine the adhesion energy, $\gamma_{ad}$, as in Equation (6-3). This is the energy required to cleave the grain boundary into two equal stepped surfaces. The grain boundary is considered to be stable relative to the bulk crystal where the energy of the grain boundary ($E_g$) is less than twice the energy of the stepped surface system ($E_s$).

$$Boundary\ Energy\ = \frac{\left(2E_b\ -\ E_g\right)}{A} \qquad \textbf{(6-2)}$$

$$Adhesion\ Energy = \frac{\left(2E_s - E_g\right)}{A} \qquad \textbf{(6-3)}$$

### 6.2.3 Calculation of the Segregation Energy of Defects

To calculate the segregation energy of a uranium atom defect in a stepped surface of thorium dioxide, we have first performed a bulk defect calculation using the General Utility Lattice Program (GULP) (Gale 1997; Gale & Rohl 2003). Implementing the CHAOS code (Duffy & Tasker 1983; Duffy & Tasker 1985) within METADISE, we can determine the defect energy of replacing one thorium atom with a uranium impurity at different depths in the surface. This method has been used in many studies of segregation effects in oxide materials (Allen et al. 2009; Aschauer et al. 2006; Balducci et al. 1998). Stanek et al have used a very similar methodology to model cation impurities in $UO_2$ (Stanek et al. 2004). As both GULP and METADISE use Newton-Raphson energy minimization techniques, we can consider the calculated defect energy values to be comparable for our purposes here where we need both the bulk and surface defect energies. The segregation energy, $E_{seg}$, can then be calculated as

$$E_{seg} = E_{sdef} - E_{bdef} \quad \textbf{(6-4)}$$

where $E_{sdef}$ is the defect energy in the surface and $E_{bdef}$ is energy of the same defect in the bulk. We have chosen to investigate the segregation energies of the flat oxygen-terminated (111) surface, as it has the lowest surface energy from our DFT calculations in the previous chapter. We have also used the stepped surface with the shortest terrace length and shortest step, denoted

ST1S1, and its corresponding 13% uranium doped stepped surface to examine the effect of the uranium dopants on an oxygen vacancy.

### 6.2.4 Incorporation of Uranium into the Models

We have modeled eighteen U-doped thoria stepped surfaces and grain boundaries, for a total of thirty-six new systems. These represent a stepped surface and corresponding grain boundary for three mole fractions of uranium (0.06, 0.13, and 0.19) at each terrace size and step depth we previously modeled for pure thoria. Due to the difficulty of ensuring the correct percentage of uranium was in each final structure when starting from a U-doped bulk cell of $ThO_2$, the U atoms were substituted by hand in Materials Studio into the pure thoria stepped surfaces. As we have concluded in Chapter 4, the formation of uranium clusters is not energetically favorable. Therefore in substituting uranium into the stepped surfaces, we have dispersed the uranium atoms through the cell as much as possible. From these surfaces, the corresponding grain boundaries were created in METADISE, using the interatomic potentials we developed and discussed in Chapter 3. The description of the U-O and O-O interactions were again taken from the $UO_2$ potential published by Catlow. Complete details of the potential parameters used are given in Chapter 3.

## 6.3 Results

### 6.3.1 Stabilities of Stepped Surfaces

We have relaxed the structures and calculated the surface energies for each of the six pure $ThO_2$ surfaces (Table 6-1). All of the stepped surfaces are reasonably close in energy, within 0.43 $J/m^2$ of each other. The overall trend is that the lowest energy surfaces for a given step height have the largest surface area and the surface energy increases as the terrace length decreases. The introduction of a step to the surface causes an increase in the surface energy and for those stepped surfaces with a larger terrace area, the relative effect of the step is reduced. A steeper step also introduces a greater energy penalty than the smaller step does in a surface with the same terrace length. This effect has been observed in the faceted surfaces of other oxides, including CaO, MgO and $Mg_2SiO_4$ (de Leeuw et al. 1995; Watson et al. 1996; de Leeuw et al. 2000). The one exception is the surface of area 411 $Å^2$, which has an intermediate terrace length but the highest surface energy of the six pure boundaries. The lowest energy (most stable) surface is the longest terrace length with a short step height. The relaxed structures are presented in Figure 6-3.

**Table 6-1 Surface energies $\gamma_s$ of the pure thoria stepped surfaces**

| Surface | Terrace Length (Å) | Area (Å$^{2)}$ | Step Height (Å) | $\gamma_s$ (J/m$^2$) |
|---|---|---|---|---|
| ST1S1 | 22 | 259 | 4 | 1.49 |
| ST1S2 | | 307 | 9 | 1.70 |
| ST2S1 | 30 | 366 | 4 | 1.42 |
| ST2S2 | | 411 | 9 | 2.12 |
| ST3S1 | 38 | 474 | 4 | 1.39 |
| ST3S2 | | 517 | 9 | 1.53 |

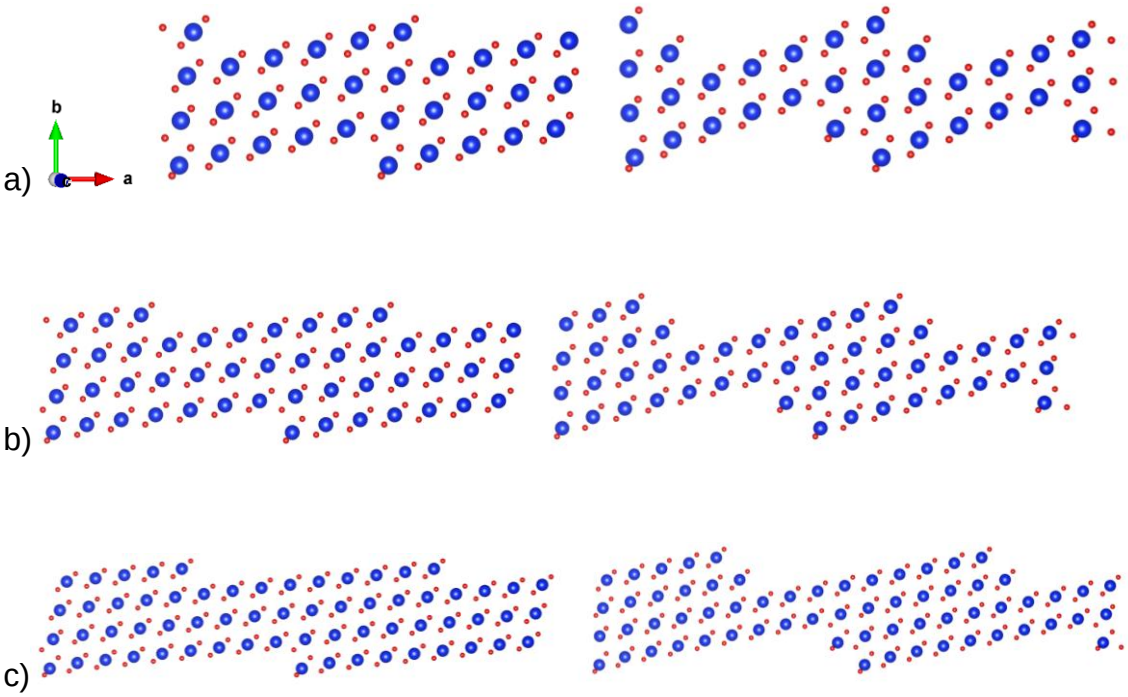


**Figure 6-3 Relaxed stepped surfaces with a) ST1S1 (left) and ST1S2 (right), b) ST2S1 (left) and ST2T2 (right), and c) ST3S1 (left) and ST3S2 (right)**

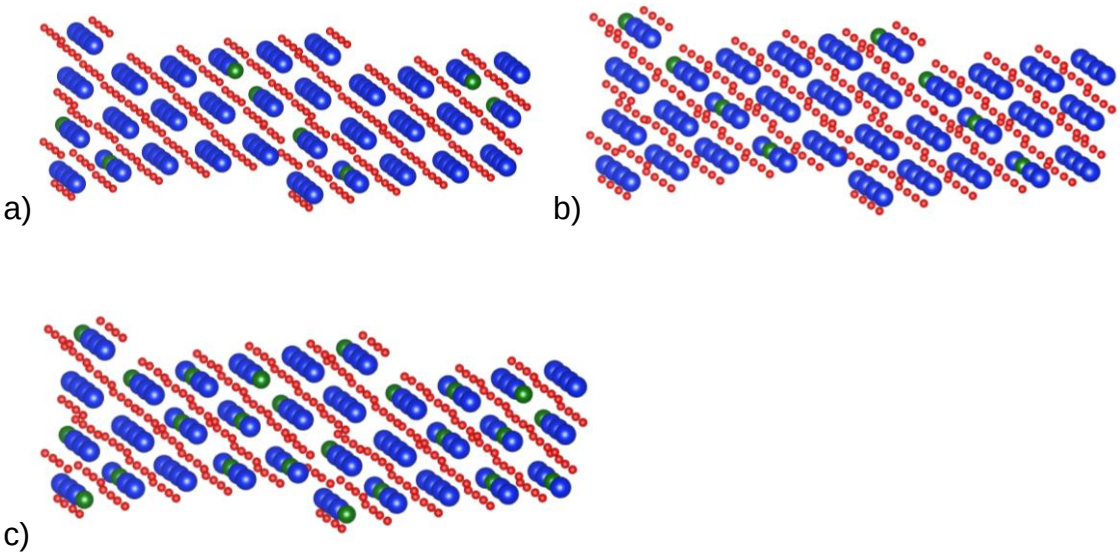


**Figure 6-4 The ST1S1 surface doped with uranium mole fractions of a) 0.06, b) 0.13, and c) 0.19**

We have further added uranium to each of the pure stepped surfaces above in concentrations representing mole fractions of uranium of 0.06, 0.13, and 0.19. Examples of the relaxed uranium-doped stepped surfaces may be seen in Figure 6-4. With uranium substitution, we find that the relative stability of the surfaces decreases as the uranium content of the system increases (Table 6-2). We also find that the surfaces with the longest terrace length (T3-type) have the lowest surface energies for the same level of uranium doping as compared to the surfaces with the shorter terraces. The medium terrace length (T2) surfaces are not included with the rest of the results here, as the amount of dopant by mole fraction of uranium differs from the other two terrace lengths. The T2 surfaces were doped with 0.08, 0.13, and 0.17 uranium by mole fraction and so are only directly comparable to the pure surfaces and where the amount of

dopant coincides with the other doped stepped surfaces at 0.13 U by mole fraction (Table 6-3). When considering all six sizes of the surfaces with 13% uranium, it is clear the T3 terrace is the most stable compared to the other two lengths; in the same way it is the most stable length of the pure surfaces.

**Table 6-2 Surface energies of $Th_{(1-x)}U_xO_2$ stepped surfaces with four different surface areas**

| Surface | Area in Å$^2$ | Angle ° | Mole fraction of Uranium | $\gamma_s$ (J/m$^2$) |
|---|---|---|---|---|
| ST1S1 | 259 | 60 | 0 | 1.490 |
| | | | 0.06 | 1.498 |
| | | | 0.13 | 1.515 |
| | | | 0.19 | 1.525 |
| ST1S2 | 307 | 135 | 0 | 1.697 |
| | | | 0.06 | 1.705 |
| | | | 0.13 | 1.742 |
| | | | 0.19 | 1.749 |
| ST3S1 | 474 | 60 | 0 | 1.386 |
| | | | 0.06 | 1.407 |
| | | | 0.13 | 1.413 |
| | | | 0.19 | 1.420 |
| ST3S2 | 517 | 132 | 0 | 1.525 |
| | | | 0.06 | 1.532 |
| | | | 0.13 | 1.553 |
| | | | 0.19 | 1.558 |

**Table 6-3 Surface energies of stepped surfaces with 13% uranium doping**

| Mole fraction of U | Surface | $\gamma_s$ (J/m$^2$) |
|---|---|---|
| 0.13 | ST1S1 | 1.52 |
| | ST1S2 | 1.74 |
| | ST2S1 | 1.46 |
| | ST2S2 | 1.61 |
| | ST3S1 | 1.41 |
| | ST3S2 | 1.55 |

## 6.3.2 Boundary and Adhesion Energies of Grain Boundaries

We have calculated the boundary and adhesion energies, $\gamma_g$ and $\gamma_{ad}$ respectively, for each of the lowest energy relaxed structures (Figure 6-5) for all six of the pure thoria grain boundaries. The relaxed structures do not all share the same orientation of block 1 relative to block 2, as a scan was performed on the unrelaxed structures in METADISE to determine the optimal orientation, which can differ for each boundary. We expect diffusion of radiation products and other ions to be enhanced for the grain boundaries with the largest terrace size (smallest dihedral boundary angle), e.g. Figure 6-5 (e) and (f), due to the formation of large pores at the boundary interface.

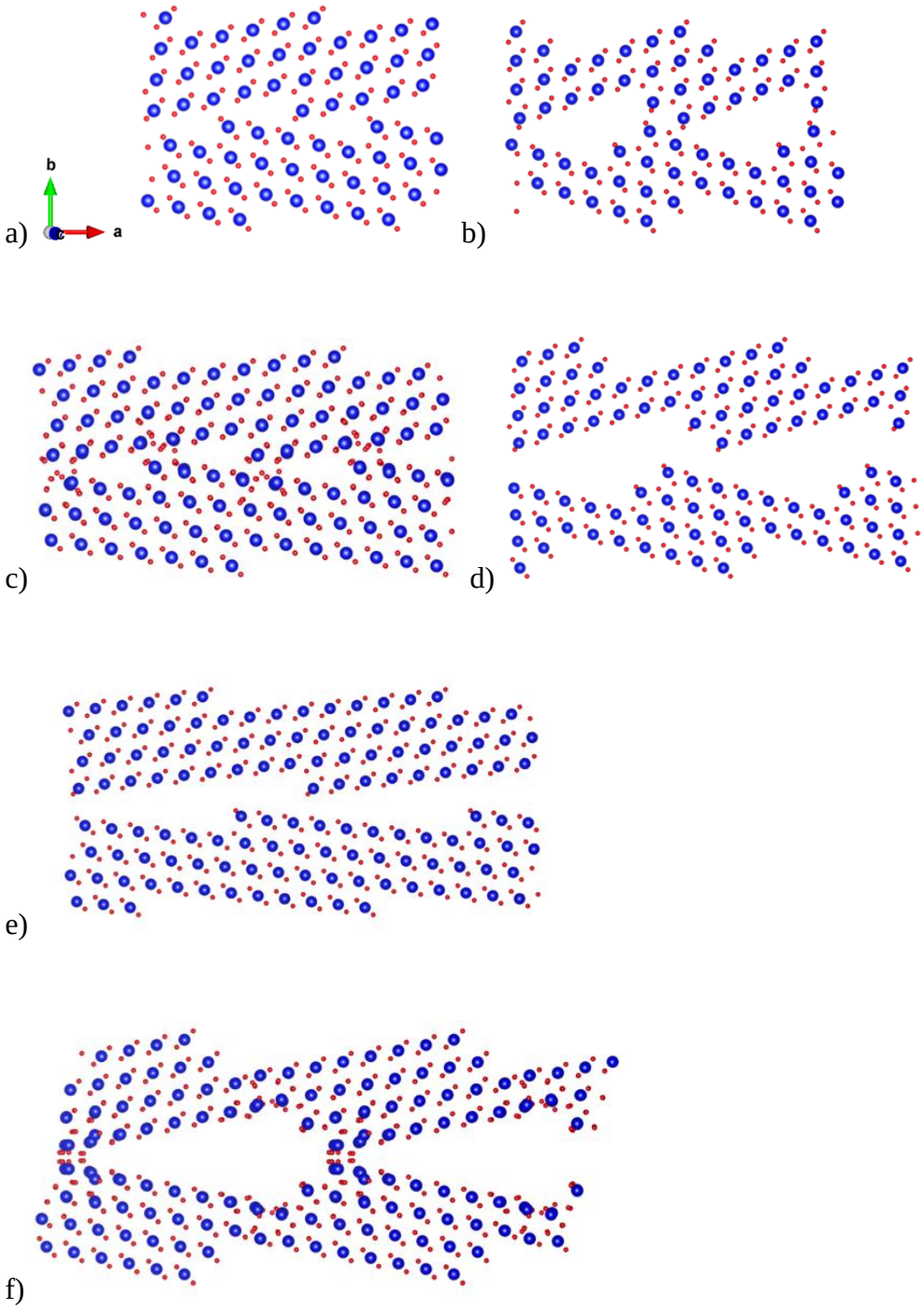


**Figure 6-5 Relaxed grain boundary structures with the lowest energy orientations of block 1 relative to block 2 with dihedral boundary angles of a) 33˚ (GT1S1), b) 42˚ (GT1S2), c) 25˚ (GT2S1), d) 31˚ (GT2S2), e) 14˚ (GT3S1), and f) 19˚ (GT3S2)**

The boundary and adhesion energies for the six types of grain boundaries, with increasing amounts of uranium doping are presented in Table 6-4. The grain boundaries where the dihedral boundary angles are 42˚, 31˚, and 19˚ represent the steepest facet (S2 steps). For all concentrations of uranium, the grain boundaries with the S2 steps have higher boundary energies and are therefore less stable relative to the bulk crystal than those with the shallow step (S1 steps with boundary angles of 33˚, 25˚, and 14˚). On the substitution of uranium into the system (Figure 6-8) $\gamma_g$ increases with increasing concentrations of U for grain boundaries with the smallest areas but $\gamma_g$ decreases for those with the largest areas. This may be because the larger boundaries are better able to stabilize the effects of substituting the $U^{4+}$ cation than the smaller grain boundaries are due to the increased pore size of the large grain boundaries. The adhesion energies (Table 6-4), which measure the stability of the grain boundary with respect to the corresponding faceted surface, are generally small but positive. This indicates that the formation of grain boundaries is unfavorable relative to the stepped surfaces due to the stabilities of the surfaces and the relatively high boundary energies.

**Table 6-4 The boundary and adhesion energies for $ThO_2$ grain boundaries**

| % U | Interface | Angle ° | A in Å$^2$ | $\gamma_g$ J/m$^2$ | $\gamma_{ad}$ J/m$^2$ |
|---|---|---|---|---|---|
| 0 | GT1S1 | 33 | 259 | 2.21 | 0.77 |
| | GT1S2 | 42 | 307 | 2.84 | 0.55 |
| | GT2S1 | 25 | 366 | 2.11 | 0.74 |
| | GT2S2 | 31 | 411 | 3.17 | 0.01 |
| | GT3S1 | 14 | 474 | 2.30 | 0.69 |
| | GT3S2 | 19 | 517 | 3.05 | 0.47 |
| 6 | GT1S1 | 33 | 259 | 2.21 | 0.78 |
| | GT1S2 | 42 | 307 | 2.84 | 0.57 |
| 8 | GT2S1 | 25 | 366 | 2.10 | 0.80 |
| | GT2S2 | 31 | 411 | 2.89 | 0.32 |
| 6 | GT3S1 | 14 | 474 | 1.95 | 1.05 |
| | GT3S2 | 19 | 517 | 2.89 | 0.62 |
| 13 | GT1S1 | 33 | 259 | 2.25 | 0.78 |
| | GT1S2 | 42 | 307 | 2.92 | 0.57 |
| | GT2S1 | 25 | 366 | 2.09 | 0.82 |
| | GT2S2 | 31 | 411 | 2.67 | 0.56 |
| | GT3S1 | 14 | 474 | 1.76 | 1.23 |
| | GT3S2 | 19 | 517 | 2.74 | 0.77 |
| 19 | GT1S1 | 33 | 259 | 2.23 | 0.82 |
| | GT1S2 | 42 | 307 | 2.93 | 0.57 |
| 17 | GT2S1 | 25 | 366 | 2.13 | 0.80 |
| | GT2S2 | 31 | 411 | 2.71 | 0.50 |
| | GT3S1 | 14 | 474 | 1.56 | 1.43 |
| 19 | GT3S2 | 19 | 517 | 2.52 | 1.00 |

For the pure $ThO_2$ grain boundaries, we can consider the ratio of the boundary energy to the surface energy as a function of the boundary angle (Figure 6-6).

While it is experimentally difficult to measure the boundary energy alone, groove experiments on surfaces can calculate the energy based on the dihedral boundary angle and calculate $\gamma_g/\gamma_s$ (Harding et al. 1999). In Figure 6-6, we see that for those boundaries derived from stepped surfaces with the S1 step, which only affects the top surface layer, the ratio $\gamma_g/\gamma_s$ reaches a plateau as the boundary angle increases. However, for those grain boundaries with the S2 step, there is a maximum at a boundary angle of ~30˚. This indicates either a particularly unstable grain boundary or a stable surface. In Figure 6-7, we observe that for the grain boundaries with the S2 step, the adhesion energy reaches a sharp minimum at a dihedral boundary angle of ~30˚ and that those gain boundaries with the S1 step reach a plateau around 15˚. Overall, this indicates that grain boundaries with the S2 (tall) step will be more easily cleaved than those with the S1 (short) step. Unfortunately, we are not aware at this time of any experimental studies of boundary or adhesion energies for $ThO_2$ grain boundaries.

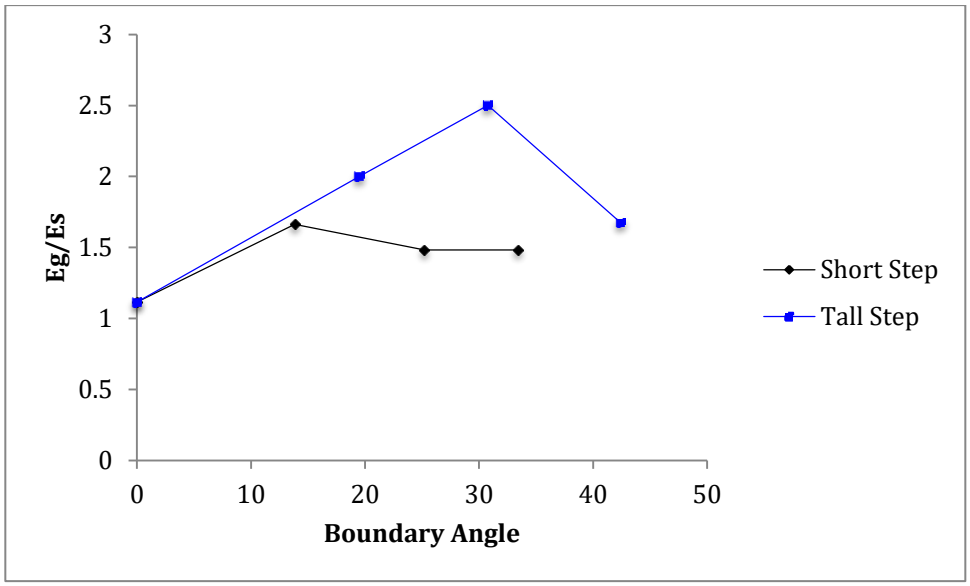


**Figure 6-6 The ratio of the boundary energy to the surface energy ($\gamma_g/\gamma_s$) vs the boundary angle in pure $ThO_2$**

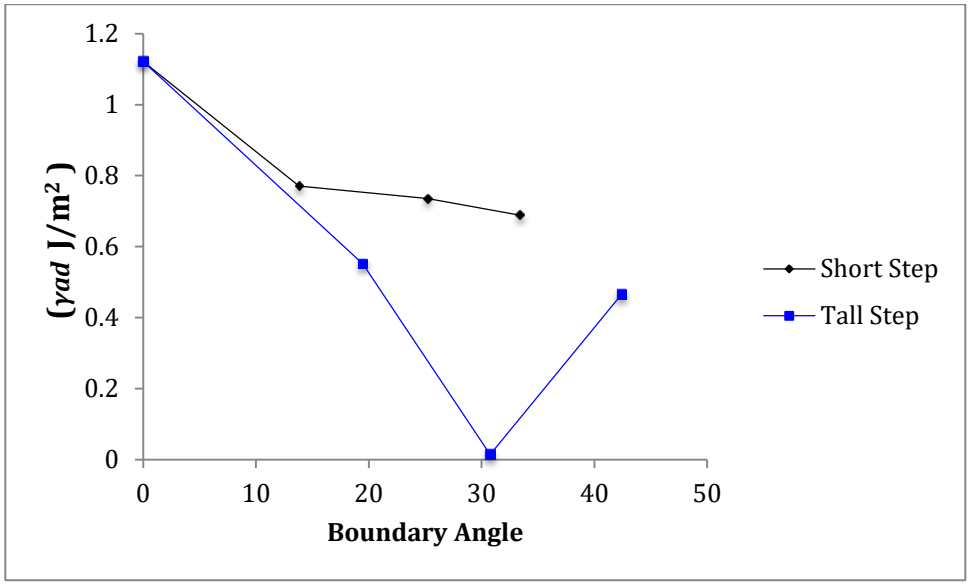


**Figure 6-7 The dependence of the adhesion energy on the boundary angle in pure $ThO_2$**

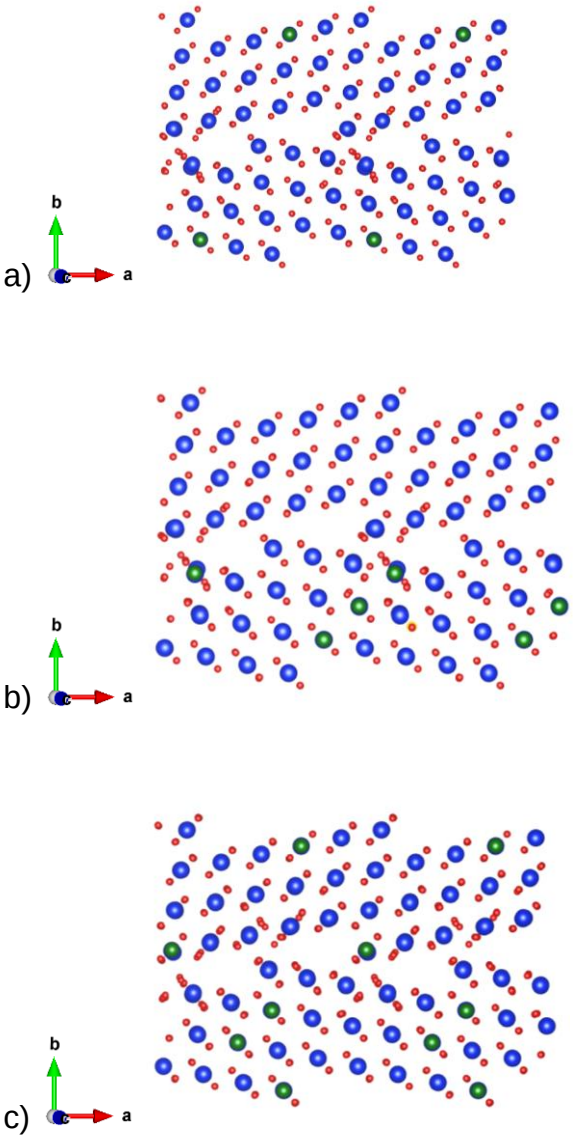


**Figure 6-8 Uranium doped grain boundary of surface area 259 Å$^2$ with mole fractions of uranium of a) 0.06, b) 0.13, c) 0.19**

### 6.3.3 Defect Segregation

We have used GULP to calculate the energy of a uranium impurity in the bulk material and implemented CHAOS within METADISE to calculate the defect energy of a uranium impurity in the flat (111) surface and in the T1S1 stepped

surface (shortest terrace with the smallest step depth) (Figure 6-9). These methods all use the Newton-Raphson energy minimization techniques and so the energy values should be comparable. It was necessary to use larger surface blocks for the defect calculations to ensure convergence of the defect energy and that sufficient surface layers were present to model the variation of the segregation energy with the depth of the defect in the surface. The bulk defect energies calculated are listed in Table 6-5.

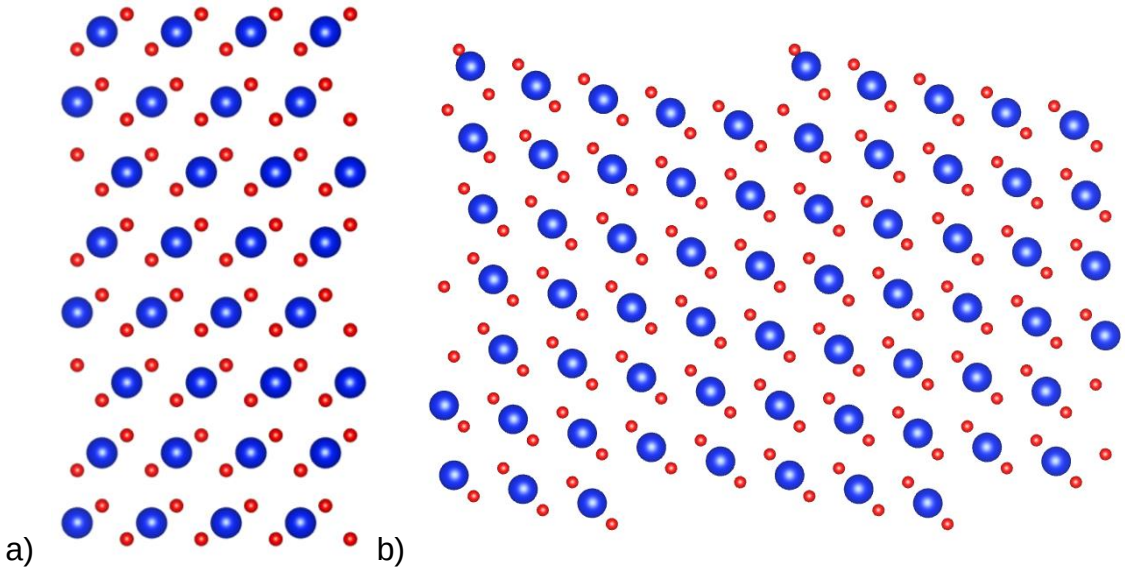


**Figure 6-9 Flat (111) and 22 Å terrace, 60° angle stepped surface for defect calculations**

**Table 6-5 Defect energies in bulk $ThO_2$, in the pure material and in a bulk material doped with 13% uranium**

| Bulk Defects | Uranium Impurity (eV) | Oxygen Vacancy (eV) |
|---|---|---|
| Pure | -2.34 | 16.54 |
| 13% Uranium Doped | -- | 16.50 |

In Table 6-6, we can see that the defect energy of a uranium atom substitution two layers deep in the flat (111) surface has already converged to the bulk defect energy and therefore the segregation energy is zero. The segregation energy converges to the bulk four layers deep in the stepped surface. Furthermore, regarding the stepped surface, the segregation energy is decreased as the U impurity is moved through the surface layers towards the top of the surface. In the topmost layer of the surface, the defect energy becomes a larger positive value. This indicates that a U impurity originating in the bulk may be trapped just below the top surface layer. Previous work by other researchers on Xe and oxygen defect migration and fission gas release in bulk $ThO_2$, including experimental results of Matkze (Matzke 1967) and DFT simulations by Yun et al (Yun et al. 2009) and Xiao et al (Xiao et al. 2011) conclude that fission product ions in thoria are less mobile than defects in $UO_2$ due to higher defect migration energies. Our findings here support the idea that, like the other fission product ions in those studies, the U impurity will remain trapped under the surface of $ThO_2$. It should be noted that the segregation

energies for the uranium defect in thoria are still low in absolute terms, with a maximum value of 0.22 eV in the flat surface and 0.09 eV in the stepped surface. This is most likely due to the fact that $UO_2$ and $ThO_2$ are isostructural and the cations are similar in size. In the grain boundary, moving the uranium impurity to the boundary interface is favorable and we would expect to see the accumulation of uranium impurities at these interfaces.

**Table 6-6 The segregation energy ($E_{seg}$) of a uranium atom in a thorium dioxide flat (111), stepped surface, and grain boundary**

| Surface type | Surface layer | Distance from top of surface plane (Å) | $E_{seg}$ (eV) |
|---|---|---|---|
| Flat (111) | Top layer | 0 | 0.22 |
| | 2nd layer | 3.23 | 0.00 |
| Stepped Surface | Top layer | 0.94 | 0.09 |
| | 2nd layer | 4.29 | -0.03 |
| | 3rd layer | 7.68 | -0.01 |
| | 4th layer | 11.07 | 0.00 |
| Grain Boundary | Interface | 0.87 | -2.25 |
| | 2nd layer | 4.26 | -0.10 |
| | 3rd layer | 7.67 | -0.03 |
| | 4th layer | 11.07 | -0.02 |

We have also considered a single oxygen vacancy moving from the bulk to the surfaces (flat and stepped surfaces). To exclude any energy contribution from an electrostatic field generated by the surface, we have calculated the defect energy of a vacancy very deep in the surface, at a depth in which the defect energy should be equal to the bulk defect energy. By comparing the defect energy of this deep “pseudo-bulk” defect with the defect energy calculated in the true bulk material in GULP, we can adjust the defect energy in METADISE to isolate the energy contributions of the defect. This adjusted surface defect energy is then used in the calculations of the segregation energy. This adjustment was not necessary for the uranium defect, as no difference in energy was found between the “pseudo-bulk” defect and the true bulk defect. When a single oxygen vacancy is introduced into the system, the segregation energy is notably higher in the topmost layer of the surface than in the other surface layers (Figure 6-10 and Figure 6-11). Overall, the segregation energy decreases as the vacancy approaches the bulk.

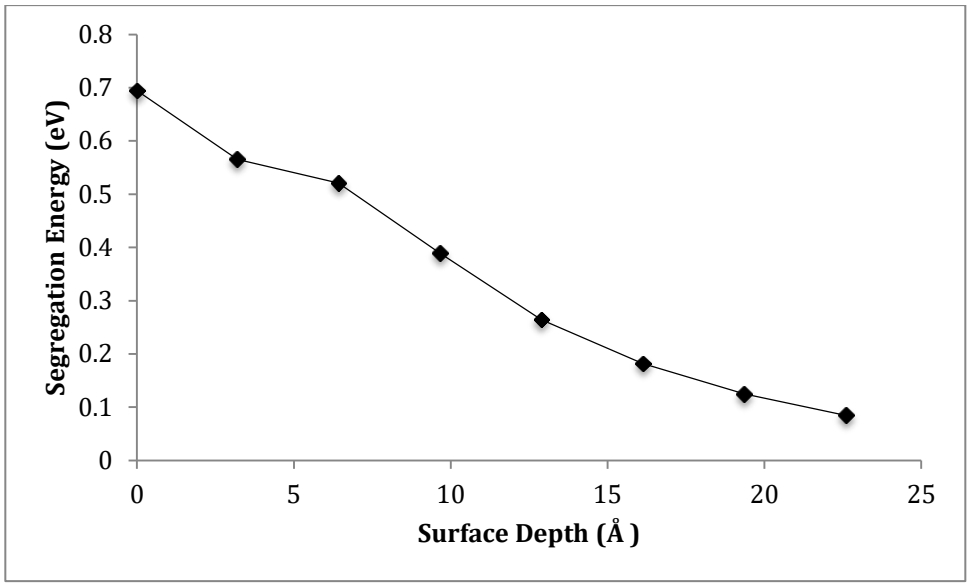


**Figure 6-10 The segregation energy of an oxygen vacancy in the flat (111) surface as a function of increasing distance from the surface**

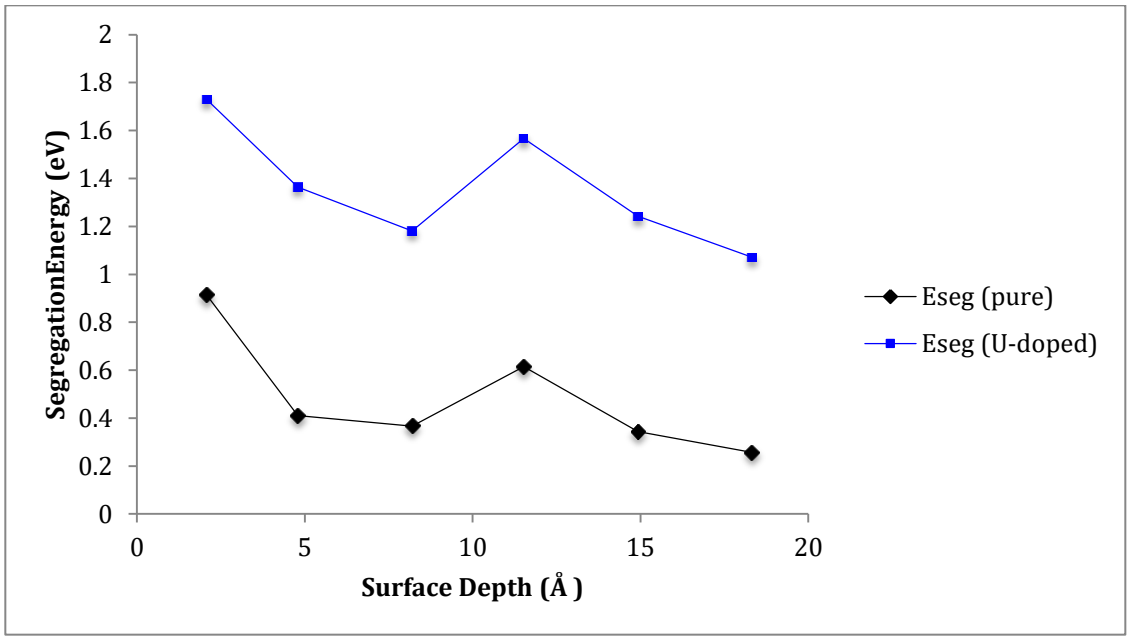


**Figure 6-11 The segregation energy of a single oxygen vacancy in the pure $ThO_2$ stepped surface and in the same stepped surface doped with 13% uranium as a function of the depth of the vacancy in the surface**

We now consider the same oxygen defect in a system doped with 13% uranium, to examine any effects uranium dopants have on the segregation energy of the oxygen vacancy (Figure 6-11). The overall trend is similar to the un-doped system, although the values of the segregation energy are 0.9 eV higher in the doped system than the comparable energy in the pure system. This indicates that the presence of uranium atoms makes it more difficult for the oxygen vacancy to migrate to the surface. However, in the doped surface, the difference in $E_{seg}$ when moving an oxygen atom from the bulk to the topmost layer of the surface vs $E_{seg}$ for the 2$^{nd}$ layer of the surface is much smaller than in the pure surface (though of course, on the whole the $E_{seg}$ values in the doped surface are considerably higher).

In a grain boundary, we observe a similar effect with oxygen vacancies as for uranium impurities (Table 6-7). There is a large negative segregation energy associated with moving the vacancy from the bulk to the boundary interface. However, 7 Å removed from the interface, the segregation energy is positive, indicating that a vacancy migrating from the bulk may become trapped before reaching the interface.

**Table 6-7 Segregation energies of an oxygen vacancy in a pure grain boundary at different depths as measured from the plane of the boundary interface**

| Layer in Grain Boundary | Distance from Interface (Å) | Segregation Energy (eV) |
|---|---|---|
| Top layer | 0.49 | -4.04 |
| 3rd layer | 4.01 | -0.67 |
| 5th layer | 7.26 | 0.37 |
| $7^{th}$ layer | 12.09 | -0.01 |

## 6.4 Conclusions

We have used METADISE and our interatomic potential to model six different stepped surfaces and mirror tilt grain boundaries. From these initial structures we have incorporated uranium into each system to simulate the low concentration uranium doping used in real-world applications of thorium dioxide for a total of 18 $Th_{(1-x)}U_xO_2$ surfaces and another 18 corresponding grain boundaries. We have calculated the surface energies, grain boundary energies, and adhesion energies of these systems. We find that for faceted (stepped) surfaces, a larger step increases the surface energy. For grain boundaries, a larger pore size (resulting from a larger step in the corresponding surface), decreases the stability of the grain boundary. The grain boundaries become relatively more stable as the concentration of uranium increases. We find that

the dihedral boundary angle impacts the ease with which the grain boundary may be cleaved and that grain boundaries resulting from a taller step, which affects several surface layers, will be more easily cleaved than those derived from a small step where only the top layer of the surface is affected.

By using GULP and the CHAOS code within METADISE, we have calculated defect and segregation energies of a uranium impurity in the pure material and an oxygen vacancy in both the pure and uranium-doped surfaces. We conclude that a uranium defect that migrates from the bulk will end up trapped just below the top layer of the surface but that it is favorable to move the U impurity from the bulk to the interface of a grain boundary. The presence of uranium dopants impedes the migration of an oxygen vacancy to the top layer of an interface as compared to migration in the pure crystal.

# Chapter 7

# Conclusions and Future Work

## 7.1 Summary and Conclusions

In this thesis we present the results of a wide-ranging study on the effects of uranium-doping in thorium dioxide. Thoria is an important nuclear fuel material that requires the addition of a neutron source such as uranium before a sustainable fission reaction is achieved. As thorium fuels are considered to be proliferation resistant and as countries around the world search for ways to reduce carbon emissions, as discussed in Chapter 1, academic and political interest in thorium fuels increases every year. As with any nuclear fuel, where safety is of the utmost priority, an understanding of the bulk properties, defect structures, and interfaces is an important fundamental step in predicting the behavior of fuel compound under reactor conditions. Given the expense and health hazards associated with experiments on radioactive substances such as $ThO_2$ and $UO_2$, there is a need for robust computational models of these

systems. In particular, for thoria fuels, the effects of uranium-doping must be understood. In the previous chapters, we have used a variety of computational codes to simulate the $ThO_2$-$UO_2$ system. We have provided a fundamental analysis of the solid solution, a DFT-model of adsorption on the major surfaces of $ThO_2$, a model of faceted surfaces and grain boundary interfaces of pure and U-doped ThO2, and a novel force field describing the Th-O interaction in thorium dioxide which will be of use in further studies of this system. This force field was derived using least squares fitting in GULP to experimental parameters selected after careful evaluation of the available literature data. It is able to successfully reproduce experimental properties of the bulk material, including the lattice parameter, the coefficient of thermal expansion, the bulk modulus, the elastic constants and the Cauchy violation ($C_{12} \neq C_{44}$) of the elastic constants. This interatomic potential has been optimized for use with uranium-doped $ThO_2$, which is a material of particular interest to the nuclear fuel industry. We have gone on to use these force fields extensively in the modeling of uranium substitution in bulk $ThO_2$ and in the modeling of a number of stepped surfaces and grain boundaries.

Our configurational analysis of the $Th_{(1-x)}U_xO_2$ solid solution using the SOD code shows that uranium atoms do not cluster in the bulk thoria crystal. Instead we predict that uranium atoms will be distributed throughout the material. From the configurational analysis of the 1x1x2 and for select concentrations of the 2x2x2 supercells, further studies of these solid solutions or uranium-doped thoria systems can specifically target the most probable configurations, saving computational time and effort. In the solid solution, we calculate that the enthalpy of mixing is endothermic. The Gibbs free energy of mixing has been found to be favorable at temperatures above 600 K. We have considered vibrational effects in further calculations, which show a small miscibility gap in the free energies of mixing, though we do not expect to observe the formation of separate domains at any point in the solid solution.

Using the GGA+U approximation of DFT with PBE functionals, we have completed calculations in VASP to explore the electronic structure of pure $ThO_2$ and the effects low levels of uranium substitution in 2x2x2 $ThO_2$ supercells. We have confirmed that for the widely-used PBE functionals, an effective Hubbard U parameter is unnecessary for thoria calculations. We have presented the density of states plots for the 2x2x2 cells and find our DFT simulations lead to an underestimation of the experimental band gap, which is common in other DFT studies of $ThO_2$. We do still find thoria to be an insulator with a large band gap and correctly reproduce the experimental parameters of the crystal. We

analyzed the Bader charge density of $Th_{(1-x)}U_xO_{16}$ supercells where x = 1-7. We find that the addition of uranium to thoria shifts some of the electronic charge onto the uranium ion, increasing the covalent character of the bonding interactions.

The major surfaces of $ThO_2$ have been studied with DFT. From calculations of the surface energies, we find the (111) surface to be the natural cleavage plane of thoria, as it is the lowest in energy and therefore most stable. This is in agreement with other studies of $ThO_2$ and fluorite structures. The equilibrium particle morphology of $ThO_2$ at thermodynamic equilibrium has been determined to be entirely composed of facets with the (111) surface orientation. STM images for the (111), (110), and (100) surface have been simulated. While, to our knowledge, there are no experimental STM images for these surfaces, we hope these simulated images may prove useful if experimental studies are undertaken. For the three pristine surface modeled in this work, we added a single uranium adatom to the surface and calculated the adsorption energy. We found U adsorbs on all surfaces but binds particularly strongly to the (110) and (100) surfaces. This provides a foundation and methodology for continued DFT studies of adsorbates on $ThO_2$ surfaces.

To further study thoria surfaces and to begin an investigation into interfaces, we used the METADISE code to model six stepped surface orientations based on the (111) flat surface. To these stepped surfaces, we substituted uranium for thorium at three difference concentrations, up to a ~19% uranium dopant. From

the stepped surfaces, we created a corresponding mirror grain boundary. The surface energies, grain boundary energies, and adhesion energies, were calculated for all systems. We found the surface energy is increased by the size of the step wall in the stepped surfaces. For the grain boundaries studied here, a larger pore size increased the boundary energy. The least stable grain boundaries therefore were derived from the models of the least stable stepped surfaces (those with a large step wall). The dihedral boundary angle was found to impact the ease with which the grain boundary may be cleaved. The least stable grain boundaries are predicted to cleave most easily. Based on these simulations, continued studies of faceted (stepped) surfaces and grain boundaries should focus primarily on the most stable of these systems.

We studied the migration of uranium impurities and oxygen vacancies using GULP and the CHAOS code implemented by METADISE. The defect and segregation energies of the uranium impurity were calculated for pure $ThO_2$. We found the uranium atom moving from the bulk crystal to the top layer of the $ThO_2$ surface ended up trapped just below the surface. For the same U impurity in a grain boundary, we found U will move to the top layer of the interface without being trapped. A uranium-doped $ThO_2$ system was included in the calculations that were performed for a single oxygen vacancy. We found that the presence of uranium impeded the segregation of oxygen vacancies to the surface or interface. This is of consequence to the performance and integrity of nuclear fuels and merits future research.

In conclusion, we have used DFT to model small bulk systems (fewer than 100 atoms) and the major surfaces of pure $ThO_2$. We have studied the effect of very low levels of uranium substitution on the $ThO_2$ bulk crystal and the adsorption of single uranium atoms to the pure surfaces. For the investigation of the larger systems, we have developed a new force field describing the Th-O interaction, which is optimized for use with a leading $UO_2$ interatomic potential. These potentials have been employed in a configurational analysis of the $ThO_2$-$UO_2$ solid solution, in calculating useful thermophysical properties of the material, and in the modeling of uranium and oxygen defects at surfaces and grain boundaries. The research presented in this thesis provides a framework for understanding uranium doping in $ThO_2$, particularly at the low dopant concentrations useful in the study of thorium MOX fuels. We hope the interatomic potential model we have developed will be of use in further studies of this material.

## 7.2 Future Work

At the end of this project, we find we still have many questions about the behavior of doped thorium dioxide. Uranium is not the only actinide element useful in thorium-MOX fuels. Plutonium is a commonly used in nuclear reactors and can be combined with thorium dioxide. Work on Pu-doped $ThO_2$ similar to that presented in this thesis would be of considerable interest, as a global reduction in Pu stores is an overall aim of nuclear countries. Future studies on the pure and U- and Pu-doped $ThO_2$ surfaces, particularly in the presence of

water or radiation products would be of great interest to predict the oxidation properties and the effects of adsorbates on the particle morphology of these fuel materials. We present the results of simulations of a single uranium adsorbate on thoria in this thesis and a continuation of that work to investigate other adsorption sites on the surfaces and other levels of adsorbate coverage would be of significant interest in the field. DFT has known issues in modeling large actinide systems with unpaired f electrons but improvements in the simulations may be attained through the implementation of spin-orbit coupling and/or hybrid functionals and this avenue of enquiry should be pursued. While molecular dynamics (MD) simulations have previously been done on bulk thoria, we would be interested to see MD simulations of water on $ThO_2$ grain boundaries and the migration of fission products and other defects, including charged defects and interstitials, across grain boundaries and other interfaces.

# References


Abramowski, M., Grimes, R.W. & Owens, S., 1999. Morphology of $UO_2$. *Journal of Nuclear Materials*, 275(1), pp.12–18.

Adamo, C. & Barone, V., 1999. Toward reliable density functional methods without adjustable parameters: the PBE0 model. *The Journal of Chemical Physics*, 110(13), p.6158.

Aidhy, D.S., Zhang, Y. & Weber, W.J., 2014. Strained ionic interfaces: effect on oxygen diffusivity from atomistic simulations. *The Journal of Physical Chemistry C*, 118(8), pp.4207–4212.

Allen, J.P., Greń, W., Molinari, M., Arrouvel, C., Maglia, F. & Parker, S.C., 2009. Atomistic modelling of adsorption and segregation at inorganic solid interfaces. *Molecular Simulation*, 35(7), pp.584–608.

Anisimov, V.I., Zaanen, J. & Andersen, O.K., 1991. Band theory and Mott insulators: Hubbard U instead of Stoner I. *Physical Review B*, 44(3), pp.943–954.

Anon, 2015. Power Reactor Information System. Available at: http://pris.iaea.org/pris/.

Arima, T., Yamasaki, S., Inagaki, Y. & Idemitsu, K., 2005. Evaluation of thermal properties of $UO_2$ and $PuO_2$ by equilibrium molecular dynamics simulations from 300 to 2000 K. *Journal of Alloys and Compounds*, 400(1-2), pp.43–50.

Arima, T., Yoshida, K., Idemitsu, K., Inagaki, Y. & Sato, I., 2010. Molecular dynamics analysis of diffusion of uranium and oxygen ions in uranium dioxide. *IOP Conference Series: Materials Science and Engineering*, 9(1), p.012003.

Aschauer, U., Bowen, P. & Parker, S.C., 2006. Atomistic modeling study of surface segregation in Nd:YAG. *Journal of the American Ceramic Society*, 89(12), pp.3812–3816.

Bader, R.F.W., 2002. Atoms in Molecules. In *Encyclopedia of Computational Chemistry*.

Balducci, G., Kaspar, J., Fornasiero, P., Graziani, M. & Islam, M.S., 1998. Surface and reduction energetics of the $CeO_2$-$ZrO_2$ catalysts. *Journal of Physical Chemistry B*, 102(3), pp.557–561.

Banerjee, J., Parida, S.C., Kutty, T.R.G., Kumar, A. & Banerjee, S., 2012. Specific heats of thoria–urania solid solutions. *Journal of Nuclear Materials*, 427(1-3), pp.69–78.

Becke, A.D., 1988. Density-functional exchange-energy approximation with correct asymptotic behavior. *Physical Review A*, 38(6), pp.3098–3100.

Becke, A.D., 1993. Density-functional thermochemistry.III. The role of exact exchange. *The Journal of Chemical Physics*, 98(7), p.5648.

Behera, R.K. & Deo, C.S., 2012. Atomistic models to investigate thorium dioxide ($ThO_2$). *Journal of physics. Condensed matter : an Institute of Physics journal*, 24(21), p.215405.

Benny, S., Grau-Crespo, R. & de Leeuw, N.H., 2009. A theoretical investigation of alpha-$Fe_2O_3$-$Cr_2O_3$ solid solutions. *Physical chemistry chemical physics : PCCP*, 11(5), pp.808–15.

Benson, G.C., Freeman, P.J. & E., D., 1963. Calculation of cohesive and surface energies of thorium and uranium dioxides. *Journal of the American Ceramic Society*, 46(1), pp.43–47.

Bertaut, F., 1958. Le terme electrostatique de l'energie de surface. *Comptes Rendus Hebdomadaires Des Seances De L'Academie Des Sciences*, 246, pp.3447–3450.

Birch, F., 1947. Finite elastic strain of cubic crystals. *Physical Review*, 71(11), pp.809–824.

Bloch, F., 1929. Über die Quantenmechanik der Elektronen in Kristallgittern. *Zeitschrift für Physik*, 52(7-8), pp.555–600.

Blöchl, P.E., 1994. Projector augmented-wave method. *Physical Review B*, 50(24), pp.17953–17979.

Born, M. & Huang, K., 1954. *Dynamical theory of crystal lattices*, Oxford: Oxford University Press.

Born, M. & Mayer, J.E., 1932. Zur Gittertheorie der Ionenkristalle. *Zeitschrift für Physik*, 75(1-2), pp.1–18.

Born, M. & Oppenheimer, R., 1927. Zur Quantentheorie der Molekeln. *Annalen der Physik*, 389(20), pp.457–484.

Boys, S.F., 1950. Electronic wave functions. I. A general method of calculation for the stationary states of any molecular system. *Proceedings of the Royal Society A: Mathematical, Physical and Engineering Sciences*, 200(1063), pp.542–554.

Buckingham, R.A., 1938. The classical equation of state of gaseous Helium, Neon and Argon. *Proceedings of the Royal Society A: Mathematical, Physical and Engineering Sciences*, 168(933), pp.264–283.

Catlow, C.R.A., 1977. Point defect and electronic properties of uranium dioxide. *Proceedings of the Royal Society A: Mathematical, Physical and Engineering Sciences*, 353(1675), pp.533–561.

Ceperley, D.M. & Alder, B.J., 1980. Ground state of the electron gas by a stochastic method. *Physical Review Letters*, 45(7), pp.566–569.

Clausen, K., Hayes, W., Macdonald, J.E., Osborn, R., Schnabel, P.G., Hutchings, M.T. & Magerl, A., 1987. Inelastic neutron scattering investigation of the lattice dynamics of $ThO_2$ and $CeO_2$. *Journal of the Chemical Society, Faraday Transactions 2*, 83(7), p.1109.

Colbourn, E.A.A. & Mackrodt, W.C.C., 1983. The calculated defect structure of thoria. *Journal of Nuclear Materials*, 118(1), pp.50–59.

Cooper, M.W.D., Rushton, M.J.D. & Grimes, R.W., 2014. A many-body potential approach to modelling the thermomechanical properties of actinide oxides. *Journal of physics. Condensed matter : an Institute of Physics journal*, 26(10), p.105401.

Crawford, D.C., Porter, D.L. & Hayes, S.L., 2007. Fuels for sodium-cooled fast reactors: US perspective. *Journal of Nuclear Materials*, 371(1-3), pp.202–231.

Dancausse, J.-P., Gering, E., Heathman, S. & Benedict, U., 1990. Pressure-induced phase transition in $ThO_2$ and $PuO_2$. *High Pressure Research*, 2(5-6), pp.381–389.

Dash, S., Parida, S.C., Singh, Z., Sen, B.K. & Venugopal, V., 2009. Thermodynamic investigations of $ThO_2$–$UO_2$ solid solutions. *Journal of Nuclear Materials*, 393(2), pp.267–281.

Dekoussar, V., Dyck, G.R., Galperin, A., Ganguly, C., Todoscow, M. & Yamawaki, M., 2005. *Thorium fuel cycle—Potential benefits and challenges* IAEA, ed.,

Delaye, J.., Louis-Achille, V. & Ghaleb, D., 1997. Modeling oxide glasses with Born–Mayer–Huggins potentials: Effect of composition on structural changes. *Journal of Non-Crystalline Solids*, 210(2-3), pp.232–242.

Devey, A.J., 2011. First principles calculation of the elastic constants and phonon modes of $UO_2$ using GGA+U with orbital occupancy control. *Journal of Nuclear Materials*, 412(3), pp.301–307.

Devey, A.J., Grau-Crespo, R. & de Leeuw, N.H., 2008. Combined Density Functional Theory and interatomic potential study of the bulk and surface structures and properties of the iron sulfide mackinawite (FeS). *Journal of Physical Chemistry C*, 112(29), pp.10960–10967.

Dick, B.G. & Overhauser, A.W., 1958. Theory of the dielectric constants of alkali halide crystals. *Physical Review*, 112(1), pp.90–103.

Dudarev, S.L., Savrasov, S.Y., Humphreys, C.J. & Sutton, A.P., 1998. Electron-energy-loss spectra and the structural stability of nickel oxide: An LSDA+U study. *Physical Review B*, 57(3), pp.1505–1509.

Duffy, D.M. & Tasker, P.W., 1983. *A guide to CHAOS: a program for the calculation of point defect energies near interfaces in ionic crystals*,

Duffy, D.M. & Tasker, P.W., 1985. Computer simulation of grain boundaries in ionic oxides.

Ewald, P.P., 1921. Die Berechnung optischer und elektrostatischer Gitterpotentiale. *Annalen der Physik*, 369(3), pp.253–287.

Fermi, E., 1927. Statistical method to determine some properties of atoms. *Rend. Accad. Naz. Lincei*, 6(December), pp.602–607.

Fronzi, M., Soon, A., Delley, B., Traversa, E. & Stampfl, C., 2009. Stability and morphology of cerium oxide surfaces in an oxidizing environment: A first-principles investigation. *Journal of Chemical Physics*, 131(10).

Gale, J.D., 1997. GULP: A computer program for the symmetry-adapted simulation of solids. *Journal of the Chemical Society, Faraday Transactions*, 93(4), pp.629–637.

Gale, J.D. & Rohl, A.L., 2003. The General Utility Lattice Program ( GULP ). *Molecular Simulation*, 29(5), pp.291–341.

Gibbs, J.W., 1928. *The Collected Works of J. Willard Gibbs* H. A. Bumstead, R. G. van Name, & W. R. Longley, eds., New York: Longmans. Green, & Co.

González-López, J., Ruiz-Hernández, S.E., Fernández-González, Á., Jiménez, A., de Leeuw, N.H. & Grau-Crespo, R., 2014. Cobalt incorporation in calcite: Thermochemistry of (Ca,Co)$CO_3$ solid solutions from density functional theory simulations. *Geochimica et Cosmochimica Acta*, 142, pp.205–216.

Govers, K. & Verwerft, M., 2013. Classical molecular dynamics investigation of microstructure evolution and grain boundary diffusion in nano-polycrystalline $UO_2$. *Journal of Nuclear Materials*, 438(1), pp.134–143.

Grau-Crespo, R., Al-Baitai, A.Y., Saadoune, I. & De Leeuw, N.H., 2010. Vacancy ordering and electronic structure of γ-$Fe_2O_3$ (maghemite): a theoretical investigation. *Journal of physics. Condensed matter : an Institute of Physics journal*, 22(25), p.255401.

Grau-Crespo, R., Hamad, S., Catlow, C.R.A. & Leeuw, N.H. de, 2007. Symmetry-adapted configurational modelling of fractional site occupancy in solids. *Journal of Physics: Condensed Matter*, 19(25), p.256201.

Grau-Crespo, R., de Leeuw, N.H. & Catlow, C.R.A., 2004. Distribution of cations in $FeSbO_4$ : A Computer modeling study. *Chemistry of Materials*, 16(10), pp.1954–1960.

Grau-Crespo, R., Smith, K.C., Fisher, T.S., de Leeuw, N.H. & Waghmare, U. V., 2009. Thermodynamics of hydrogen vacancies in $MgH_2$ from first-principles calculations and grand-canonical statistical mechanics. *Physical Review B*, 80(17), p.174117.

Greaves, E.D., Furukawa, K., Sajo-Bohus, L. & Barros, H., 2012. The case for the thorium molten salt reactor. In *AIP Conference Proceedings*. pp. 453–460.

Haider, S., Grau-Crespo, R., Devey, A.J. & de Leeuw, N.H., 2012. Cation distribution and mixing thermodynamics in Fe/Ni thiospinels. *Geochimica et Cosmochimica Acta*, 88, pp.275–282.

Hamann, D., Schlüter, M. & Chiang, C., 1979. Norm-Conserving Pseudopotentials. *Physical Review Letters*, 43(20), pp.1494–1497.

Harding, J., Harris, D. & Parker, S., 1999. Computer simulation of general grain boundaries in rocksalt oxides. *Physical Review B*, 60(4), pp.2740–2746.

Harding, J.H., Lindan, P.J.D. & Pyper, N.C., 1994. The cohesion of thorium dioxide. *Journal of Physics: Condensed Matter*, 6, pp.6485–6496.

Henkelman, G., Arnaldsson, A. & Jónsson, H., 2006. A fast and robust algorithm for Bader decomposition of charge density. *Computational Materials Science*, 36(3), pp.354–360.

Herring, J.S., MacDonald, P.E., Weaver, K.D. & Kullberg, C., 2001. Low cost, proliferation resistant, uranium–thorium dioxide fuels for light water reactors. *Nuclear Engineering and Design*, 203(1), pp.65–85.

Hill, R., 1952. The elastic behaviour of a crystalline aggregate. *Proceedings of the Physical Society. Section A*, 65(5), pp.349–354.

Hohenberg, P. & Kohn, W., 1964. Inhomogeneous electron gas. *Physical Review*, 136(3B), pp.B864–B871.

Hubbard, J., 1963. Electron correlations in narrow energy bands. *Proceedings of the Royal Society A: Mathematical, Physical and Engineering Sciences*, 276(1365), pp.238–257.

Hubert, S., Purans, J., Heisbourg, G., Moisy, P. & Dacheux, N., 2006. Local structure of actinide dioxide solid solutions $Th_{(1-x)}U_{(x)}O_2$ and $Th_{(1-x)}Pu_{(x)}O_2$. *Inorganic chemistry*, 45(10), pp.3887–94.

Huggins, M.L. & Mayer, J.E., 1933. Interatomic distances in crystals of the alkali halides. *The Journal of Chemical Physics*, 1(9), p.643.

Idiri, M., Le Bihan, T., Heathman, S. & Rebizant, J., 2004. Behavior of actinide dioxides under pressure: $UO_2$ and $ThO_2$. *Physical Review B*, 70(1), pp.1–8.

Ioffe, B.L. & Kochurov, B.P., 2012. Preliminary results of calculations for heavy-water nuclear-power-plant reactors employing $^{235}U$, $^{233}U$, and $^{232}Th$ as a fuel and meeting requirements of a nonproliferation of nuclear weapons. *Physics of Atomic Nuclei*, 75(2), pp.160–162.

Irrera, S., Roldan, A., Portalone, G., Leeuw, N.H. De & De Leeuw, N.H., 2013. The role of hydrogen bonding and proton transfer in the formation of uracil

networks on the gold (100) surface: A Density Functional Theory approach. *The Journal of Physical Chemistry C*, 117(8), pp.3949–3957.

Jankovic, J.T., Underwood, W.S. & Goodwin, G.M., 1999. Exposures from thorium contained in thoriated tungsten welding electrodes. *American Industrial Hygiene Association Journal*, 60(3), pp.384–389.

Jones, J.E., 1924. On the determination of molecular fields. II. From the equation of state of a gas. *Proceedings of the Royal Society A: Mathematical, Physical and Engineering Sciences*, 106(738), pp.463–477.

Kadak, A.C., 2005. A future for nuclear energy: pebble bed reactors. *International Journal of Critical Infrastructures*, 1(4), p.330.

Kanchana, V., Vaitheeswaran, G., Svane, A. & Delin, A., 2006. First-principles study of elastic properties of CeO2 , Th 2 and PoO2. *Journal of Physics: Condensed Matter*, 18(42), pp.9615–9624.

Kandan, R., Babu, R., Manikandan, P., Venkata Krishnan, R. & Nagarajan, K., 2009. Calorimetric measurements on (U,Th)O2 solid solutions. *Journal of Nuclear Materials*, 384(3), pp.231–235.

Kawabuchi, K. & Magari, S., 1980. Growth morphology of $UO_2$, $ZrO_2$, $HfO_2$ and ThO2 crystallites grown from oxide plasmas. *Journal of Crystal Growth*, 49(1), pp.81–84.

Kelly, P.J. & Brooks, M.S.S., 1987. Electronic structure and ground-state properties of the actinide dioxides. *Journal of the Chemical Society, Faraday Transactions 2*, 83(7), p.1189.

Kempter, C.P. & Elliott, R.O., 1959. Thermal Expansion of ⟨UN⟩, ⟨$UO_2$⟩, ⟨$UO_2$-$ThO_2$⟩, and ⟨$ThO_2$⟩. *The Journal of Chemical Physics*, 30(6), p.1524.

Kohn, W. & Sham, L.J., 1965. Self-Consistent equations Including exchange and correlation effects. *Physical Review*, 140(4A), pp.A1133–A1138.

Kresse, G. & Furthmüller, J., 1996a. Efficiency of ab-initio total energy calculations for metals and semiconductors using a plane-wave basis set. *Computational Materials Science*, 6(1), pp.15–50.

Kresse, G. & Furthmüller, J., 1996b. Efficient iterative schemes for ab initio total-energy calculations using a plane-wave basis set. *Physical Review B*, 54(16), pp.11169–11186.

Kresse, G. & Hafner, J., 1993. Ab initio molecular dynamics for liquid metals. *Physical Review B*, 47(1), pp.558–561.

Kresse, G. & Hafner, J., 1994. Ab initio molecular-dynamics simulation of the liquid-metal–amorphous-semiconductor transition in germanium. *Physical Review B*, 49(20), pp.14251–14269.

Kresse, G. & Joubert, D., 1999. From ultrasoft pseudopotentials to the projector augmented-wave method. *Physical Review B*, 59(3), pp.1758–1775.

Land, P.L. & Rodine, E.T., 1971. Electronic defect structure of single-crystal $ThO_2$ by thermoluminescence. *Physical Review B*, 4, pp.2701–2723.

Lee, C., Yang, W. & Parr, R.G., 1988. Development of the Colle-Salvetti correlation-energy formula into a functional of the electron density. *Physical Review B*, 37(2), pp.785–789.

De Leeuw, N.H. & Parker, S.C., 2000. Modeling absorption and segregation of magnesium and cadmium ions to calcite surfaces: Introducing $MgCO_3$ and $CdCO_3$ potential models. *The Journal of Chemical Physics*, 112(9), p.4326.

De Leeuw, N.H., Parker, S.C., Catlow, C.R.A. & Price, G.D., 2000. Proton-containing defects at forsterite {010} tilt grain boundaries and stepped surfaces. *American Minerologist*, 85(9), pp.1143–1154.

De Leeuw, N.H., Watson, G.W. & Parker, S.C., 1995. Atomistic simulation of the effect of dissociative adsorption of water on the surface structure and stability of calcium and magnesium oxide. *The Journal of Physical Chemistry*, 99(47), pp.17219–17225.

Lewis, G. V & Catlow, C.R.A., 1985. Potential models for ionic oxides. *Journal of Physics C: Solid State Physics*, 18(6), pp.1149–1161.

Li, S., Ahuja, R. & Johansson, B., 2002. High pressure theoretical studies of actinide dioxides. *High Pressure Research*, 22(2), pp.471–474.

Liechtenstein, A.I., Anisimov, V.I. & Zaanen, J., 1995. Density-functional theory and strong interactions: Orbital ordering in Mott-Hubbard insulators. *Physical Review B*, 52(8), pp.R5467–R5470.

Lindley, B.A. & Parks, G.T., 2012. Near-complete transuranic waste incineration in a thorium fuelled pressurised water reactor. *Annals of Nuclear Energy*, 40(1), pp.106–115.

Lombardi, C., Luzzi, L., Padovani, E. & Vettraino, F., 2008. Thoria and inert matrix fuels for a sustainable nuclear power. *Progress in Nuclear Energy*, 50(8), pp.944–953.

Lu, Y., Li, D.-F., Wang, B.-T., Li, R.-W. & Zhang, P., 2011. Electronic structures, mechanical and thermodynamic properties of ThN from first-principles calculations. *Journal of Nuclear Materials*, 408(2), pp.136–141.

Lu, Y., Yang, Y. & Zhang, P., 2012. Thermodynamic properties and structural stability of thorium dioxide. *Journal of physics. Condensed matter : an Institute of Physics journal*, 24(22), p.225801.

Ma, J.-J., Du, J.-G., Wan, M.-J. & Jiang, G., 2015. Molecular dynamics study on thermal properties of $ThO_2$ doped with U and Pu in high temperature range. *Journal of Alloys and Compounds*, 627, pp.476–482.

Macedo, P.M., Capps, W. & Wachtman, J.B.O., 1964. Elastic constants of single crystal $ThO_2$ at 25°C. *Journal of the American Ceramic Society*, 47(12), pp.651–651.

Mackrodt, W.C. & Stewart, R.F., 1979. Defect properties of ionic solids. II. Point defect energies based on modified electron-gas potentials. *Journal of Physics C: Solid State Physics*, 12(3), pp.431–449.

Makov, G. & Payne, M., 1995. Periodic boundary conditions in ab initio calculations. *Physical Review B*, 51(7), pp.4014–4022.

Marples, J.A.C., 1976. Plutonium 1975 and other actinides : 5th International Conference on Plutonium and Other Actinides 1975: proceedings. In H. Blank & R. Lindner, eds. *Plutonium 1975 and other actinides : 5th International Conference on Plutonium and Other Actinides 1975: proceedings*. Amsterdam: North Holland Publishing Company.

Martin, P., Cooke, D.J. & Cywinski, R., 2012. A molecular dynamics study of the thermal properties of thorium oxide. *Journal of Applied Physics*, 112(7), p.073507.

Matzke, H., 1967. Xenon migration and trapping in doped $ThO_2$. *Journal of Nuclear Materials*, 21(2), pp.190–198.

Mayer, J.E., 2004. Dispersion and polarizability and the van der Waals potential in the alkali halides. *The Journal of Chemical Physics*, 1(4), pp.270–279.

McLean, D., 1957. *Grain Boundaries in Metals*, Oxford: Clarendon Press.

Monkhorst, H.J. & Pack, J.D., 1976. Special points for Brillouin-zone integrations. *Physical Review B*, 13(12), pp.5188–5192.

Morse, P.M., 1929. Diatomic molecules according to the wave mechanics. II. Vibrational levels. *Physical Review*, 34(1), pp.57–64.

Murnaghan, F.D., 1944. The compressibility of media under extreme pressures. *Proceedings of the National Academy of Sciences*, 30(9), pp.244–247.

Nadeem, M., Akhtar, M.J., Shaheen, R. & Haque, M.N., 2001. Interatomic potentials for some binary oxides. *J. Mater. Sci. Technol.*, 17(6), pp.638–642.

Neugebauer, J. & Scheffler, M., 1992. Adsorbate-substrate and adsorbate-adsorbate interactions of Na and K adlayers on Al(111). *Physical Review A*, 46(24), pp.16067–16080.

Olander, D., 2009. Nuclear fuels – Present and future. *Journal of Nuclear Materials*, 389(1), pp.1–22.

Olander, D.R., 1976. *Fundamental aspects of nuclear reactor fuel elements*, Springfield, VA: Energy Research and Development Administration.

Osaka, M., Adachi, J., Kurosaki, K., Uno, M. & Yamanaka, S., 2007. Molecular dynamics study on defect structure of gadolinia-doped thoria. *Journal of Nuclear Science and Technology*, 44(12), pp.1543–1549.

Perdew, J., Burke, K. & Wang, Y., 1996. Generalized gradient approximation for the exchange-correlation hole of a many-electron system. *Physical Review B*, 54(23), pp.16533–16539.

Perdew, J.P., Burke, K. & Ernzerhof, M., 1996. Generalized Gradient Approximation made simple. *Physical Review Letters*, 77(18), pp.3865–3868.

Perdew, J.P., Chevary, J., Vosko, S., Jackson, K.A., Pederson, M.R., Singh, D.J. & Fiolhais, C., 1992. Atoms, molecules, solids, and surfaces: Applications of the generalized gradient approximation for exchange and correlation. *Physical Review B*, 46(11), pp.6671–6687.

Perdew, J.P. & Wang, Y., 1992. Accurate and simple analytic representation of the electron-gas correlation energy. *Physical Review B*, 45(23), pp.13244–13249.

Reuss, A., 1929. Berechnung der Fließgrenze von Mischkristallen auf Grund der Plastizitätsbedingung für Einkristalle . *ZAMM - Zeitschrift für Angewandte Mathematik und Mechanik*, 9(1), pp.49–58.

Ronchi, C. & Hiernaut, J.P., 1996. Experimental measurement of pre-melting and melting of thorium dioxide. *Journal of Alloys and Compounds*, 240(1-2), pp.179–185.

Ruiz-Hernandez, S.E., Grau-Crespo, R., Ruiz-Salvador, A.R. & De Leeuw, N.H., 2010. Thermochemistry of strontium incorporation in aragonite from atomistic simulations. *Geochimica et Cosmochimica Acta*, 74(4), pp.1320–1328.

Ruiz-Salvador, A.R., Grau-Crespo, R., Gray, A.E. & Lewis, D.W., 2013. Aluminium distribution in ZSM-5 revisited: The role of Al–Al interactions. *Journal of Solid State Chemistry*, 198, pp.330–336.

Sanders, M.J., Leslie, M. & Catlow, C.R.A., 1984. Interatomic potentials for $SiO_2$. *Journal of the Chemical Society, Chemical Communications*, (19), p.1271.

Santos-Carballal, D., Roldan, A., Grau-Crespo, R. & de Leeuw, N.H., 2014. A DFT study of the structures, stabilities and redox behaviour of the major surfaces of magnetite $Fe_3O_4$. *Physical Chemistry Chemical Physics*, 16(39), pp.21082–97.

Sanville, E., Kenny, S.D., Smith, R. & Henkelman, G., 2007. Improved grid-based algorithm for Bader charge allocation. *Journal of Computational Chemistry*, 28(5), pp.899–908.

Savrasov, S.Y., 1996. Linear-response theory and lattice dynamics: A muffin-tin-orbital approach. *Physical Review B*, 54(23), pp.16470–16486.

Schram, R.P.C. & Klaassen, F.C., 2007. Plutonium management with thorium-based fuels and inert matrix fuels in thermal reactor systems. *Progress in Nuclear Energy*, 49(8), pp.617–622.

Schrödinger, E., 1926. An undulatory theory of the mechanics of atoms and molecules. *Physical Review*, 28(6), pp.1049–1070.

Schulz, H., 1999. Short history and present trends of Fischer–Tropsch synthesis. *Applied Catalysis A: General*, 186(1-2), pp.3–12.

Schwarz, K. & Blaha, P., 2003. Solid state calculations using WIEN2k. *Computational Materials Science*, 28(2), pp.259–273.

Seminovski, Y., Palacios, P., Wahnón, P. & Grau-Crespo, R., 2012. Band gap control via tuning of inversion degree in $CdIn_2S_4$ spinel. *Applied Physics Letters*, 100(10), p.102112.

Shanno, D.F., 1970. Conditioning of quasi-Newton methods for function minimization. *Mathematics of Computation*, 24(111), pp.647–647.

Shannon, R.D., 1976. Revised effective ionic radii and systematic studies of interatomic distances in halides and chalcogenides. *Acta Crystallographica Section A*, 32(5), pp.751–767.

Shein, I., Shein, K. & Ivanovskii, A., 2007. Elastic and electronic properties and stability of $SrThO_3$, $SrZrO_3$ and $ThO_2$ from first principles. *Journal of Nuclear Materials*, 361(1), pp.69–77.

Shi, H., Chu, M. & Zhang, P., 2010. Optical properties of $UO_2$ and $PuO_2$. *Journal of Nuclear Materials*, 400(2), pp.151–156.

Shiba, K., Itoh, A. & Akabori, M., 1984. The mechanisms of fission gas release from (Th, U)$O_2$. *Journal of Nuclear Materials*, 126(1), pp.18–24.

Shiba, K., Itoh, A. & Ugajin, M., 1981. Fission xenon release from lightly irradiated (Th, U)$O_2$ powders. *Journal of Nuclear Materials*, 96(3), pp.255–260.

Skomurski, F.N.N., Shuller, L.C.C., Ewing, R.C.C. & Becker, U., 2008. Corrosion of $UO_2$ and $ThO_2$: A quantum-mechanical investigation. *Journal of Nuclear Materials*, 375(3), pp.290–310.

Slater, J.C., 1930. Atomic shielding constants. *Physical Review*, 36(1), pp.57–64.

Smith, K.C., Fisher, T.S., Waghmare, U. V. & Grau-Crespo, R., 2010. Dopant-vacancy binding effects in Li-doped magnesium hydride. *Physical Review B*, 82(13), p.134109.

Sovacool, B.K., 2008. Valuing the greenhouse gas emissions from nuclear power: A critical survey. *Energy Policy*, 36(8), pp.2950–2963.

Stanek, C.R., Bradford, M.R. & Grimes, R.W., 2004. Segregation of $Ba^{2+}$, $Sr^{2+}$, $Ce^{4+}$, and $Zr^{4+}$ to $UO_2$ surfaces. *Journal of Physics: Condensed Matter*, 16(27), pp.S2699–S2714.

Staun Olsen, J., Gerward, L., Kanchana, V. & Vaitheeswaran, G., 2004. The bulk modulus of $ThO_2$—an experimental and theoretical study. *Journal of Alloys and Compounds*, 381(1-2), pp.37–40.

Tang, W., Sanville, E. & Henkelman, G., 2009. A grid-based Bader analysis algorithm without lattice bias. *Journal of physics. Condensed matter : an Institute of Physics journal*, 21(8), p.084204.

Tasker, P.W., 1979. The stability of ionic crystal surfaces. *Journal of Physics C: Solid State Physics*, 12(22), pp.4977–4984.

Tasker, P.W., 1980. The structure and properties of fluorite crystal surfaces. *Le Journal de Physique Colloques*, 41(C6), pp.C6–488–C6–491.

Terki, R., Feraoun, H., Bertrand, G. & Aourag, H., 2005. First principles calculations of structural, elastic and electronic properties of $XO_2$ (X=Zr, Hf and Th) in fluorite phase. *Computational Materials Science*, 33(1-3), pp.44–52.

Tersoff, J. & Hamann, D.R., 1985. Theory of the scanning tunneling microscope. *Physical Review B*, 31(2), pp.805–813.

Thomas, L.H., 1927. The calculation of atomic fields. *Mathematical Proceedings of the Cambridge Philosophical Society*, 23(05), p.542.

Upadhyay, D.G.K., 2008. *Solid State Physics: Lattice Dynamics of Ionic Solids*, New Delhi: Laxmi Publications.

Vanderbilt, D., 1990. Soft self-consistent pseudopotentials in a generalized eigenvalue formalism. *Physical Review B*, 41(11), pp.7892–7895.

Vanpoucke, D. & Brocks, G., 2008. Formation of Pt-induced Ge atomic nanowires on Pt/Ge(001): A density functional theory study. *Physical Review B*, 77(24), p.241308.

Vanpoucke, D.E.P. & Brocks, G., 2010. Density functional theory study of Pt-induced Ge(001) reconstructions. *Physical Review B*, 81(3), p.035333.

Voigt, W., 1928. *Lehrburch der Krystallphysik*, Leipzig: Teubner.

Vosko, S.H., Wilk, L. & Nusair, M., 1980. Accurate spin-dependent electron liquid correlation energies for local spin density calculations: a critical analysis. *Canadian Journal of Physics*, 58(8), pp.1200–1211.

Wang, B.-T., Shi, H., Li, W.-D. & Zhang, P., 2010. First-principles study of ground-state properties and high pressure behavior of $ThO_2$. *Journal of Nuclear Materials*, 399(2-3), pp.181–188.

Wang, B.-T., Zhang, P., Song, H., Shi, H., Li, D. & Li, W.-D., 2010. Structural, mechanical, thermodynamic, and electronic properties of thorium hydrides from first-principles. *Journal of Nuclear Materials*, 401(1-3), pp.124–129.

Wang, J., Yip, S., Phillpot, S. & Wolf, D., 1993. Crystal instabilities at finite strain. *Physical Review Letters*, 71(25), pp.4182–4185.

Wang, Q., Grau-Crespo, R. & de Leeuw, N.H., 2011. Mixing thermodynamics of the calcite-structured $(Mn,Ca)CO_3$ solid solution: A computer simulation study. *Journal of Physical Chemistry B*, 115(47), pp.13854–61.

Watson, G.W., Kelsey, E.T., de Leeuw, N.H., Harris, D.J. & Parker, S.C., 1996. Atomistic simulation of dislocations, surfaces and interfaces in MgO. *Journal of the Chemical Society, Faraday Transactions*, 92(3), p.433.

Wulff, G., 1901. On the question of speed of growth and dissolution of crystal surfaces. *Z. Kristallogr. Mineral.*, 34, pp.449–530.

Xiao, H.Y. & Weber, W.J., 2011. Oxygen vacancy formation and migration in $Ce_{(x)}Th_{(1-x)}O_2$ solid solution. *The journal of physical chemistry. B*, 115(20), pp.6524–33.

Xiao, H.Y., Zhang, Y. & Weber, W.J., 2011. Trapping and diffusion of fission products in $ThO_2$ and $CeO_2$. *Journal of Nuclear Materials*, 414(3), pp.464–470.

Yamashita, T., Nitani, N., Tsuji, T. & Inagaki, H., 1997. Thermal expansions of $NpO_2$ and some other actinide dioxides. *Journal of nuclear materials*, 245, pp.72–78.

Yun, Y., Oppeneer, P.M., Kim, H. & Park, K., 2009. Defect energetics and Xe diffusion in $UO_2$ and $ThO_2$. *Acta Materialia*, 57(5), pp.1655–1659.